Optimization of a Multi-Element Airfoil for a Rigid Airborne Wind Energy Kite

Master Thesis

Agustí Porta Ko

Delft University of Technology

TU Delft

KITEMILL

Optimization of a Multi-Element Airfoil for a Rigid Airborne Wind Energy Kite

by

Agustí Porta Ko

to obtain the degree of Master of Science
at the Delft University of Technology.

Supervisors:	Dr.-Ing. Roland Schmehl	
	Tekn.Lic., M.Sc., Sture Smidt	
Thesis committee	Dr.-Ing. Roland Schmehl	TU Delft, chair
	Dr.ir. Delphine De Tavernier	TU Delft
	Dr.ir. Alexander van Ziujlen	TU Delft
	Tekn.Lic., M.Sc., Sture Smidt	Kitemill AS

Cover Image: Kitemill AS' kite during take-off at the test site in Lista, Norway, taken on August 17^{th}, 2021.

TU Delft

Preface

I first stumbled upon the airborne wind energy field around two years ago, through one of the master degree courses. Such research domain immediately appealed to me since it utterly aligned with my interests and allowed me to use my skills to contribute to the development of a sustainable source of energy. Hence, I decided to steer my early career in that direction; I was able to acquire an internship in Kitemill AS, one of the leading companies in the sector. After an extremely valuable experience as an intern, the company and I formulated a research topic for the present master thesis, as part of their product development.

I would like to express my gratitude to Kitemill for giving me the opportunity to actively contribute to the development of such groundbreaking and challenging technology. Thanks to S. Smidt for the trust in me and helping me become a better engineer through the tips and supervision. I would also like to thank R. Schmehl, the insights and valuable feedback were always most welcome, they certainly guided my work into a better version.

I would furthermore like to thank M. Mandru, for mentoring me all along this journey by sharing with me his experience and advice. All my colleagues in Kitemill for being so welcome and friendly since the very first day, I could not have imagined a more valuable and rewarding experience for my internship and thesis. J. Poland for being an ideal colleague, housemate and friend, our trips enhanced the experience in Norway. G. Cremades for remaining my closest friend despite being far away. Lastly, my family for their unconditional support and guidance in every step I take.

Agustí Porta Ko
Lista, Norway, November 2022

Summary

In the present thesis a two-element airfoil has been designed through optimization for a rigid Airborne Wind Energy kite (AWE). AWE is an emerging technology that aims to harvest high-altitude wind energy through the use of a kite tethered to a ground station. Since the kite operates in a pumping cycle or ground-gen, it has two main operational phases: reel-out or production phase and reel-in or return phase. Each phase has radically different requirements, thus making the airfoil design somewhat complex. To deal with such distinct requirements, the airfoil has been first optimized for production phase, and the result has been adapted to perform efficiently for return phase as well, through a movable flap. Hence, two configurations have been developed for the multi-element airfoil.

The optimization strategy is based on a multi-objective genetic algorithm, coupled with MSES, a 2D aerodynamic solver employed for design and analysis of multi-element airfoils with low computational cost. The choice of a genetic algorithm is justified by its robustness in finding the global optima in a highly non-linear design space and its flexibility when dealing with a multi-objective problem. The downside of such algorithm, is its high computational cost, resulting from its population based methodology, however, such drawback has been mitigated by employing a low computational cost solver: MSES. In addition, MSES has been proved to be a suitable solver for the optimization algorithm due its capability of being executed from the terminal, and thus from a Matlab script, and its automatically generated high quality mesh. A significant drawback from MSES when coupling it to the algorithm is that it does not converge for particular geometries or flow conditions. Such phenomena has been mitigated by combining the algorithm with the human-in-the-loop technique, i.e. the designer has monitored and manually analysed several required cases so that the algorithm can carry on.

The airfoil parametrization scheme has been developed such that the number of design variables is relatively low while providing enough flexibility and shape control in the regions of interest. To that end, a parametrization method based on the NACA 4-digits nomenclature combined with a modification on the TE of the main element to enhance flap integration has been employed. The objective functions that have driven the optimization for production phase have been selected with the goal of maximizing the power output. To that end, the operational C_L and the power coefficient C_L^3/C_D^2 along the whole operational range have been maximized, leading to a multi-objective optimization, which has been dealt through the pareto front.

The airfoil resulting from the optimization procedure has then been evaluated for return phase, where the aim is to minimize the aerodynamic loads such that the overall power cycle is most efficient. In order to reduce the loads, the flap is rotated upwards, however, it has been observed that flow separation takes place on the main element at low AoA's such that low enough C_L's are not attainable. To resolve that, the flap rotational pivot point has been modified such that the flap location in flap-up configuration helps mitigating flow separation by accelerating the boundary layer on the main element.

Lastly, the aerodynamic performance of the designed multi-element airfoil has been verified through CFD RANS simulations, using the open source software OpenFOAM. The CFD setup has been first validated with the experimental data of a single-element airfoil showing fairly good agreement. The turbulence model $k-\omega$ SST has been selected due to its superior performance both for external flows as for the boundary layer flow. The employed mesh has a hybrid topology, structured close to the airfoil and wake and unstructured in the far field, which has been constructed with the software Cadence. Said software allows scripting, hence simplifying vastly the process of analyzing different airfoil geometries. The MSES verification has shown good agreement in terms of lift coefficient but a considerable overprediction of drag has been observed. The flow separation phenomena observed with MSES for the return phase configuration has been analysed with CFD through the flow visualization, showing good agreement between the two tools.

Contents

Nomenclature

Abbreviations

Abbreviation	Definition
AoA	Angle of Attack
AWE	Airborne Wind Energy
BL	Boundary Layer
CF	Capacity Factor
CFD	Computational Fluid Dynamics
CMA - ES	Covariance Matrix Adaptation Evolution Strategy
et al.	and others
etc.	et cetera—and similar things
EA	Evolutionary Algorithm
GA	Genetic Algorithm
HAWT	Horizontal Axis Wind Turbine
i.e.	id est—that is to say
IGP	Improved Geometrical Parametrization
LCOE	Levelized Cost Of Energy
LE	Leading Edge
MAC	Mean Aerodynamic Chord
max	maximum
min	minimum
MIT	Massachussets Institute of Technology
MOGA	Multi Objective Genetic Algorithm
NSGA II	Non-dominated Sorting Genetic Algorithm II
PP	Pivot Point
RMS	Root Mean Square
SST	Shear Stress Transport
TU Delft	Delft University of Technology
TE	Trailing Edge
wrt	with respect to

Symbols

Symbol	Definition	Unit
C	Aerodynamic coefficient	
c	Chord	m
CH_4	Methane	
CO_2	Carbon dioxide	
e	Mass-specific energy	J/kg
F	Force	N
f	Function	
k	Turbulence kinetic energy	
l	Length	m
m	Camber	
Ma	Mach number	
n	Number, amount	
n	Normal vector of a surface	
N_2O	Nitrous oxide	
P	Power	W
p	Position of maximum camber	
Re	Reynolds number	
S	Surface	m^2
t	Thickness	
t	Time	s
v, **v**	Velocity	m/s
x	Vector of design variables	
x,y,z	Cartesian coordinates	
y^+	Dimensionless wall distance	

Greek symbol	Definition	Unit
α	Angle of attack	deg
Γ	Surface	
δ	Angle of deflection	deg
ϵ	Turbulent dissipation rate	
κ	Curvature	
μ	Viscosity	Pa s
ρ	Density	kg/m^3
τ	Shear stress	Pa
Ω	Volume	
ω	Turbulence kinetic energy	

Super-/subscripts	Definition
D	Drag
des	Design
f	Flap
L	Lift
m	Pitching moment (subscript)
m	Main element (superscript)
max	Maximum
min	Minimum
obj	Objective
p	Pressure

Super-/subscripts	Definition
$surf$	Surface
v	Viscous
vol	Volume
w	Wind or wall
∞	Freestream conditions

List of Figures

List of Tables

1

Introduction

The climate change is currently a global threat to human kind and the Earth's environment. The average surface temperature has risen significantly in the last century as well as the globally averaged sea level. Several studies such as [13] show that the increase in greenhouse gases in the atmosphere are likely to be the main cause of the mentioned effects, as a clear correlation is observed from Figure 1.1. The greenhouse gases such as CO_2, CH_4 and N_2O are released to the atmosphere by human kind through various industrial sectors, where the energy industry is one the most contributing sector. Moreover, said industry is growing steadily since the need for energy increases every year, according to the International Energy Agency the global energy demand will rise by 30% by 2040. In order to meet the growing energy demand while reducing the emissions of gas contributing to the global warming, renewable sources will necessarily lead the energy industry in the future. Such transition from the fossil fuel based sources of energy to sustainable energy is commonly referred as energy transition.

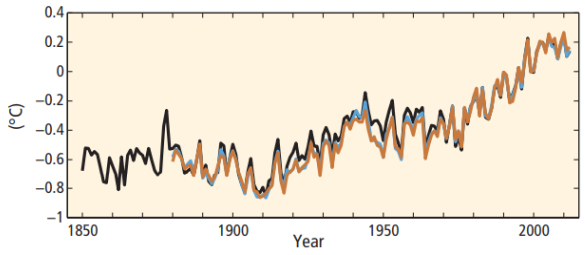

(a) Annually and globally averaged combined land and ocean surface temperature anomalies relative to the mean over the period 1986-2005.

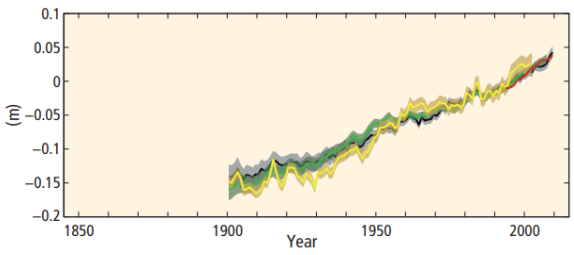

(b) Annually and globally averaged sea level change relative to the average over the period 1986 to 2005 in the longest-running dataset.

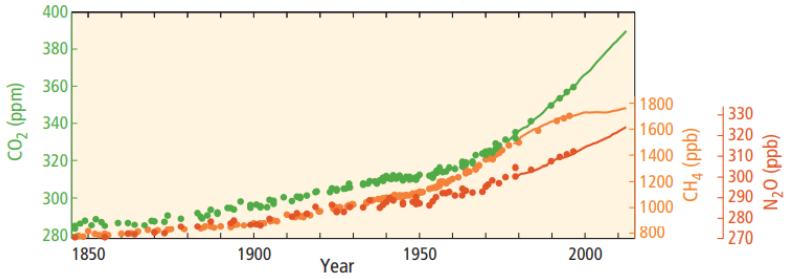

(c) Atmospheric concentrations of the greenhouse gases carbon dioxide (CO2, green), methane (CH4, orange) and nitrous oxide (N2O, red) determined from ice core data (dots) and from direct atmospheric measurements (lines).

Figure 1.1: Observations of a changing global climate system, the colours in (a) and (b) indicate different data sets. From [13]

Nowadays, wind energy plays a paramount role in the energy transition, providing clean and renewable energy to the grid. Such energy source is traditionally harvested through conventional horizontal axis wind turbines (HAWT). However, a relatively new field in wind energy has arisen known

as Airborne Wind Energy (AWE) which will be part of the solution to accelerate the energy transition. AWE is a term that encompasses a wide variety of systems that aim to convert wind energy into electricity. The common denominator among these systems is the use of one or multiple flying devices (ideally autonomous) tethered to the ground, where the tether's utility is to transfer either mechanical or electrical power. One implementation of such technology consists on using the pulling force done by the kite tethered to a ground-based generator. The kite is operated in pumping cycles, alternating between two phases: reel-out and reel-in. During reel-out, the kite flies in cross-wind manoeuvres and the pulling force on the tether applies a torque on the ground-based drum which is converted into electrical power. During reel-in, cross-wind operation is halted and the kite is flown back to the initial position, to start the reel-out phase again. Such technology is further introduced in Section 2.1.1 and a detailed description can be found in [3] by Ahrens, Diehl and Schmehl.

The electric energy produced by conventional wind turbines still has a significant carbon dioxide footprint mainly resulting from the construction of the plant and materials used. AWE systems can drastically reduce such carbon dioxide footprint since it requires only a small fraction of the construction materials and can therefore further reduce the environmental impact. Another advantage of AWE that makes it a potential industry to bolster the energy transition is the higher operational heights, where stronger and more reliable winds are found. Therefore leading to higher capacity factors (CFs) and lower Levelized Cost of Electricity (LCOE). In addition, sites that might not be suitable for HAWT systems are made accessible for AWE. All these circumstances have lead multiple research institutes and companies worldwide to study and develop Airborne Wind Energy systems. The current work is part of the design phase of a kite system for Kitemill AS.

Kitemill AS is a company developing an airborne wind energy system, it employs a rigid kite in ground-gen operation or pumping cycle, i.e., the kite transfers mechanical energy through the tether and it is converted into electrical energy in the ground station. During the reel-out phase, the kite flies crosswind in circular motion, thus following a helical trajectory. In reel-in phase, the kite is depowered and flown back to restart the power cycle. The flying device is an eVTOL drone, with the typical components of an aircraft: wing, fuselage and tail and the additional VTOL propellers. Such propellers can also provide forward thrust since they can rotate and are folded during flight to reduce the kite drag.

The kite design of an AWE system strives towards achieving a high lift, among other design goals. High lifting capabilities are greatly beneficial since they increase the pulling force on the tether which increase the available power output. For low wind conditions, high lift is very significant since it allows the system to reduce the cut-in wind speed, therefore increasing the system capacity factor. Moreover, notice that the C_L/C_D ratio of an AWE system is limited by the unavoidable tether drag, which has a significant contribution to the whole system drag, thus making the lift maximization even more crucial. A relevant difference between an AWE kite and a conventional aircraft (general aviation) is that an AWE kite employs a tether to transfer the loads which are generally significantly higher than gravitational and inertial forces acting on a conventional aircraft. Thus making the design requirements of an AWE kite substantially different wrt a conventional aircraft. Taking all into consideration, the wing of a rigid AWE system requires a multi-element airfoil, which provides higher lift forces and delays stall to higher angles of attack in comparison to single-element airfoils. Such preference for multi-element airfoils in the AWE field is clearly seen through the companies' designs, where most AWE companies that operate with rigid wings make use of multi-element airfoils, some examples are Makani [27], Ampyx Power [65], Skypull [15] or Kitekraft [26, 6].

The aim of the present thesis is to design through optimization a multi-element airfoil for a rigid kite to harvest wind energy and to verify its performance through CFD simulations. Since the kite for which the airfoil is designed operates in ground-gen mode, it has distinct phases, i.e.. production phase and return phase and therefore, the airfoil must fulfill multiple requirements concerning the various operational phases. In general terms, the airfoil must reach high lift values during production phase but should be able to operate with low loads during return phase, in order to maximize the overall power output.

The thesis report is structured as follows. The following Chapter 2 provides the literature study,

divided in two main sections. First, section 2.1 gives the theoretical fundamentals of several key topics treated in the thesis: Airborne Wind Energy, theory of fluid dynamics and high lift aerodynamics and the optimization algorithm: Genetic Algorithm. Then section 2.2 provides an overview of the state of the art of airfoil optimization both within general aviation field as well as in the AWE field. Then, Chapter 3 describes the overall methodology employed for the present thesis, which is divided in two main blocks. The first block is presented in Chapter 4 where the whole optimization of the two-element airfoil is developed and its results are shown. Following, the second main block, Chapter 5, describes the CFD setup and presents the results of the verification. Lastly, the thesis is rounded off with Chapter 6, where the conclusions and recommendations for future work are presented. The work plan for the thesis can be found in the Appendix A through a Gantt diagram.

2

Literature Study

2.1. Fundamentals

The current section provides an overview of the theoretical fundamentals treated in the present thesis. First, an introduction to Airborne Wind Energy is given, explaining its working principle, the existing types of operation and its potential to contribute to the energy transition. An introduction of fluid dynamics and high lift aerodynamics is then provided describing how multi-elements airfoils reach higher lift and why are they required for the AWE field. Lastly, this section is completed with information about the optimization algorithm employed in the present thesis: Genetic Algorithm (GA).

2.1.1. Airborne Wind Energy

Although the main source of energy nowadays is still based on fossil fuels, renewable energy has been increasing its contribution to the grid over the last decades. This transition is paramount for a sustainable development and one of the main energy sources that plays a role in such transition is wind energy. Wind energy is currently being harnessed mainly through conventional horizontal axis wind turbines (HAWT), however, a new technology is currently being developed and commercialized by both research institutions and companies, such technology is Airborne wind energy (AWE) [3].

Concept and working principle

Airborne Wind Energy is a technology for harvesting high altitude wind energy using tethered flying devices, such idea was extensively described by Loyd in 1980 [46]. The system consists of three main components: a kite, a tether and a ground station, depicted in Figure 2.1. The tethered flying device or kite can either be a rigid/fixed wing, a flexible kite or a hybrid concept, where the rigid wing concept is considered for the current thesis.

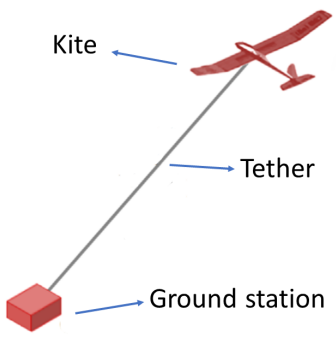

Figure 2.1: Components of an Airborne Wind energy system, adapted from [12].

There are two main ways available to harvest high-altitude wind energy:

- Onboard generation or fly-gen: the generation of energy takes place onboard of the kite through the use of turbines and is transmitted to the ground station through a conducting tether. See Figure 2.2, left.
- Ground based generation or ground-gen: the aerodynamic force on the flying device when flying crosswind acts as a pulling force on the tether, effectively reeling out the tether from the drum, that drives the generator converting mechanical power into electric power. For this concept, the kite must fly back once the maximum tether length is reached where the aim is to depower (i.e. reduce the loads of) the kite, such that the energy consumed to bring back the kite is minimum. This phase consumes a small fraction of the energy produced during reel-out. The phase where the kite is reeled out is referred as energy production or traction phase and the phase where the kite is reeled in is the energy consumption or return phase. Since the operation consists of a periodic reel-out and reel-in it is also referred as pumping mode or yoyo mode. See Figure 2.2, middle (production phase) and right (return phase).

The latter mode is the focus of the current thesis.

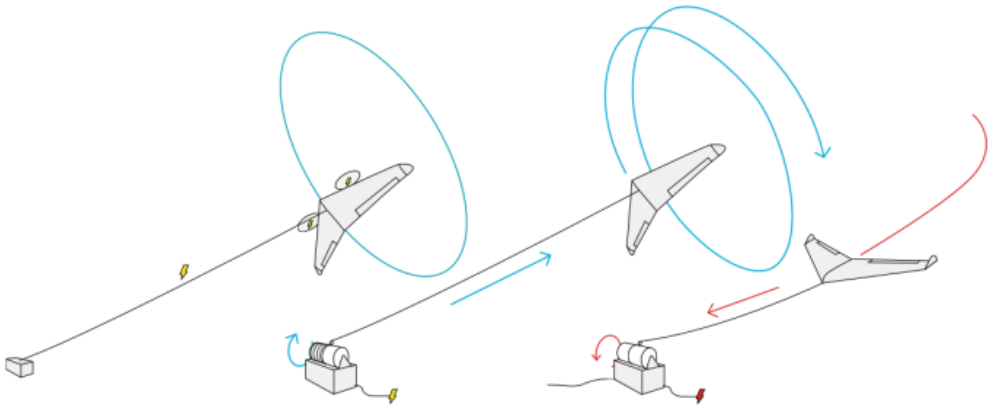

Figure 2.2: Onboard generation (left) and ground based generation (middle and right) AWE concepts, adapted from [73].

The pumping cycle realized by the ground-gen concepts can be visualized through the example in Figure 2.3 where the instantaneous power during both phases (production and return phase) is shown. Note that in the present thesis an airfoil will be designed taking into consideration the requirements for both phases.

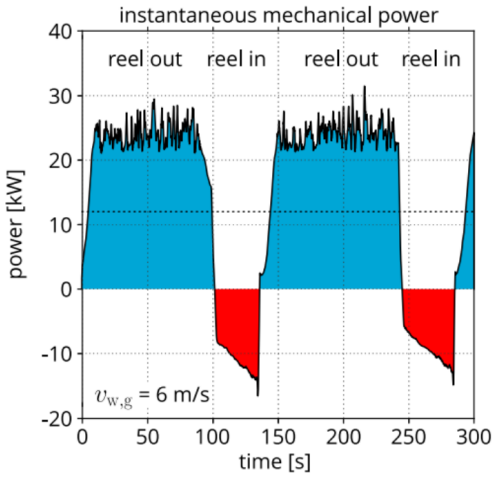

Figure 2.3: Representation of power generation for a ground-generating reeling tether device, from [3].

The potential of AWE was first introduced by Loyd [46] where the available power output of a kite flying crosswind was computed by the following equation,

$$P = \frac{2}{27}\rho S v_w^3 \frac{c_L^3}{c_D^2} \tag{2.1}$$

where ρ is the fluid density, S the wing reference surface, v_w the freestream wind speed and c_L and c_D the lift and drag coefficients of the system respectively. Such equation is the foundation for crosswind kite power. Notice that the available power scales with the factor c_L^3/c_D^2, referred as power coefficient, a significant parameter that will be taken into account in the airfoil optimization procedure.

Potential of AWE and challenges

Airborne wind energy has several advantages with respect to conventional wind energy (mainly harvested through HAWT):

- A very significant advantage of AWE is the reduction of material usage compared to HAWT. In the case of a HAWT, the tower and blades are cantilever beams, which makes them relatively inefficient structures which is compensated with high material usage and a heavy concrete foundation, [14]. On the other hand, an AWE system can replace all that structure with three main components: a kite, a tether and a ground station. This drastically reduces the structural mass and therefore, the cost of two systems with a similar power output. Moreover, the reduction of mass reduces the environmental impact, AWE has at least 40% lower carbon intensity than established wind technology, [50].
- Another advantage is that AWE systems operate at higher altitudes, where the wind is stronger and more consistent, increasing capacity factors. The reason why the wind speed is higher at higher altitudes is based on the wind boundary layer on the earth's surface, referred to as atmospheric boundary layer. Such effect is depicted in Figure 2.4, where a higher average wind speed is shown at a higher altitude in Europe.
- Lastly, AWE systems have an adaptive operational height since the kite can be flown at any desired height. Such feature can lead to a higher capacity factor since the system can be operated at the most suitable height while HAWT are constrained to their hub height.

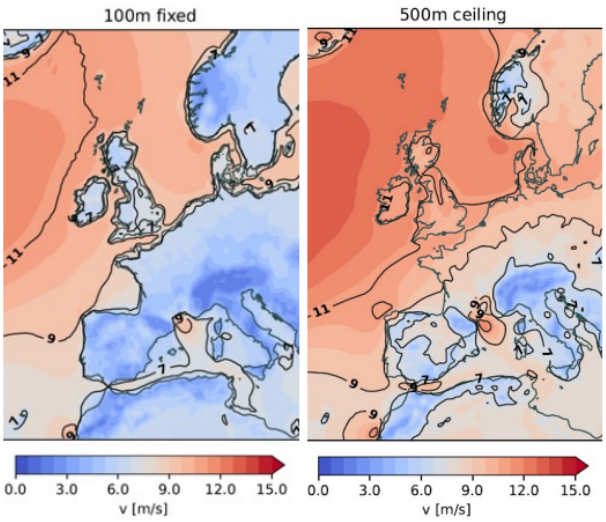

Figure 2.4: Average wind speed at 100m fixed and 500m ceiling above ground level, from [4].

It is true, however, that such technology is in development and early commercialization phase and has several challenges to overcome. A relevant one is to achieve fully automated operation for all the stages: take-off, production, retraction, transitions and landing (although some of these phases

are not required for the fly-gen mode). Such autonomous operation should be durable and reliable, moreover, another relevant challenge to take into account is that regulatory requirements must be established. That being said, AWE has very significant advantages making it a potential technology to contribute to the energy transition leading to multiple companies and institutions to develop such technology.

2.1.2. Fluid dynamics

The motion of a fluid within a confined volume is described by the conservation laws, i.e, conservation of mass, momentum and energy. The conservation of mass dictates that any change of mass within a control volume Ω is equal to the flow over its surface Γ:

$$\frac{\partial}{\partial t}\int_{\Omega}\rho d\Omega = -\int_{\Gamma}\rho \mathbf{v}\cdot\mathbf{n}d\Gamma. \tag{2.2}$$

The right hand side quantifies how much fluid with velocity **v** is traversing the volume surface Γ defined by the normal vector **n** and the left hand side is the time variation of mass in the control volume Ω, where the ρ is the fluid density.

The conservation of momentum states that that time rate change of the system momentum is equal to the sum of all external forces, according to Newton's second law. The momentum of the system is split into the change of momentum in the control volume and the amount of momentum that crosses through the volume's surface Γ. Leading to the equation

$$\frac{\partial}{\partial t}\int_{\Omega}\mathbf{v}\rho d\Omega + \int_{\Gamma}\mathbf{v}\rho\mathbf{v}\cdot\mathbf{n}d\Gamma = \sum_{\Omega}F_{vol} + \sum_{\Gamma}F_{surf}, \tag{2.3}$$

where F_{vol} refers to the volume forces such as the gravitational force and F_{surf} refers to surface forces such as the pressure. Lastly, the conservation of energy states that the energy is not created nor destroyed, thus, the total energy in a volume and crossing over its surface is equal to all the heat, Q or work, W transferred into the system:

$$\frac{\partial}{\partial t}\int_{\Omega}e\rho d\Omega + \int_{\Gamma}e\rho\mathbf{v}\cdot\mathbf{n}d\Gamma = \dot{Q}_{\Omega} + \dot{W}_{\Omega} \tag{2.4}$$

where e is the mass-specific energy. The presented equations consist of a system of partial differential equations known as the *Navier-Stokes equations*. Such equations can be simplified by imposing the assumption of inviscid flow, by doing so, the Euler equations are obtained. Even though neglecting viscosity may seem to limit significantly the applicability of the Euler equations, they have been shown to be a good approximation for external flows i.e. outside the boundary layer [36].

Boundary layer theory

The boundary layer theory allows us to describe the flow behaviour in the vicinity of an object's surface, e.g. an airfoil, where the viscosity of the fluid dominates the flow behaviour. Such concept completes the inviscid formulation given by the Euler equations. The viscosity, μ is a physical property of a fluid that relates the wall shear stress τ_w to the gradient of flow velocity parallel to the surface in the normal direction:

$$\tau_w = \mu\frac{du}{dy}. \tag{2.5}$$

The Reynolds number, Re is a dimensionless number that gives the ratio of inertial forces to viscous forces,

$$Re = \frac{\rho v l}{\mu}, \tag{2.6}$$

where l is a characteristic length of the problem. Said number is employed to characterize the boundary layer, a flow can be categorized as laminar or turbulent given its Re and Ma (where the Mach number, Ma gives the ratio between the flow speed and the sound speed). Laminar flow is

characterized by the fluid motion being structured in parallel planes, where there is no significant exchange of flow properties in the direction perpendicular to the flow. On the other hand, turbulent flow shows a chaotic flow motion, with strong interaction within the flow. Such distinction is relevant since each type of flow behaves differently, and thus the aerodynamic properties of an airfoil are conditioned on the type of flow in the boundary layer. A turbulent BL has a higher velocity gradient on the wall, thus higher wall shear stress, leading to a higher friction drag, nonetheless, it can be beneficial for delaying flow separation, a phenomena described later in this section. The transition from laminar flow to turbulent flow in the boundary layer occurs due to instabilities in the flow. Assuming, the BL starts with laminar flow from the leading edge, its thickness will increase until the transition point is reached, where the laminar flow becomes turbulent. Such transition depends mainly on the turbulence intensity of the outer flow and the object's surface roughness. If the surface is rough or dirty, the turbulent BL can be triggered from the leading edge.

The pressure on the surface is mostly imposed by the external flow, i.e., the gradient of pressure in the direction normal to the surface in the BL is very small. Hence, the pressure in the BL mainly varies in the flow direction, the usually employed parameter for the pressure around an airfoil is the pressure coefficient, c_p,

$$c_p = \frac{p - p_\infty}{\frac{1}{2}\rho v}. \tag{2.7}$$

Where p_∞ is the pressure of the flow in the freestream and p is the pressure at a given location on the airfoil's surface. The kinetic energy of a boundary layer along an airfoil surface decreases due to an adverse pressure gradient, i,e, an increase of pressure. Such reduction of velocity is depicted in Figure 2.5 by the decreasing velocity gradient of streamlines close to the surface. If the increasing pressure is too high such that the kinetic energy is not sufficient to overcome it, the particles near the wall stop (indicated in Figure 2.5 by the separation point S) and start going upstream, leading to a separated flow. Therefore, such phenomena occurs for cases with strong pressure gradients, which can be caused by the airfoil geometry or a high angle of attack. The pressure coefficient along an airfoil surface usually depicts flow separation through a flat plateau, since the pressure remains rather constant downstream of the separation point. The consequence of detached flow is a clear drop in lift and increase of pressure drag, i.e, stall.

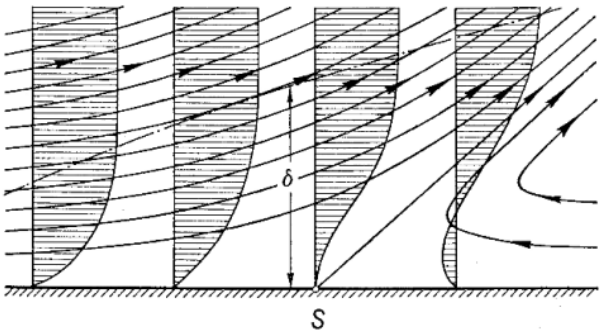

Figure 2.5: Schematic BL profiles when flow separation occurs, [56].

2.1.3. High-lift aerodynamics

High lift aerodynamics have been widely studied mainly due to its paramount importance in the commercial aviation industry, where take off and landing require of high lifting capabilities. A high lifting airfoil can be achieved through various measures in the design, where the goal is to ensure attached flow as far as possible, i.e., delay flow separation. A possible approach is to design the airfoil suction surface such that a steep pressure gradient is avoided, [39]. However, a more effective approach to reach higher lift forces is to employ a multi-element airfoil, usually a flap, a rear element and/or a slat, a front element. The aerodynamic mechanisms that allow multi-element airfoils to reach higher lift were extensively described by A.M.O. Smith in [59], such mechanisms are hereby introduced:

1. Slat effect or front element effect: A slat produces its own circulation, therefore inducing certain flow velocity in the vicinity of the leading edge of the downstream element. Such velocity runs counter to the flow velocity on the downstream element thus reducing the suction peak on said element. A reduction of the suction peak leads to a less steep adverse pressure gradient preventing flow separation.
2. Dumping effect: Since the trailing edge of an upstream element is located in a region where the flow velocity is higher than the freestream, the boundary layer is dumped at a high velocity. Due to such higher velocity the pressure rise along the airfoil is relieved and hence, flow separation is prevented or higher lift is allowed.
3. Off-the-surface pressure recovery: Since the boundary layer of a forward element is dumped at a velocity higher than the freestream velocity, the final deceleration of the boundary layer to freestream velocity takes place out of contact with the wall. Such deceleration method is more effective than a deceleration in contact with the wall.
4. Fresh boundary layer effect: The gap between the elements, for instance the gap between the main element and the flap makes the flap boundary layer completely new. That means that such boundary layer will be much thinner than if it came from the main element and a thin boundary layer can withstand stronger adverse pressure gradients than thick ones. Therefore, flow separation is prevented by allowing a fresh boundary layer along the flap.

The overall consequence of all the mentioned effects of having a slotted airfoil is that the airfoil will reach higher lift coefficients and the angle of attack of stall will be delayed. These effects of the rear element to its front element and viceversa are relevant to understand the interaction between the elements that lead to an increase of lift and delay of stall.

The high lifting capabilities are greatly beneficial for the AWE technology. Let us consider the ground-gen operation, which is the focus of the current thesis. The generated power is achieved by pulling the tether with a certain force, resulting from the aerodynamic loads on the kite. In order to maximize such force, the operational C_L must therefore be as high as possible, leading to the necessity of multi-element airfoils in the AWE industry. Other authors working on AWE have also inferred that the C_L must be maximized to maximize the available power, some examples are Makani in [27] and Bauer [6], where such hypothesis is derived from Loyd's model.

2.1.4. Optimization algorithm

This section provides an overview of the optimization algorithm employed in the present thesis. Among all the available optimization methods, the Genetic algorithm has been chosen. The theory supporting such algorithm and the reasons that have led us to select it as well as its drawbacks are hereby described.

Numerous great inventions have been the result of bionics, i.e., the application of biological or natural principles to the study and design of human systems. The natural evolution of species could be seen as a process of adapting to the environment and optimizing the fitness of the species. This same principle could be imitated to design an algorithm, giving place to evolutionary algorithms (EA). Genetic algorithms are a type of optimization algorithms included in the group of the Evolutionary Algorithms, extensively presented in [58, 72]. Such algorithms consist of optimization techniques based on a biological phenomena: evolution. EA's are meta-heuristic approaches with the ability to evolve and learn from the problem, all EA's have three characteristics in common, as specified in [72]:

- Population-based. EA's maintain a group of solutions or individuals, called a population, to optimize the problem in a parallel manner.
- Fitness-oriented. Every individual in a population is evaluated by computing its fitness value, which is given by the objective function or fitness function. EA's will favour fitter individuals, which is the foundation of the optimization and convergence of the algorithms.
- Variation-driven. When constructing a new population, the individuals from previous populations will undergo a certain type of variations, which is fundamental to searching the solution space.

Genetic algorithm

The structure of a GA consists on three main steps, closely related to the three characteristics of EA's presented in the previous section.

The first step is **initialization**. A GA operates on a group of individuals, therefore, we need to generate an initial population to begin the evolving process. In general, the number of individuals for the first (and subsequent) populations is given by the designer. The question then is how to create such first population, for some cases the part of the design space with better solutions is known, however, for most cases a blind search over the whole design domain is preferred. Therefore, a random initialization of the population can be done. Such random distribution of individuals makes sure to have a representative individual of every part of the design space and therefore, decrease the chance of missing a potential design.

The following step is **selection**. After the GA has initialized the first population, it enters the main loop, which starts with the selection process. Such process mimics natural selection by granting fitter individuals higher opportunity to breed, where 'fitter' means 'with a higher value of objective function/s or fitness function/s', or lower if the goal is to minimize. Therefore, an individual's chance of being selected to produce offspring, i.e. the next population, is related to its fitness.

Finally, the last step is **variation**. With the selected individuals in the previous step, the aim now is to create a new population from them. Generally, there are two main variation operators that give place to the new population: crossover and mutation. Crossover is the main exploration mechanism of a GA, it consists on mixing the properties of multiple individuals to create a new one. On the other hand, mutation consists on slightly changing randomly a property of an individual. These two variation mechanisms imitate natural reproduction. The Matlab function employed in this thesis to run the GA [28] has a third way to generate an offspring population: eliteare. It consists on automatically passing the best individuals on to the next generation. The three variations methods are depicted in Figure 2.6.

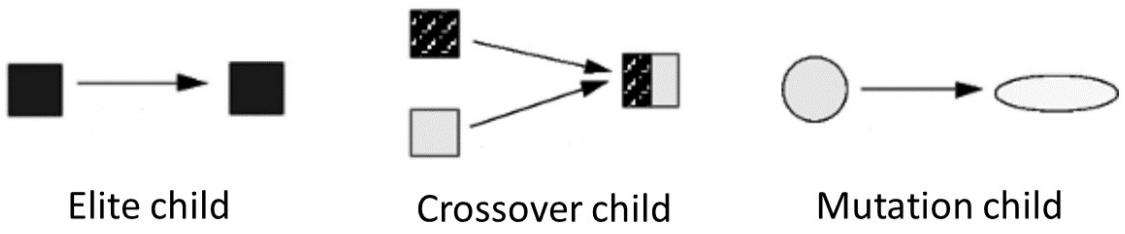

Figure 2.6: Variation methods of a GA, adapted from [69].

A GA has been selected among a wide variety of optimization algorithms due to its suitability for our optimization problem. As will be shown in the Previous work section 2.2, other methods have been employed in the multi-element airfoil design work, however the later works on airfoil design for the AWE sector show a clear preference for evolutionary algorithms, specifically GA's. Multi-element airfoil design is a highly non-linear problem and therefore there are significant coupling effects between the design variables that define the airfoil geometry. The strong coupling leads us to move away from algorithms that evaluate one-parameter-at-a-time (unless small time and resources are available). On the other hand, the non-linearity of the design space and its possibility of having local optimas make GA a preferred option rather than a gradient-based algorithm. While a gradient-based algorithm may be driven by the derivatives information towards a local optima instead of a global optima, a GA is known to be more reliable to find the actual global optima. That is due to its population-based nature, as it has individuals spread all over the design space. Moreover, not requiring sensitivities information makes it appropriate for our design problem since it has been learned form previous experience that certain airfoil geometries analysis will struggle to converge. The capability of finding the global optima in a design space with local optimas is visualized through an example shown in the Figures 2.7 and

2.8, where a comparison of a gradient-based algorithm and a GA is shown. A design space with a clear global optima is shown in Figure 2.7, Figure 2.8a shows that a gradient-based method can be misled towards a local optima according to the where the first point is located. On the other hand, Figure 2.8b depicts how the final population of the GA converges to the global optima. Such example is presented to visually explain how a GA can outperform a gradient-based algorithm in terms of finding the global optima.

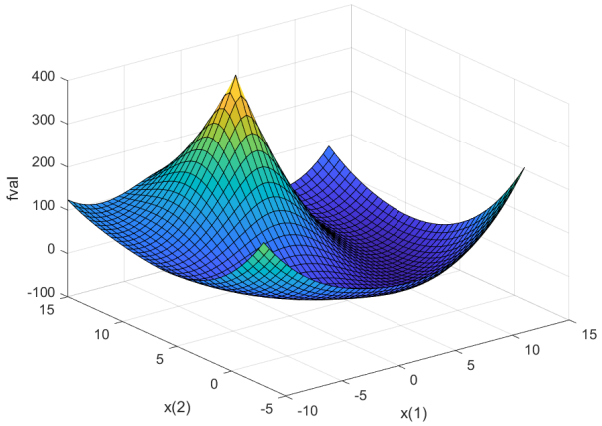

Figure 2.7: Design space.

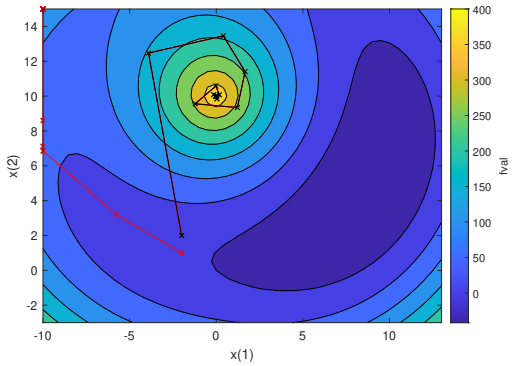

(a) Global optima search by a gradient-based algorithm, one path is mislead towards a local optima while the other successfully finds the global optima. Thus showing dependency on the initial point.

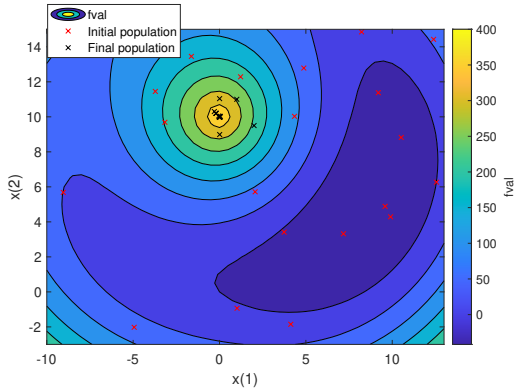

(b) Global optima search by a GA, converging on the global optima.

Figure 2.8: Comparison of a gradient-based algorithm and GA in the search of the global optima.

Another characteristic that made me opt for a GA is its flexible way of dealing with multiple objectives. A GA is capable of computing the pareto front or pareto set, i.e. the set of individuals that can not improve one objective function without having a detrimental effect on the other. In other words, it is the set of airfoils that optimize the objective functions with a compromise between the various objectives. Such set is a great asset when designing an airfoil since the most appropriate compromise among the objective functions can be selected after the optimization run, thus providing a very flexible design process.

A Genetic Algorithm has been selected given its mentioned advantages, more specifically the Non-dominated Sorting Genetic Algorithm II (NSGA-II), from [17] and [18]. NSGA-II is an extension of the GA for multiple objective function optimization , employed by the Matlab function: *gamultiobj*. It should be mentioned that the GA has a significant drawback: its computational cost is high, however,

it is deemed as an acceptable drawback due to other GA benefits. Furthermore, the solver coupled to the GA has a low computational cost, thus reducing the computation time of the overall optimization procedure.

2.2. Previous work

Multi-element airfoil optimization has been widely studied in the aeronautic community mainly for general aviation purposes. Nonetheless, the interest on multi-element airfoils is progressively increasing in the emerging sector of AWE. The present chapter provides an overview of the field of airfoil optimization both within the general aviation sector as well as in the AWE field.

2.2.1. Multi-element airfoil optimization in general aviation

Various methods for airfoil optimization are found in literature, such as inverse design, subdivision of the problem, gradient-based algorithms, evolutionary algorithms or a hybrid type combining some of the mentioned methods. A relevant methodology seen in literature is the inverse design approach for multi-element airfoil optimization, employed in works such as [59, 44, 57]. The inverse design approach consists on finding the airfoil surface geometry as a result of a desired user-given pressure distribution. Such functionality is available in classic tools for airfoil analysis such as XFOIL [20] or MSES. However, said procedure has been deemed as complex since each particular shape has a determinate pressure distribution but not each pressure distribution has a particular shape, as stated by Smith in [59]. Moreover, for multi-element airfoil purposes, the desired pressure distribution along the various elements is not typically known, therefore this methodology is discarded for the present work.

Bortolotti [8] develops an automated procedure for multi-element optimization where the parametrization scheme can be chosen among various options (NACA, IPS and Benzing). This author provides a valuable of comparison of gradient-based algorithms with evolutionary algorithms by developing the optimization procedure with two different algorithms: particle swarm (evolutionary algorithm) and steepest descent (gradient-based). Evolutionary algorithms are emphasized by many authors for airfoil optimization, however, its major drawback lies in their computational efficiency. Therefore, a more traditional alternative that has a lower computational cost is employing a gradient-based algorithm. Such methods are characterized by reaching the optima by navigating through the design domain with the derivatives information. These procedure is proved to efficiently reach the local optima for complex optimization domains, however, it does not ensure to find the global optima. There are various methods within gradient based algorithms such as steepest descent or ascent, employed in [8] and [40], simulated annealing or quasi-Newton method, both used in [71]. Another approach is to employ LINDOP, a gradient based optimization algorithm coupled with MSES as a modelling tool that uses the commonly employed BFGS method [32] to generate the sequence of descent directions. LINDOP was developed by Drela [22] and used to optimize a multi-element airfoil in [23] and [25], it is stated that MSES' ability to produce sensitivity information at little additional cost allowed the optimization algorithm to have a modest computational cost.

Other authors have relied on evolutionary algorithms for airfoil optimization, such as [8, 9, 11, 29, 37] or [34], due to its benefits wrt to gradient-based methods, described in the previous section 2.1.4. In [9], the flap and slat of a three-element airfoil are optimized through a multi-objective genetic algorithm (MOGA) coupled with a CFD RANS solver. Even though the bulk of the optimization is done with a GA, a gradient-based algorithm is used when the GA is close to converging, such approach reduces the number of iterations. Moreover, the human-in-the-loop technique is added, which consists on manually monitoring and guiding the algorithm to accelerate the convergence and produce more engineering applicable solutions.

In the case of [37], a similar optimization is conducted where it is mentioned that coupling a MOGA with a CFD RANS solver leads to optimization runs of the order of days, since each simulation has

a high computational cost. It is also found that the objective function is more sensitive to the design variables describing the relative position of the various elements (i.e., setting) , rather than the shape of each element. As a consequence of such finding, it is suggested to decouple the optimization problem into shape and setting parameters. Such approach introduces another methodology for airfoil optimization, consisting on subdividing the problem into various sets of design variables, or individual design variables (the latter known as one-parameter-at-a-time approach). The optimization is then performed by evaluating the effect of each parameter (or set of parameters) separately. Such methodology simplifies greatly the optimization process, although it comes at an evident price, it disregards the coupling effects between the various design variables which are significant for the case of airfoil design.

A widely accepted approach is the one presented by Benini in [7], which combines the celerity of a lower-fidelity solver with the accuracy of a CFD simulation. Benini proposes to couple an optimization algorithm with a fast low-fidelity aerodynamic solver and perform a verification of the result through a higher fidelity tool such as CFD. He uses said approach to optimize the slat and flap shape and their setting (relative position) of a three-element airfoil to perform efficiently in both take-off and landing. The employed algorithm is a genetic algorithm and the solver is MSES, which shows good agreement with the CFD RANS results. This approach has been employed by various authors in the AWE field, as shown in the following section due to its satisfactory results and the benefits of not coupling the optimization algorithm with a solver with high computational cost. Even though GA has a high computational cost it is commonly chosen for airfoil optimization instead of other algorithms due to its robustness of finding the global optima and for its effectiveness in dealing with a multi objective design. Moreover, not requiring the gradients in the search process is a significant advantage when using a solver that may not converge for all the cases, as concluded in [64], which provides an interesting comparison of GA against other traditional methods in terms of airfoil design.

2.2.2. Airfoil Optimization in the AWE field

Even though the vast majority of research on multi-element airfoil optimization has been performed for the general aviation field, there is currently a good amount of research documents that optimize, design or analyse multi-element airfoils with AWE applications. Before focusing on the multi-element airfoil optimization in the AWE field let us first briefly present the work done for other types of airfoil with AWE applications.

There has been a fair amount of research projects aiming to optimize airfoils for a soft kite system with AWE applications. Three examples known to the author are the projects from Coenen, R [14], Kroon, E [41] and Thedens, P [63]. Even though the type of airfoil is different to what the present work aims to optimize, the mentioned projects are relevant since they follow a similar optimization procedure and have the same application, AWE. For the case of [41] and [14], a single skin airfoil is designed while an airfoil for a RAM-air kite is optimized in [63]. [41] and [63] use a NSGA-II (Non-dominated Sorting Genetic Algorithm) as optimization algorithm with RFOIL as the aerodynamic solver. On the other hand, [14] optmizes through a surrogate modelling technique where the solver to construct the model is CFD RANS simulations. See the Table 2.1, which summarizes the main features of the mentioned projects.

A slightly different study is provided in [55] where a single element airfoil is optimized for an airborne wind turbine. The optimization is performed through a genetic algorithm coupled with XFOIL as the aerodynamic solver. The 3D turbine with the optimized airfoil is then analysed with a CFD RANS solver. The airfoil shape is optimized with the parametrization scheme: PARSEC [33].

If we now focus on the work done specifically on the multi-element airfoils for a rigid kite, a few projects stand out. In [6], Bauer performs an aerodynamic analysis of a four-element airfoil designed for a fly-gen system to demonstrate the feasibility of a very high C_L kite. The study relies on the hypothesis that the system's power, energy yield and the profit margin are maximized by maximizing the kite's lift coefficient, a hypothesis based on an extension of Loyd's model [46]. Although the

main objective of the work is not to optimize the airfoil it provides relevant information for the present work since it provides the geometry and polars of the analysed airfoil, obtained through CFD analysis, shown in Figure 2.9.

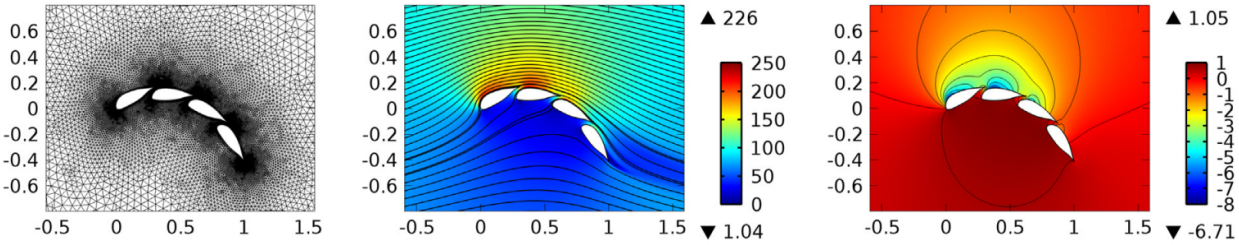

Figure 2.9: Results of the CFD simulation of the multi-element airfoil analysed in [6], showing the mesh (left), velocity field (middle) and pressure coefficient field (right). All space coordinates are in m and all speed values are in m=s

Another reference for multi-element airfoil design in the AWE field is found in [66]. It does not optimize the airfoil either, but it shows an aerodynamic analysis of Ampyx Power's AWE system, including the 3-element airfoil, shown in Figure 2.10a. The aim of the work is to develop and compare two different power prediction models for the kite system. Both models use the results from 2D CFD analysis combining them with the free vortex code AWSM, in one case, and with a nonlinear lifting line in the other case. Such models are then compared to 3D CFD calculations of the whole kite (see Figure 2.10b), showing very good agreement between the power prediction models.

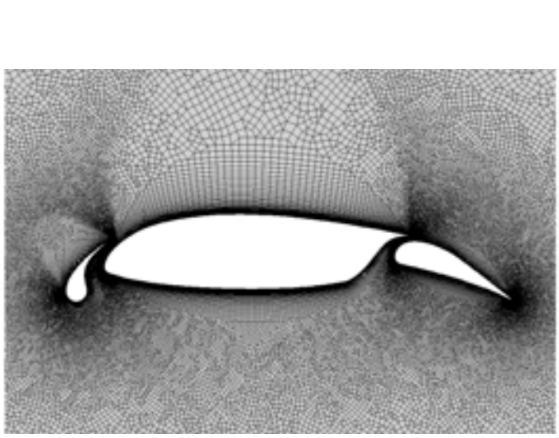

(a) Ampyx Power's 3-element airfoil, shown with its mesh.

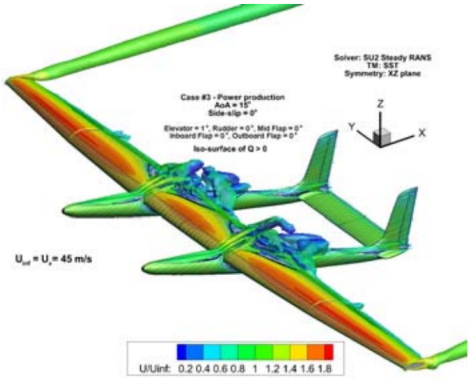

(b) Flow visualization of the 3D CFD simulation of Ampyx Power's kite.

Figure 2.10: Results visualization of Ampyx Power's work on multi-element airfoils, [66].

There are currently three research projects known to the author that have focused on the strict design or optimization of multi-element airfoils aimed for the AWE field: Makani's [27] by Echeverri, P., et al., De Fezza, G [15] for Skypull and Drexler, C [26] for Kitekraft. These three projects are the most relevant to the present thesis due to its similar methodology and/or aim.

The company Makani shared all the documentation regarding technical development of the kite system, including the methodology for airfoil design, [27]. Makani designed a two-element airfoil, shown in Figure 2.11 for their fly-gen AWE system. The method to design it does not employ an optimization algorithm, instead it consists on analysing certain design variables and flow phenomena based on previous experience and the designer's critical thinking, i.e. engineering best practices. The aerodynamic analysis have been done with MSES and the designed airfoil is verified with CFD RANS simulations where considerable discrepancies are found for the predicted drag. This report provides a valuable reasoning of why multi-element airfoils are preferred for an AWE system, mainly justified through the high lift requirements.

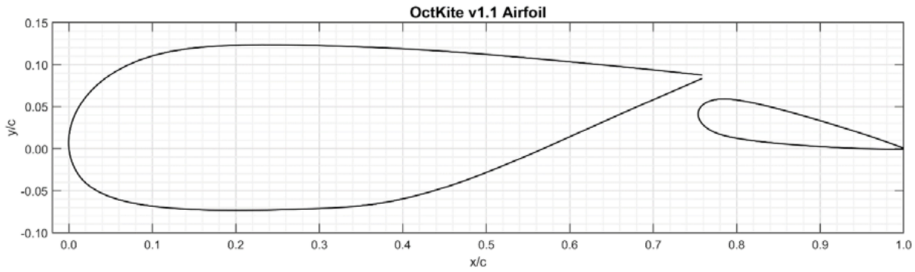

Figure 2.11: Airfoil designed by Makani in [27].

De Fezza, G [15] optimizes a multi-element airfoil for AWE application operating in ground-gen mode. In [15], a four-element airfoil is optimized using an already designed airfoil by [54] as a starting point. Said airfoil is originally aimed for a conventional wind turbine, see Figure 2.12. The optimization considers design variables that describe the relative position of the four elements and optimizes them by varying one parameter at a time and evaluating its effect to the performance individually through CFD RANS simulations. Such approach is preferred in [15] instead of an optimization algorithm in order to better understand the aerodynamics of the airfoil, as stated by the author. Moreover, each CFD simulation is manually meshed so coupling the solver with an automatic algorithm would not be feasible. The main drawback of the one-parameter-at-a-time approach is that coupling effects between the various variables are not captured. However, it facilitates employing CFD as a solver which has the significant benefit that a higher accuracy can be expected wrt lower fidelity solvers. The results with CFD are compared to MSES results and, as found by Echeverri, P [27], MSES and CFD's results diverge significantly. Said work optimizes the airfoil for production phase, focusing on the power coefficient, C_L^3/C_D^2.

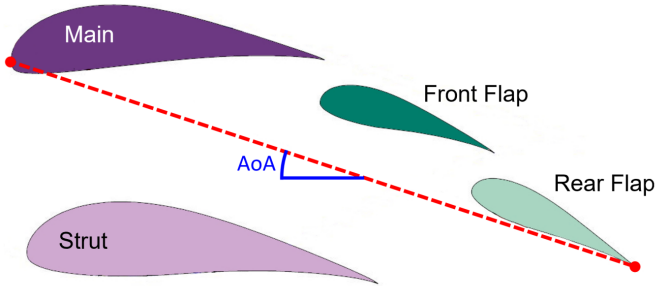

Figure 2.12: Multi-element airfoil developed by [54], employed by [15] as a baseline for the optimization.

Lastly, Drexler's work optimizes a single and two-element airfoil through a widely accepted and used method presented by Benini [7]. As previously mentioned such method consists on coupling a low-fidelity tool for aerodynamic analysis, MSES [21], to an optimization algorithm and employing a CFD RANS solver, for the posterior verification of the found optimal airfoil. This method harnesses the accuracy of a high fidelity solver, CFD RANS analysis combined with the celerity of a low-fidelity solver, i.e. the computational cost is drastically reduced. The optimization algorithm employed by Drexler is the Covariance Matrix Adaptation Evolution Strategy (CMA-ES), an evolutionary algorithm. Both the shape and relative position of the two elements are optimized, where the parametrization of each element's shape is done through cubic spline interpolation. Certain issues related to convergence of the MSES analysis are mentioned, which are mitigated by including convergence indicators into the cost function of the optimization. The results from MSES are then verified with CFD and the results show a significant discrepancy, due to flow separation taking place for the CFD analysis. However, the CFD analysis have been done in 3D, in contrast to the 2D MSES analysis, so the discrepancies due to flow separation that takes place in the CFD simulation might be even greater. Said work represents a good base for the current thesis since the methodology is quite similar, although the goal of the optimization differs due to different modes of operation. The current work optimizes for an AWE system operating in ground-gen mode whereas the airfoil optimization by Drexler is aimed

for a fly-gen system. Therefore, in Drexler's design, the airfoil design does not require to take into account the return phase, as will be done in the present thesis.

Table 2.1 shows a summary of the research projects related to airfoil optimization/design in the AWE field.

Research project	Airfoil type	Optimization method	Aero Solver	Parametrization
Coenen, R [14]	Single skin airfoil	Surrogate modelling	CFD RANS	NACA based
Kroon, E [41]	Single skin airfoil	NSGA II (OptiFlow [16])	RFOIL	CST
Thedens, P [63]	Ram-air airfoil	NSGA II	RFOIL	CST
Saleem, A [55]	1-element airfoil	GA	XFOIL + CFD RANS verif.	PARSEC
Echeverri, P., et al. [27]	2-element airfoil	Eng. best practices, 1-parameter-at-a-time	MSES + CFD RANS verif.	-
De Fezza, G [15]	4-element airfoil	1 parameter-at-a-time	CFD RANS MSES verif.	Relative position
Drexler, C [26]	1 and 2-element airfoil	CMA-ES (Evolutionary algorithm)	MSES + CFD RANS verif.	Cubic spline interpolation

Table 2.1: Summary of work related to airfoil design in the AWE field.

2.3. Research objectives and research questions

The described literature study provides a solid base for the present work and leaves certain research questions to be explored. This section describes the objective of the present thesis and the research questions that will be answered by pursuing said objective.

The objective of the thesis is to optimize a two-element airfoil for a rigid AWE kite. Said kite operates in pumping cycle, therefore, the two main operational phases must be taken into account: production phase and return phase, which have significantly different requirements and design goals. Therefore, the designed airfoil will have a different setting/configuration for each operational phase, attained through a movable flap. A highly automated optimization procedure based on a genetic algorithm will be developed, coupled with MSES as the aerodynamic solver. Lastly, the aerodynamic performance of the resulting airfoil will be verified through a CFD RANS solver to analyse the discrepancies and assess the accuracy of MSES.

The research questions deriving from the described objective are the following:

- What shape parametrization method is most suitable for the optimization procedure?
- Is the genetic algorithm a suitable optimization algorithm for our design goal?
- What are the benefits and limitations of employing MSES as the solver coupled to the optimization algorithm?
  - To what extent can we employ MSES?
  - Does MSES allow to fully automate the optimization algorithm?
  - How does it compare to a high fidelity solver, e.g. a CFD RANS solver?
- How should the airfoil vary its flap setting, i.e. relative position, to fulfill the requirements of both production and return phase?
  - What are the suitable objective functions to employ for each operational phase?

- Since the kite wing will be subject to high loads, the relative position of the airfoil elements will vary due to the spanwise wing bending, how does this relative position variation alter the aerodynamic performance?

3

Methodology

The selected method for optimizing the two-element airfoil is the one presented by [7] and commonly employed in multi-element airfoil optimization. A Multi Objective Genetic Algorithm is coupled with MSES as the aerodynamic solver in order to optimize the airfoil. After the optimization procedure, the aerodynamic performance of the resulting airfoil will be verified through a high fidelity solver: a CFD RANS simulation. Therefore, the present thesis is divided into two main blocks: optimization and design of the multi-element airfoil, and verification of the results.

In the first block, the genetic algorithm will be employed to optimize the multi-element airfoil shape and setting (elements relative position) for the production phase. Such procedure requires first to define a suitable parametrization scheme, i.e., the variables that fully define the geometry of the airfoil. The parametrization should be selected such that the number of design variables is low while maintaining enough flexibility and shape control of the regions of interest, where the integration of the flap has been given certain emphasis. The goals of the optimization must also be defined, which determine the objective functions to feed to the optimization algorithm. These objective functions are driven to optimizing the airfoil for production phase, i.e. maximizing the available power output in said phase. The coupling between the genetic algorithm and the aerodynamic solver will be done through Matlab, where the GA is implemented and is capable of executing all the MSES programs from the terminal. The resulting airfoil will then be evaluated for return phase and modified to achieve an efficient performance in both phases. To fulfill so, the airfoil will have a different flap setting for each phase, leading to a designed airfoil with two different configurations. Production and return phase have very different requirements on the airfoil since a high lift is required in production (among other requirements) while low loads are desired for return phase. Such different requirements are what makes airfoil design for an AWE system in ground-gen mode a challenging engineering problem.

The second block consists on verifying the aerodynamic performance of the resulting airfoil from the previous block. To do so, a CFD RANS solver is used with the open source software OpenFoam. The software employed to mesh the geometry is Cadence (current name for Pointwise) and for post processing the flow visualization software Paraview is used as well as Matlab scripts for data treatment. The CFD setup will be validated with the experimental data of a single element airfoil to benchmark the setup and assess its accuracy. The aim of this block is to compare the analysis results of a high-fidelity solver such as CFD RANS with the results obtained from MSES, theoretically a lower-fidelity tool but with a significant lower computational cost. The polars verification will be performed for both airfoil configurations, furthermore, the flowfield will also be compared to assess how flow separation is captured with both tools.

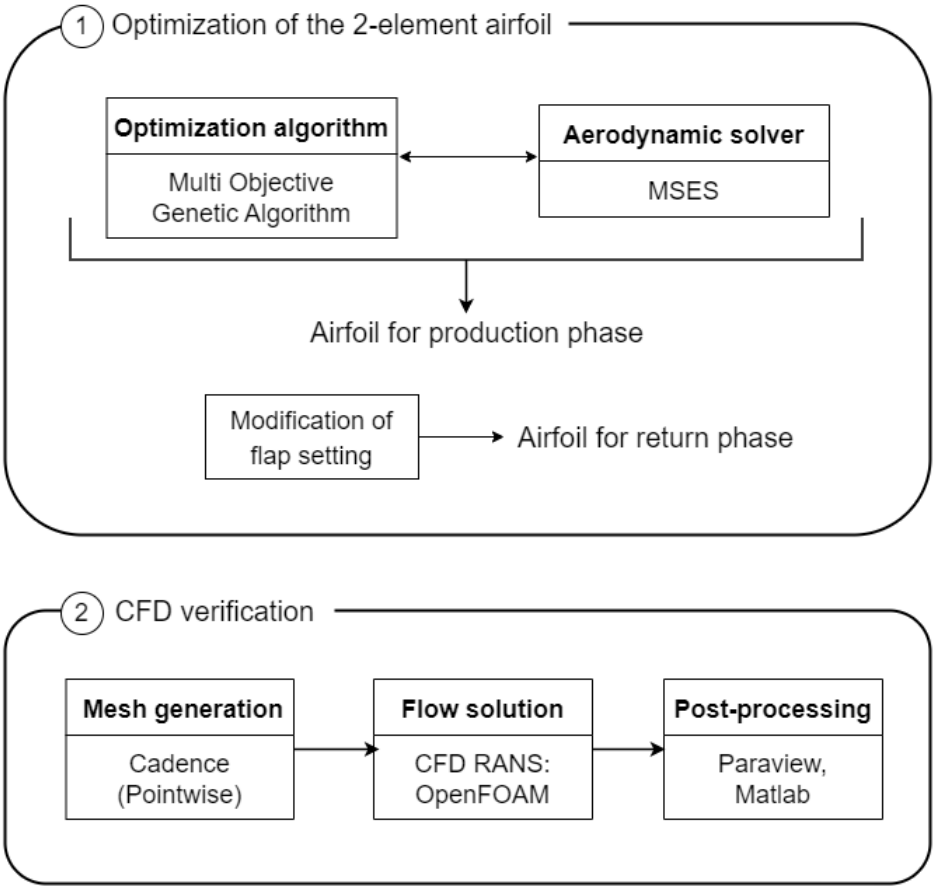

Figure 3.1: Diagram of the methodology with the two main blocks outlined.

4

Multi-element airfoil optimization procedure

The selected method for optimizing the airfoil is the one presented by [7] and commonly employed in multi-element airfoil optimization. A Multi Objective Genetic Algorithm is coupled with MSES as the aerodynamic solver in order to optimize the airfoil for production phase. The resulting airfoil will be evaluated for return phase and modified to achieve an efficient performance in both phases, to fulfill so, the airfoil will have a different flap setting for each phase.

4.1. Parametrization scheme

Parametrization consists on determining certain parameters or design variables that fully define the geometry of the multi-element airfoil, these variables are the parameters to be optimized. In order to define the geometry of a multi-element airfoil, two types of design variables are distinguished: shape variables and setting variables. The shape design variables define the shape of each individual element and the setting variables define the configuration and relative position of each element. The selection of these variables are paramount to the optimization scheme since they will determine the flexibility of the design and hence, how far the optimization can reach.

The shape parametrization of an airfoil can be achieved through various schemes, the most commonly employed being: NACA airfoils [1, 38], CST coefficients [42, 43], PARSEC [33] or IGP [47]. The NACA 4-series defines the airfoil shape by three variables: maximum camber m, chordwise position of maximum camber p and maximum thickness t. Such approach is the most known within aviation industry due to its simplicity and experimental data available.

CST coefficients, PARSEC and Improved Geometrical Parameterisation (IGP) are parametrizations methods that require a high number of design variables since they define the airfoil shape through linear combination of base functions. The main benefit of such methods is that they provide more flexible geometries than the NACA series, the concern, however, is to determine to what extent do we require a flexible shape parametrization.

The goal is to define which method finds the best possible compromise between a low number of design variables while being flexible enough to allow shape control in the regions of interest. An alternative way diverging from all the proposed by the current available literature is suggested as follows. The shape of the flap has a relevant effect on the overall performance, but a simple NACA 4 digit nomenclature is deemed as flexible enough to define it. For the main element, however, a higher level of flexibility is favourable since the airfoil performance is considerably sensitive to the slot shape, which is affected by the main airfoil's geometry at the trailing edge. Therefore, the NACA method can

be mixed with a parameterized modification along the trailing edge. In such way, the number of shape-related design variables of the main element is kept relatively low and the allowed design flexibility is well adapted to the specific problem, where we want to find a suitable flap integration. Moreover, a very significant reason to select the NACA nomenclature for the flap and as a 'backbone' for the main element is that the thickness becomes very easy to control for both elements while it would not be straightforward with the other mentioned schemes (CST, PARSEC, ...). That is quite relevant since the thickness is a parameter that depends mainly on the structural requirements and thus, should be easily constrained in the optimization procedure.

Figure 4.1 shows the modification on the trailing edge of the main element (blue) to integrate the flap and allow the optimization algorithm to vary the slot shape. Such modification will be referred as the 'TE cut' or 'cut'. The cut is defined by a third order polynomial,

$$y = ax^3 + bx^2 + cx + d. \tag{4.1}$$

Such equation has initially 4 unknowns (a, b, c and d), where one is computed through a 'mandatory' geometrical constraint, that is, smooth transition at the lower surface, i.e. the derivative of the curve must be the same on both sides of the cut. Two other unknowns are constraint by two design variables: the starting location along the lower surface of the main element x_{c1} and the ending location along the upper surface of the main element x_{c2}. Lastly, the remaining unknown, a is left as a design variable itself determining the curvature of the cut, therefore $a = \kappa^m$.

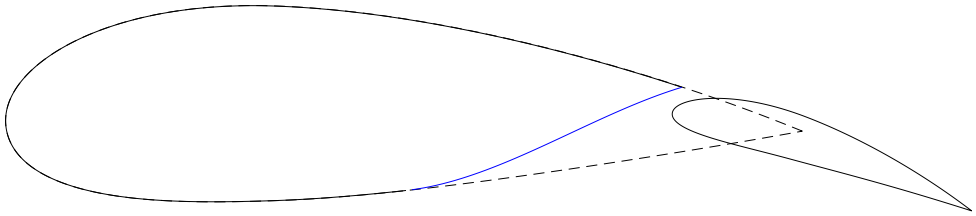

Figure 4.1: Cut on the trailing edge of the main element (blue).

Such approach of cutting the main element to integrate the rear element was already employed by Makani [27] as shown in Figure 4.2. In such case the main element was not scaled, only cut, while for the current work the main element is both scaled down and cut. The scaling down of the main element is depicted in Figure 4.1 where the dashed line shows that the original main element chord has been reduced. The main element scaling factor is inferred from other design variables: flap overlap and chord, introduced later in this section.

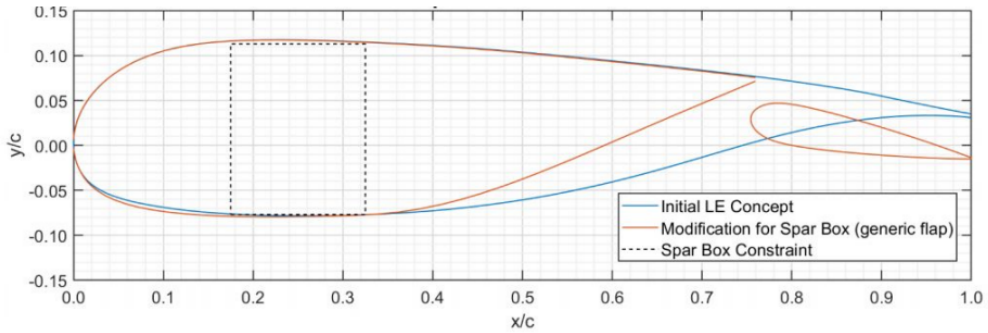

Figure 4.2: Makani's cut on main element, [27].

To visualize the effect of the design variable 'TE cut curvature, κ^m, Figure 4.3 shows different values of curvature κ^m. The curvature in addition to the design variables that determine the initial and

ending location of the TE cut allow for a very adaptable main element TE, therefore providing a wide scope of geometries to integrate the flap.

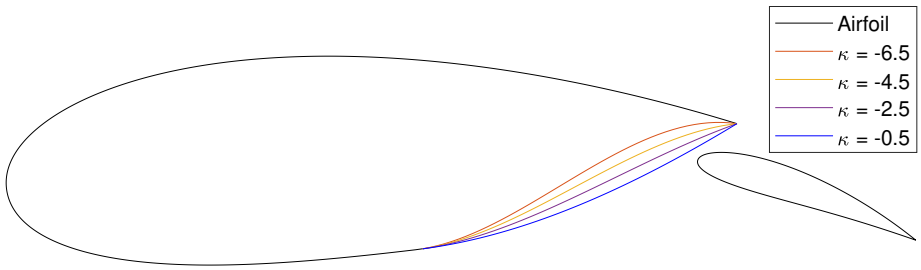

Figure 4.3: Effect of the design variable: cut curvature κ^m.

Regarding the setting design variables, the relative position between the elements is defined through four variables: flap overlap, flap gap, flap chord and flap deflection. The gap is defined as the vertical distance from the main element's TE to the flap while the overlap refers to the distance in the chordwise direction, see Figure 4.4.

The employed parametrization results in a total of **12 design variables**, listed below and geometrically illustrated in Figures 4.4 and 4.5:

Main element shape	Flap shape	Setting/relative position
Camber, m^m	Flap camber, m^f	Flap gap
Position max. camber, p^m	Position max. camber, p^f	Overlap
Cut starting position, x_{c1}	Flap thickness, t^f	Flap deflection, δ_f
Cut ending position, x_{c2}		Flap chord, c_f
Cut curvature, κ^m		

Table 4.1: List of shape and setting design variables.

Note that the main element thickness is not a design variable since it is given as a constraint by the industrial partner of the present thesis. Such constraint comes from the wing structural design since the thickness of the airfoil will determine the thickness of the wing main spar.

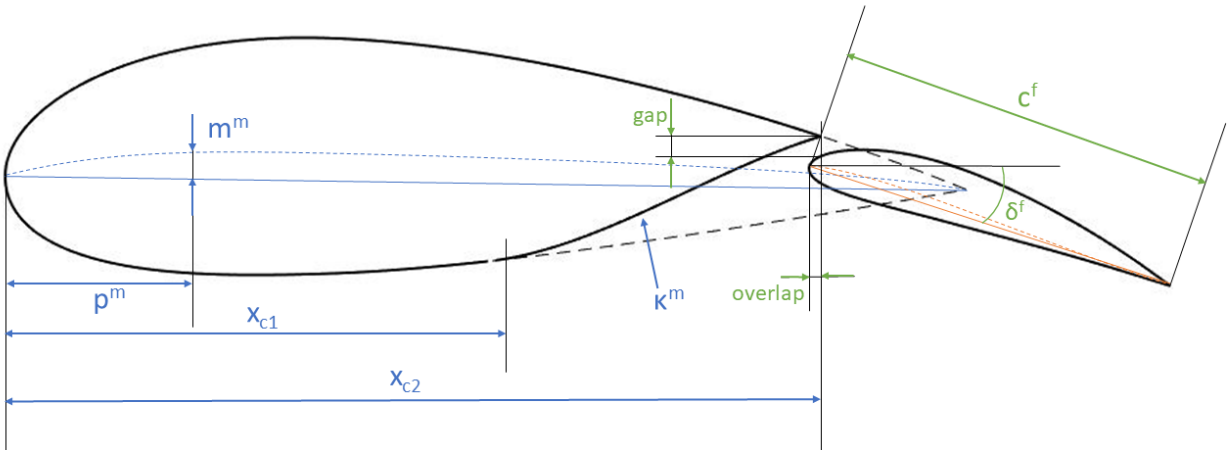

Figure 4.4: Design variables that define the main element shape (blue) and the setting (green).

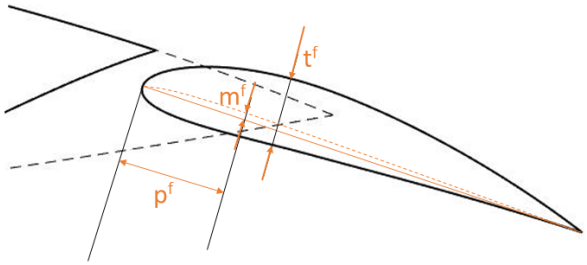

Figure 4.5: Design variables that define the flap shape.

4.2. Optimization strategy

4.2.1. Objective functions

An objective function or fitness function is the function to be minimized (or maximized) by the optimization algorithm. It is therefore a function of the design variables vector **x**, a 12-dimensional vector where each component is a design variable. As described in Section 2.1.4, the optimization algorithm employed is a multi-objective genetic algorithm, hence able to deal with various objectives. The selection of objective functions is crucial for a successful optimization since the algorithm will be only lead by the objectives it is given.

Being able to select multiple objectives is paramount due to the complexity in designing an AWE kite system. The algorithm is employed to optimize the airfoil for the production phase while the return phase requirements are accounted for in the resulting airfoil. For the production phase there are several objectives to be accounted for. In order to maximize the available power it is desired to have a design C_L as high as possible, where the design C_L (C_{Ldes}) is defined as the highest C_L at which the airfoil will operate. On the other hand, the maximum C_L (C_{Lmax}) is the highest C_L that the airfoil can physically reach, before stalling. Therefore, there must be a certain margin between the C_{Ldes} and C_{Lmax}. The industrial partner of the thesis recommends to have a margin such that $C_{Lmax}/C_{Ldes} = 1.25$, thus, the C_{Ldes} is given by C_{Ldes} = C_{Lmax}/1.25. In order to maximize the C_L at which the airfoil will operate, the C_{Lmax} must be maximized, that is the first objective function.

Furthermore, the power coefficient, given by the expression C_L^3/C_D^2 is also to be maximized. Such coefficient, introduced by Loyd [46], was found to be proportional to the power given by a kite flying crosswind. Therefore, such parameter must be accounted for designing the airfoil. Figure 4.6 shows a power curve of an AWE system and the typically employed lift coefficient at each operational state. Two main operational states are distinguished, power production below the rated wind speed and above rated wind speed. The rated wind speed is the wind speed at which the rated power is achieved, where the rated power is the maximum power for which the system has been designed.

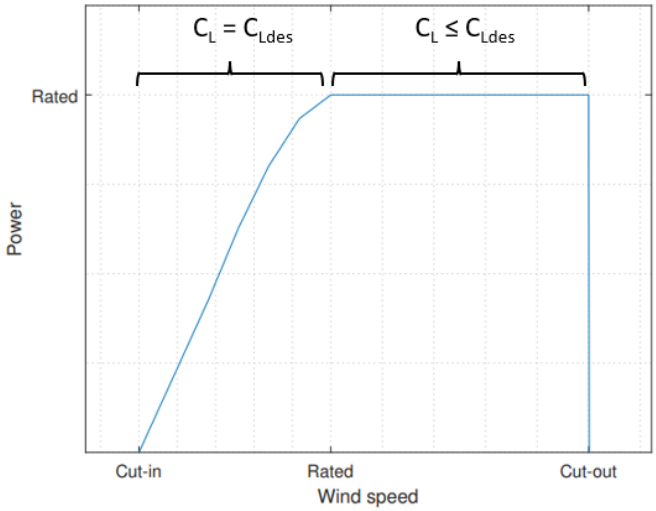

Figure 4.6: Power curve with typically employed C_L.

As seen in Figure 4.6, the system typically operates at C_{Ldes} below the rated wind speed and at a lower C_L at the rated power (above rated wind speed). The reason to decrease the C_L above rated wind speed is to cap the power and keep it on the rated power, if the C_{Ldes} was employed above the rated wind speed, the power would keep increasing (assuming a reel-out strategy or other control strategies are not employed). It is therefore inferred that the power coefficient should not only be maximized at the design C_L, but at a lower C_L as well. Such lower C_L must be representative of the C_L range typically employed at rated power. In addition, note that C_L's lower than the C_{Ldes} can also be employed in case the tether force is to be reduced or to reduce the power peak. The objective functions must therefore take into account the power coefficient at both C_{Ldes} and a lower C_L. As previously mentioned, the design C_L is taken as C_{Ldes}= C_{Lmax}/ 1.25, the lower C_L is given by C_{L2}= $C_{Ldes} \cdot 0.7$, which is considered to be representative of the whole rated power operation.

In order to avoid operating with very high values, the square root of the power coefficient is optimized instead of the power coefficient itself. Moreover, the Matlab function that executes the genetic algorithm, *gamultiobj* is developed to minimize the objective function instead of maximizing it, so the objectives to be maximized are minimized with the inverse sign. These remarks lead to the following objective function vector, f_{obj} where each component is one objective:

$$
\begin{aligned}
f_{obj}(1) &= -C_{Lmax} \\
f_{obj}(2) &= -C_L^{1.5}/C_D @ C_{Ldes} \\
f_{obj}(3) &= -C_L^{1.5}/C_D @ C_{L2}
\end{aligned}
$$

The multiple objective functions are treated with the pareto front in the current work. The pareto front is the set of airfoils that can not improve one objective function without having a detrimental effect on another objective function. Therefore, such airfoils find a compromise between the various objectives of the optimization. A more traditional manner of dealing with multiple objectives is by converting them into one single objective consisting of a linear combination of the multiple objectives. Said approach allows to give certain weights, therefore relevance, to each particular objective, however, it constrains the user to that selected distribution of weights. The pareto front is preferred since it allows us to see what kind of compromise among the objective variables are feasible and select the airfoil that provides the most advantageous balance, thus adding flexibility to the design procedure, as concluded in [64]. Due to the population-based nature of a GA, it is well suited to find the pareto front, which is one of the features that made us opt for such algorithm.

To visualize the pareto front, a simplified optimization with two objective functions has been run,

providing a pareto set that can be shown in a 2D plot. Figure 4.7 shows the pareto front in black and the rest of the airfoils population is depicted in light grey.

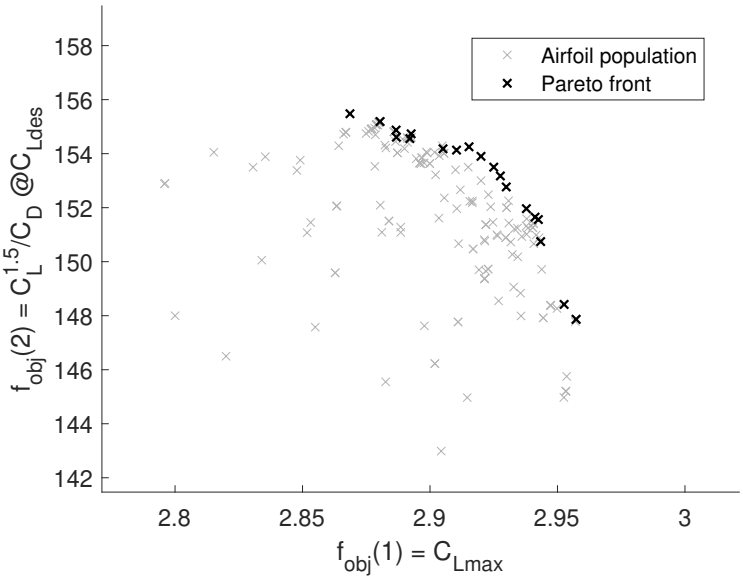

Figure 4.7: Pareto front for a simplified optimization run.

The pareto front is shown as a group of discrete points (or airfoils), while in reality the pareto front should be a continuous curve since the design variables that define the airfoil geometry are continuous variables. The discrete points forming the pareto front are a consequence of the numerical approach to the problem, however, a somewhat continuous smooth curve could be drawn from the discrete points.

The three presented objective functions give no relevance to the airfoil performance above the design C_L which is indeed not critical to the design since such C_L's are not to be employed in any operational phase. However, it is beneficial to have a smooth progressive stall behaviour, i.e. avoid a sudden drop of lift. Such objective is not included in the algorithm but the stall behaviour will be manually supervised on the resulting airfoil. Similarly, the pitch moment coefficient is not included in the objective functions given to the algorithm but its value will be manually checked such that is does not reach an excessively high value. The consequence of a drastically high pitching moment would be that a bigger horizontal tail would be required to counter-balance the pitching moment from the wing.

4.2.2. Flow conditions

The optimization is run under certain flow conditions that must be representative of the conditions seen by the kite during operation. The relevant flow conditions to be determined are the Reynolds number and the boundary layer type (laminar or turbulent). The Reynolds number is the non-dimensional number that gives the ratio of inertial forces to viscous forces and it is computed as follows,

$$Re = \frac{v\rho l}{\mu} \tag{4.2}$$

where v is the flow speed, ρ is the fluid density, l is a characteristic length (in our case the airfoil chord), and μ is the dynamic viscosity of the fluid. A representative flow speed for the kite system operation is given by the industrial partner to be a reference speed of v_{ref}=45 m/s. It is evident that the kite will operate at a wide range of speeds but a reference value must be chosen for this design phase. The density and dynamic viscosity are taken at a reference temperature of 15º, therefore leading to the values ρ= 1.225 kg/m^3 and μ= $1.81 \cdot 10^{-5}$ kg/(ms). The reference length is also provided

by the industrial partner, a reference chord must be employed such that is representative of the whole wing. Since the wing will have a varying chord in the spanwise direction, an estimation of the mean aerodynamic chord (MAC) is employed, which is assumed to be close to $l = 1$m length. Substituting in the Reynolds number equation, we reach

$$Re \approx 3 \cdot 10^6 \tag{4.3}$$

which will be employed for the whole optimization procedure.

From the industrial partner experience, it is known that the leading edge of the kite wing will get dirty as soon as it has been operative for a certain amount of time and it will remain dirty through a significant time of operation. Such impurities on the wing's LE trigger the turbulent flow in the boundary layer. Consequently, a fully turbulent BL has been employed for the airfoil optimization, even though it might be partially laminar for some operational time while the LE remains clean. Such approach is deemed as conservative since a turbulent BL is known to increase the viscous drag on the airfoil's surface [5].

4.2.3. Convergence of the optimization algorithm

The current subsection presents how the algorithm determines that the optima has been reached. To do so, the criteria for convergence and the progress of the genetic algorithm towards the optima is shown for an optimization run with two design variables and one objective function. Said amount of variables is chosen such that the design space is 2D and can be easily plot through contour lines. The chosen design variables are related to the setting: flap gap and overlap, while the objective function is C_{Lmax}. Therefore, for the current example, we are trying to determine the combination of flap gap and overlap that leads to a maximum C_{Lmax}. Such problem would not require an optimization algorithm since it is simple enough to run all the combinations of flap gap and overlap with a certain step and determine where the maximum is found. However, it is useful to do so to check that the genetic algorithm is indeed reaching the optima and check the convergence criteria.

The design space given by the flap gap and overlap is shown in Figure 4.8, where the optimum gap size is observed to be around a 2-3% of the whole chord and the overlap close to 0, thus the TE of the main element and the LE of the flap coinciding in the same horizontal position.

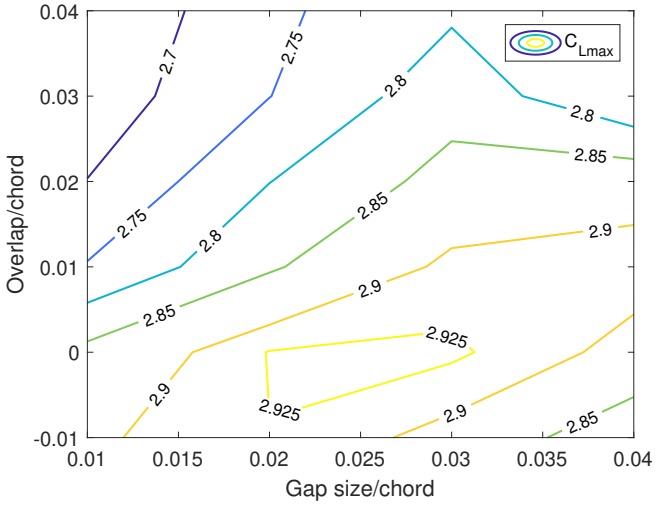

Figure 4.8: Contour plot depicting the design space for the flap gap and overlap.

By running the GA for this simplified example, we can see how the airfoil populations converge towards the optimum region, as depicted in Figure 4.9.

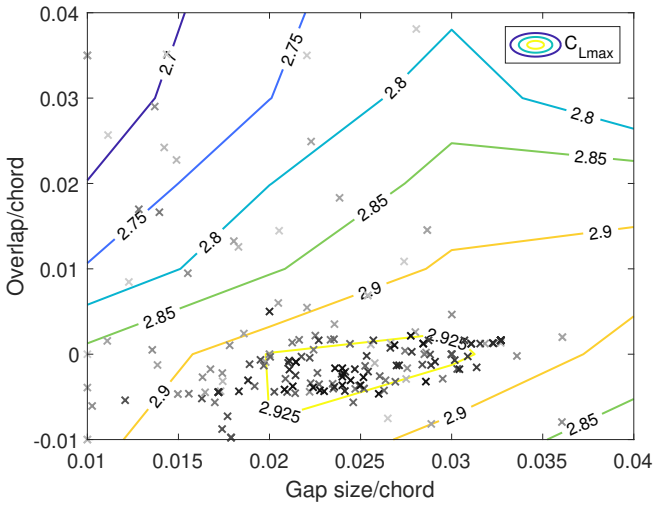

Figure 4.9: Contour plot depicting the design space for the flap gap and overlap with the airfoil populations computed by the GA.

Each black cross in Figure 4.9 is an airfoil and in order to show the progress of the populations the transparency of the cross has been employed. A darker cross is an airfoil of a later (thus better) population than a lighter cross, therefore, it is seen that the airfoils get closer to the optima as new generations are computed. The airfoils do not converge to an exact point, they are rather sparsely concentrated in the optimal region. That occurs since the maximum seems to be found in a region with a rather low gradient.

The convergence criteria to determine that the algorithm has reached the optima is based on the average of the relative variation of the maximum objective function for each population. For the case depicted in Figure 4.9, 11 populations have been computed, where the average, maximum and minimum C_{Lmax} of each population is shown in Figure 4.10.

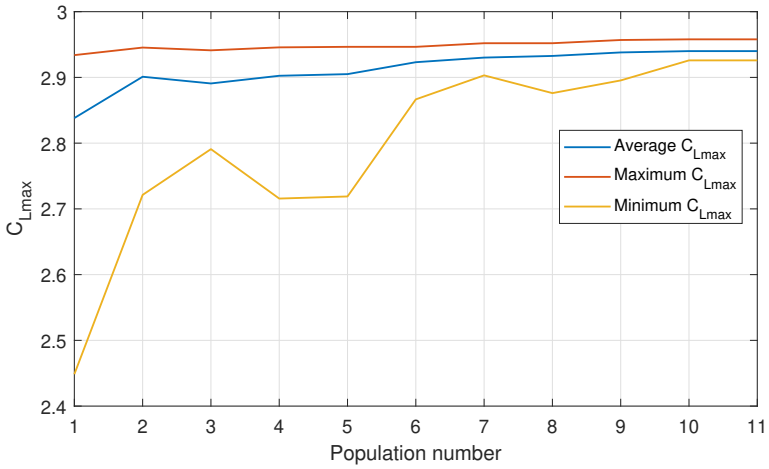

Figure 4.10: Average, maximum and minimum objective function for each population.

It is clearly seen that the average of C_{Lmax} increases with the number of populations and it converges to a constant value after a few populations. If more populations were computed, the average would get closer to the maximum, however it is not necessary since the maximum is considered to be found once the convergence criteria is fulfilled. The algorithm stops when the average of the relative variation of the maximum objective function among n_p populations is less than a certain tolerance. Both the tolerance and n_p are given to the algorithm as inputs, for the current work, the tolerance is

set to $1 \cdot 10^{-3}$ and n_p=3. It is also observed that the maximum C_{Lmax} of the first population has already reached a value close to the optimum, that occurs since the randomly spread first population has an airfoil close the optimum region. That is less likely to occur as the design space has 12 dimensions as will be the case for the full optimization problem.

Even though the mentioned convergence criteria was used to stop the algorithm, for some cases the algorithm was stopped manually before it reached the criteria due to long computational time. After a certain number of generations had been generated, if all individuals start to converge towards a promising individual the genetic algorithm was stopped.

4.2.4. Addition of design variables to the optimization algorithm

As specified in Section 4.1, the total amount of design variables employed in the optimization algorithm is 12. Both for learning purposes and ease of implementation, the 12 design variables have been added progressively, thus showing the effect of adding design variables into the algorithm. The algorithm is expected to reach a 'better' airfoil the more design variables it is given, since it will be able to try a wider range of airfoil geometries. Since 'better' is somewhat vague, let us clarify that technically it means 'with a higher fitness/objective function' (or lower if the aim is to minimize).

Such effect can be clearly observed by running the optimization algorithm several times while adding design variables. The objective functions have been presented in Section 4.2.1, however, for clearer visualization, two objective functions (which can be shown in 2D plots) have been employed for this exercise. The two objective functions are maximum lift coefficient, C_{Lmax}, and power coefficient at the design C_L. For each optimization run the pareto front is plotted, shown in Figure 4.11.

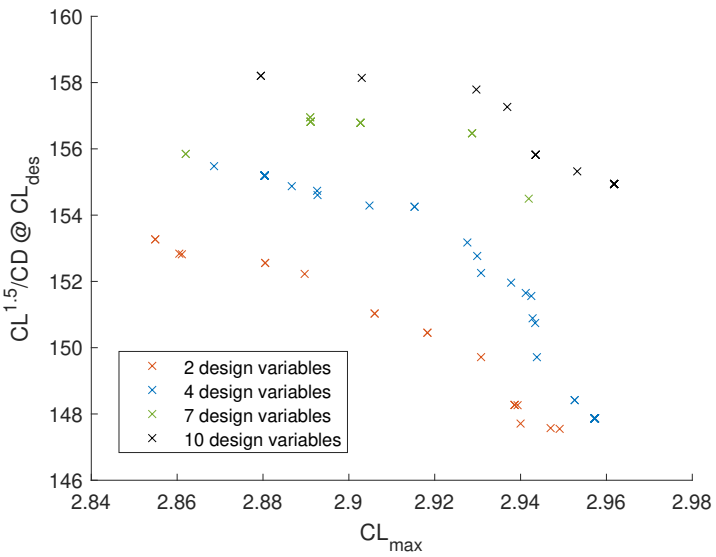

Figure 4.11: Pareto front for optimization runs with added design variables.

Each point in the shown plot is an airfoil resulting of the optimization process where the color depicts the number of design variables employed. Therefore, each set of points with the same color is a pareto set. It is shown that as the algorithm can generate more flexible geometries, i.e. it uses more design variables, it reaches higher values of both C_{Lmax} and $C_L^{1.5}/C_D$ @C_{Ldes} leading to a pareto front advancing towards better results.

The design variables employed for each run are:

2 design variables	4 design variables	7 design variables	10 design variables
Flap gap Flap overlap	previous 2 + Main element camber Main element max. camber position	previous 4 + Flap camber Flap max. camber position Flap thickness	previous 7 + Cut starting position Cut ending position Cut curvature

Table 4.2: Progressive addition of design variables into the algorithm.

For each optimization run, all the design variables are recombined meaning that the design variables that are present in various optimization runs can vary. For instance, let's consider the flap gap which is present in all the runs, the optimal flap gap can vary as design variables are added into the algorithm since the optimal flap gap might be dependant on the shape of the elements. It has been proved that there are indeed coupling effects between the various design variables since the ones that are present in multiple runs do vary slightly as design variables are added.

The variation of the airfoil geometry as design variables are added is shown in Figure 4.12. Notice that for each optimization run, various airfoils can be selected, each having a slightly different compromise between the two objective functions. The airfoils shown in Figure 4.12 are the ones that give a similar weight to both objectives. Moreover, they are selected such that both objective functions are improved when going to an optimization run with a higher number of design variables. In other words, we are moving to the top right corner in Figure 4.11.

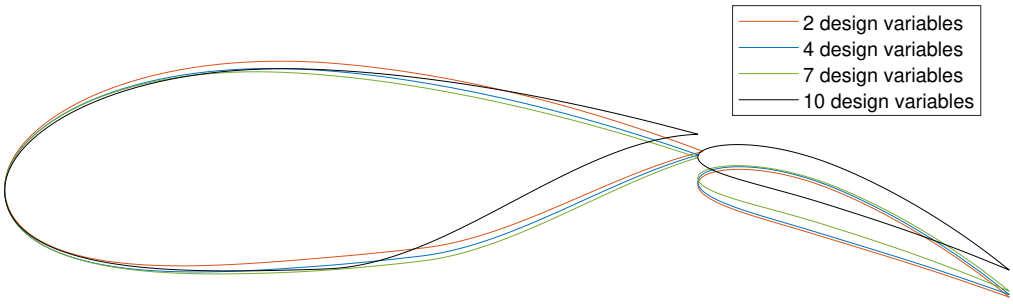

Figure 4.12: Variation of multi-element airfoil geometry as design variables are added into the algorithm.

The main element varies significantly as the design variables related to the cut are added (from 7 to 10 variables). Although such cut shows a better performance in terms of the two considered objective functions (C_{Lmax} and $C_L^{1.5}/C_D$ at C_{Ldes}) it is discarded for the main optimization process due to poor performance (i.e. high drag coefficient) at C_L's lower than C_{Ldes}. That is precisely why a third objective function has been employed for the whole optimization procedure, consisting of the power coefficient at a lower C_L than the C_{Ldes}, as described in Section 4.2.1. Therefore, this study made evident the relevance of selecting properly that objective functions that are fed into the algorithm since they can lead to a poor result if selected inadequately, even though the algorithm works properly.

In order to show the poorer performance of the airfoil resulting of employing 10 design variables Figures 4.13a and 4.13b are presented. They show that both objective functions are indeed improved when adding design variables, but the power coefficient of the 10 design variables case has a poor performance below the design C_L, i.e. around C_{Ldes}=2.3 (recall that the design C_L is defined as C_{Ldes}= C_{Lmax}/ 1.25).

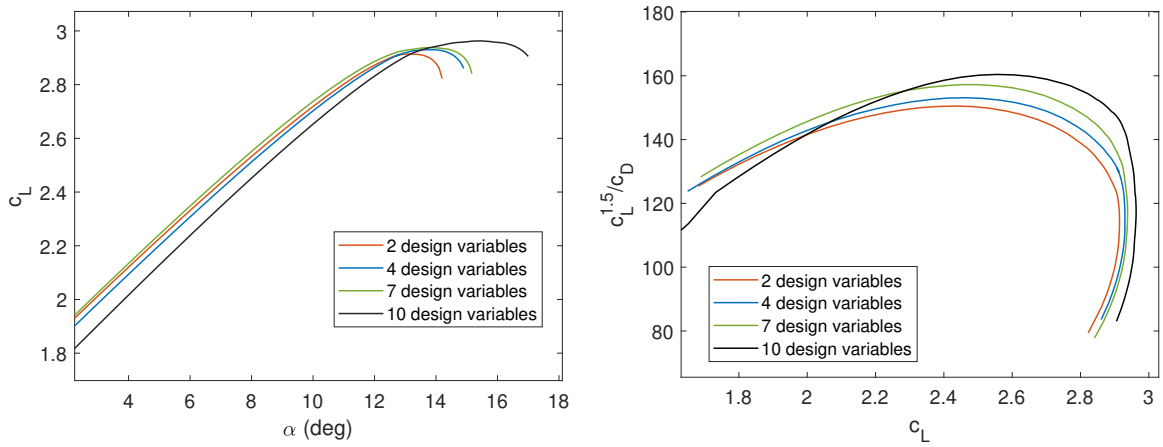

(a) C_L-α polars.

(b) Power coefficient polars.

Figure 4.13: C_L-α and power coefficient polars for optimization runs with added design variables.

4.3. Solver: MSES

The solver employed in the optimization procedure is MSES, a tool for two-dimensional aerodynamic analysis and design. It has been developed by Mark Drela and Harold Youngren at MIT [19] and it is available under a commercial licence and as open source program for research/academic purposes. The tool is built for the design and analysis of multi-element airfoils, but can also be employed for single-element wing sections. MSES is a coupled inviscid-viscous code, the inviscid formulation consists on solving the Euler equations, i.e. the Navier-Stokes equations without the viscous terms. On the other hand, the viscous flow is solved for the boundary layers using the two-dimensional integral boundary layer equations, [53]. In contrast to other inviscid-viscous codes, MSES does not iterate between the inviscid and viscous solutions, instead it couples both set of equations into a single nonlinear system of equations that is then solved by the Newton-Raphson iterative method, [29].

The Euler equations are solved using a finite volume method, where the grid is constructed automatically by intersecting the inviscid flow streamlines and splines emitting from the airfoil surface, as shown in Figures 4.14 and 4.15. The inviscid flow streamlines are precomputed with a panel method. The inviscid grid is coupled with the boundary layer equations through the displacement of the streamline closest to the surface with the displacement thickness δ^*.

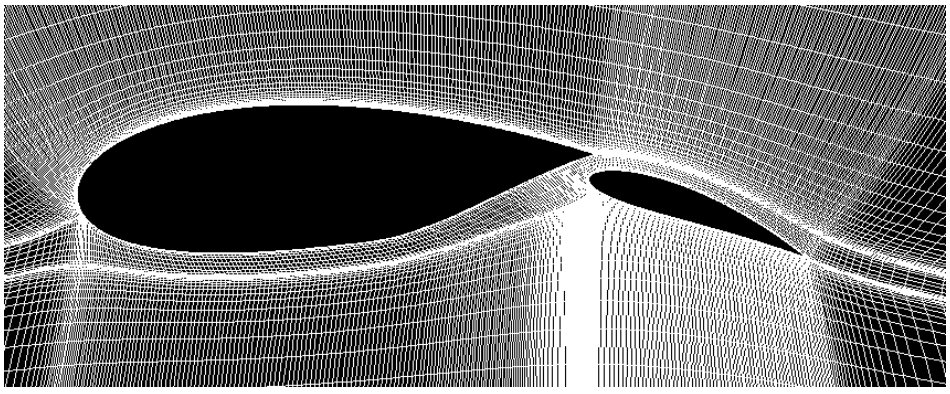

Figure 4.14: Mesh generated by MSES.

MSES has been selected as the solver to optimize the two-element airfoil due to the following reasons:

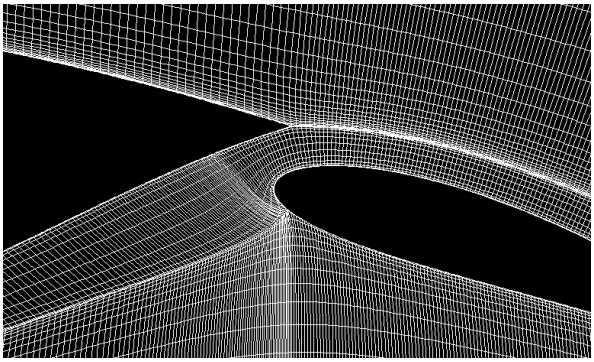

Figure 4.15: Mesh generated by MSES, zoom into the gap region.

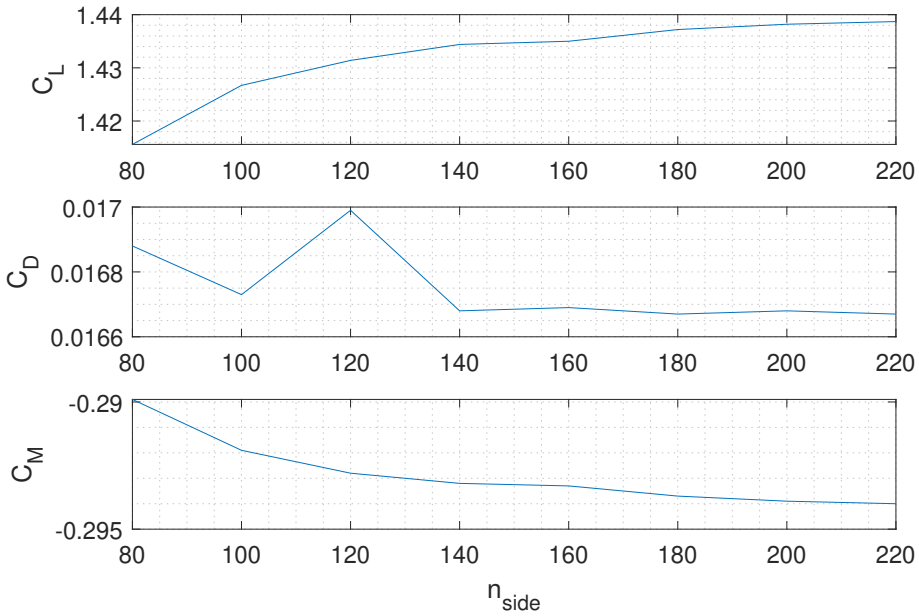

Figure 4.16: MSES mesh sensitivity.

- Automatically generated mesh with a very satisfactory quality and adaptable to variations of the geometry.
- Very short computational time.
- It is run from the terminal which allows to automate it with scripts, significant advantage to couple it with the genetic algorithm in Matlab.
- Available as open-source software for academic purposes.
- Fairly accurate results in terms of the linear C_L and C_{Lmax} although larger errors might be found for the C_D according to literature (further developed below).

According to literature [29], MSES captures rather accurately the $C_L - \alpha$ curve when comparing it to experimental data although it is slightly overpredicted in the linear region, [31] and [24] also report good agreement, the latter shows good correlation for C_{Lmax} as well. Regarding drag, it is generally underpredicted as reported in [29, 35] and [52]. MSES is deemed as a very suitable tool to optimize the airfoil due to the previously mentioned advantages but the optimization result will be verified with a higher fidelity solver: CFD-RANS simulation. The option of employing a RANS solver for the optimization itself is discarded due to the computational cost and its demanding meshing time. A genetic optimization loop coupled with a CFD solver was employed by [37] and its computational time was in the order of days.

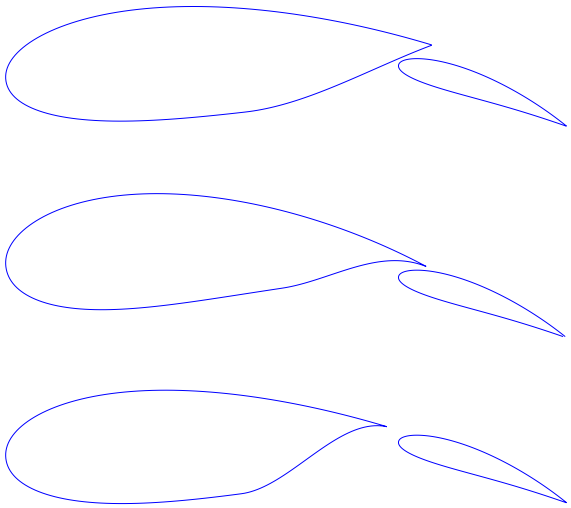

Figure 4.17: Multi-element airfoil that did not reach convergence when analysed with MSES.

As mentioned above, the mesh employed by MSES is constructed from the inviscid streamlines and points on the airfoil surface. The number of streamlines and airfoil points to be used for grid generation are determined by the user, as well as the outer boundaries of the grid. In the current work the mesh density has been determined according to test runs, where it was observed that the aerodynamic coefficients are rather insensitive to mesh density above a certain threshold. Figure 4.16 shows the sensitivity wrt to the number of points on the surface of each element side (n_{side}). Around 180 points per side have been used. The size of the mesh was determined according to the recommended in the MSES documentation [21], which shows low sensitivity to the absolute mesh size.

The main drawback found when using MSES is that some cases (combination of the geometry and analysis setting) do not reach convergence. Such phenomena mainly occurs due to an unfeasible geometry or due to the flow conditions of the analysis, or a combination of both since they are closely related. Unconverged cases due the flow conditions of the analysis are mainly related to the angle of attack being either high or low such that big regions of separated flow and recirculation take place, these cases are not considered a very significant issue since they usually occur after stall, therefore, after C_{Lmax} has been captured. The main issue related to this unconverged cases is that divergence might occur when running an α sweep before C_{Lmax} is reached if the step in AoA is too big. To solve that, an adaptive AoA step has been implemented, further explained in the following section 4.4: Computational framework. On the other side of the polar, for low AoA, MSES stops converging as soon as the detached flow region is too big, however, that is not considered an issue either since the minimum converged C_L can be used to infer the minimum C_L before the non-linearities occur in the C_L-α curve.

The other factor that leads to unconverged cases is the geometry of the multi-element airfoil, these cases were more challenging to deal with. Figure 4.17 shows three examples of multi-element airfoils that did not converge. The reason why these type geometries do no reach convergence is not always known but it has been observed that elements too close to each other hinders convergence as well as very pronounced curvatures. Such curvatures can lead to a steep deceleration of the flow to the point that flow separation occurs even at relatively low AoA's. The other main reason is that the mesh does not adapt properly to the geometry, and thus, it requires that the mesh is constructed manually for that geometry.

When running one single case where the analysis is not converging due to an unfeasible geometry, one can investigate the mesh and manually alter it to adapt it to that specific geometry. By doing so,

chances of convergence increase considerably as has been proved for the current work. However, we aim to couple the MSES analysis to a genetic algorithm that will generate and analyse a wide range of geometries automatically, thus it is not feasible to manually adapt the mesh for each case where convergence is not reached.

It would be highly desirable to have a robust model where every combination of design variables within the desired design space leads to a solution for the objective functions. Such complete robustness was not reached but the issue was overcome through various implementations.

- Several test runs were done before running the algorithm trying a wide range of geometries, in order to find the mesh parameters that would create a suitable mesh for every or most geometries. These 'generic' mesh parameters allowed the algorithm to run for the majority of cases.
- The bounds for the design variables were also adjusted to avoid unfeasible geometries such as minimal gaps or extremely pronounced curvatures.
- All the details for each analysed individual, i.e. design variables and objective functions were stored in a file, that was required not only to analyse the progress of the GA run but also to resume an optimization run if an unconverged case stopped the algorithm. When that happened, that individual was analysed manually to try to obtain the objective function and the GA was resumed without losing the previous progress since the already computed populations can be fed to the algorithm as initial population.

The approach of manually analysing some particular cases or adjusting the bounds to avoid certain unfeasible geometries is an approach that involves the designer's critical thinking instead of leaving the whole optimization process to the computational algorithm itself. Such an engineering treatment is called '*human-in-the-loop*' and it is proved to be effective in accelerating the convergence and producing more engineering applicable solutions by [10]. Said author uses the *Human-in-the-loop* technique to monitor and control the GA, as well as introducing new individuals manually. This helps to improve the diversity of the population and raise the possibility of finding a new design peak. Due to its benefits, Human-in-the-loop was also employed for the current work when deemed as necessary.

4.4. Computational framework

The optimization was performed through the Matlab function, *gamultiobj* [**pareto_matlab**], which executes the multi-objective genetic algorithm to find the pareto front of the objective functions. The optimization algorithm requires a function that computes the objective function from the design variables, such function is called ***computefobj*** and once it has been developed it can be treated as a black box where the input is a vector containing the design variables defining the airfoil geometry, x and the output is a vector containing the objective functions to be minimized, f_{obj}.

In order to present how the function *computefobj* works let us first explain how the solver MSES is employed. MSES has various functionalities that are executed through different programs called from the terminal, the three MSES programs (extensively described in the MSES documentation [21]) employed by *computefobj* are:

- mset: the program that initializes the grid and the flowfield. In order to initialize the grid it requires the airfoil geometry which is read from a *blade.* file containing the coordinates of the multi-element airfoil and the grid size. mset also requires the grid parameters, read from the *gridpar.* file. The output of this program is an *mdat.* file containing the initialized flow solution.
- mses: the flow solver, it is the main program that solves the Euler equations and the BL integral equations. It requires two input files, *mdat.* and *mses.*, and then writes the output file back to *mdat.*. The *mses.* file contains the properties for the analysis, such as AoA/C_L or Reynolds number, location to trigger a turbulent BL, etc.
- mpolar: a version of mses which sweeps through a range of a specified parameter (AoA in our case), thus generating a polar curve. Since it takes full advantage of the quadratic convergence of the Newton method, using mpolar is more efficient than running a sequence of independent

cases from scratch with mses. In addition to the input files required by mses it also requires a *spec.* file, containing the sequence of parameters (AoA). The output of mpolar is a file *polar.* containing the whole computed polar.

There are other functionalities that have been used outside the function *computefobj* for post-process analysis, such as plotting the pressure coefficient distribution or visualizing the flow streamlines. Such functionalities have been done through the program mplot, which displays the solution stored in the *mdat.* file.

Figure 4.18 shows the three MSES programs and their input/output files in a schematic manner, assuming we are analysing an airfoil called *airfoil1*.

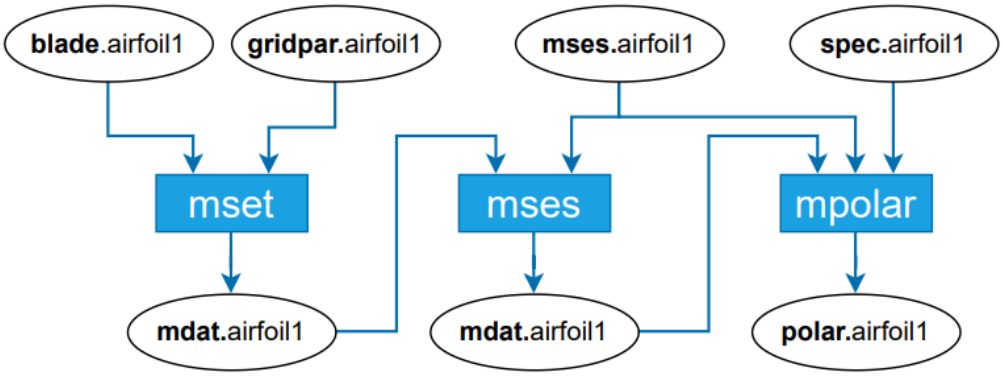

Figure 4.18: Scheme of the MSES programs with their required input files and output files.

The *computefobj* consists on various subfunctions that ultimately compute the objective functions, its implementation is shown in Figure 4.19.

The MSES programs employed are executed by calling them from the terminal, which is possible to do from a Matlab script through the command *system()*. Therefore, the function implemented in Matlab is coupled to MSES by controlling the terminal, creating files required by the programs and reading the output files.

In order to find the maximum lift coefficient, the subfunction **getfobj1** computes the stall region which can be somewhat problematic due to flow separation and thus, non-converged cases. Having non-converged cases is highly unfavourable since the optimization algorithm is then interrupted. In order to mitigate such cases, a very small step in angle of attack is used such that the flowfield solution does not vary drastically from one AoA case to the next one. However, employing a small angle of attack step leads to high computational time and many points in the polar that are not of interest. An adaptive step was then developed, the aim is to employ a somewhat high step of angle of attack within the linear region and a small step when the stall is taking place. Since each airfoil stalls at a different angle of attack, the variation of the step is computed with the C_L-α slope information. When the slope is below a certain threshold, thus approaching stall, the step in angle of attack is reduced. Such approach was proved to be very efficient in both reducing the unconverged cases without increasing the computational time. Figure 4.20 shows an example of a C_L-α polar with the adaptive step. The function computing the polar (*getfobj1*) automatically stops once the C_L starts decreasing since it means the C_{Lmax} has been found.

The function *computefobj* is then completed with the two other subfunctions: ***getfobj2*** and ***getfobj3*** that compute the two remaining objective functions. Since the C_{Lmax} has been computed by *getfobj1*, the C_{Ldes} and C_{L2} can be obtained, which are then used to compute the power coefficients. The *mpolar* program is mainly employed to get a full polar, however, the functions *getfobj2* and *getfobj3* also employ it to compute one single case since the dumped file (*polar.*) is well suited to be read

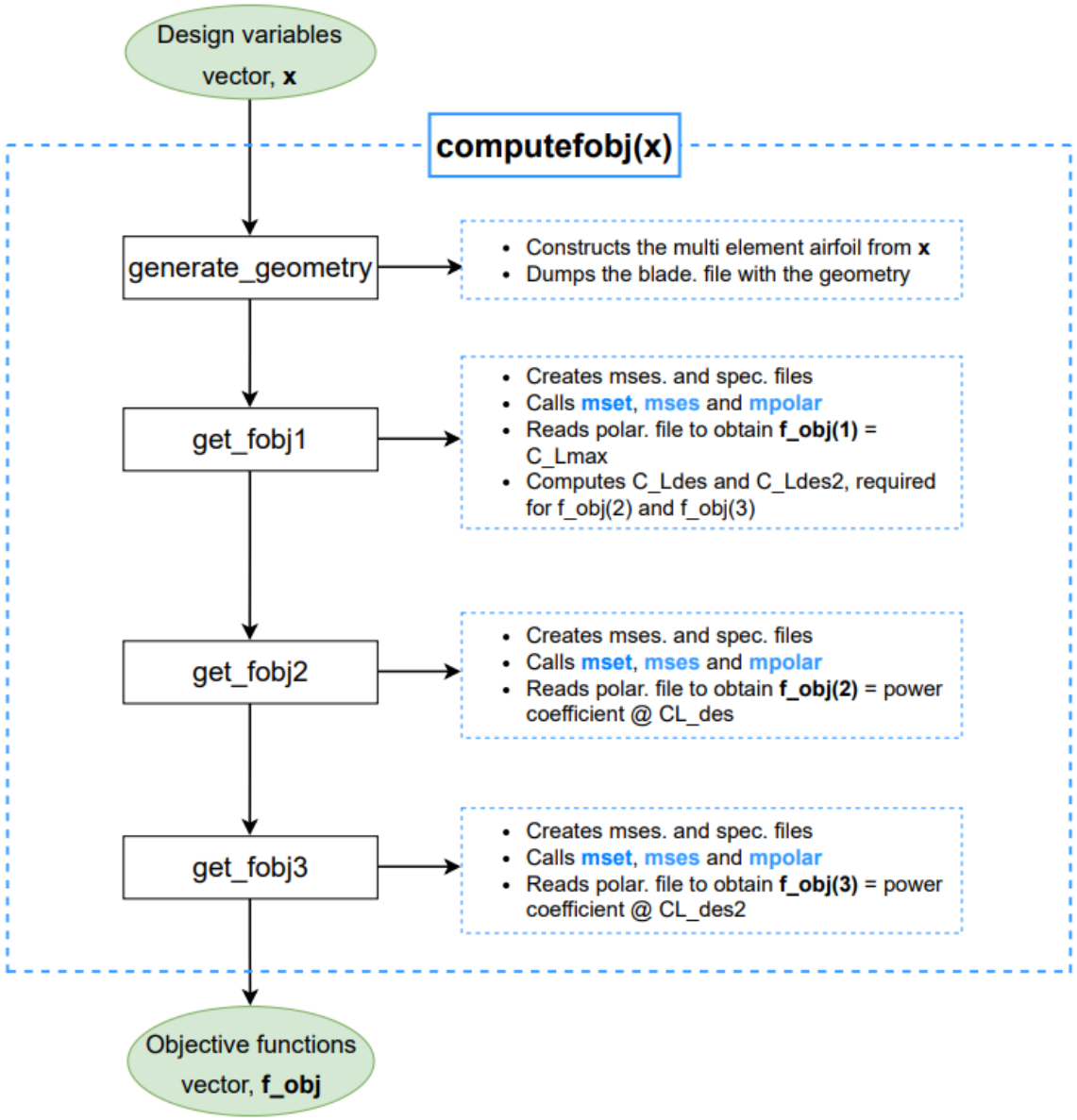

Figure 4.19: Flowchart of *computefobj*.

from the Matlab script.

Once the function *computefobj* has been developed, it can be fed to the genetic algorithm in Matlab. The genetic algorithm executed through the Matlab function *gamultiobj* requires the following inputs:

- The function *computefobj*
- An integer variable providing the number of design variables
- The upper and lower bounds for each design variable
- Linear constraints of the design variables (nonlinear constraints can also be given but they are not necessary for the current work)
- An optional variable that determines the following parameters of the genetic algorithm: population size, maximum number of generations, tolerance (convergence criteria), initial population and plots to display the algorithm progress while running

The overall Genetic algorithm structure is depicted in Figure 4.21 through a flowchart diagram.

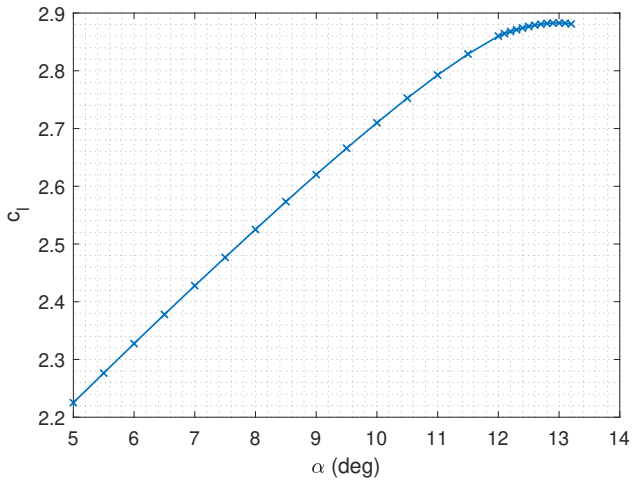

Figure 4.20: C_L-α polar with the adaptive step in angle of attack.

The termination criteria has been explained in the previous section 4.2.3 and the genetic operators have been introduced in the section about the GA, 2.1.4.

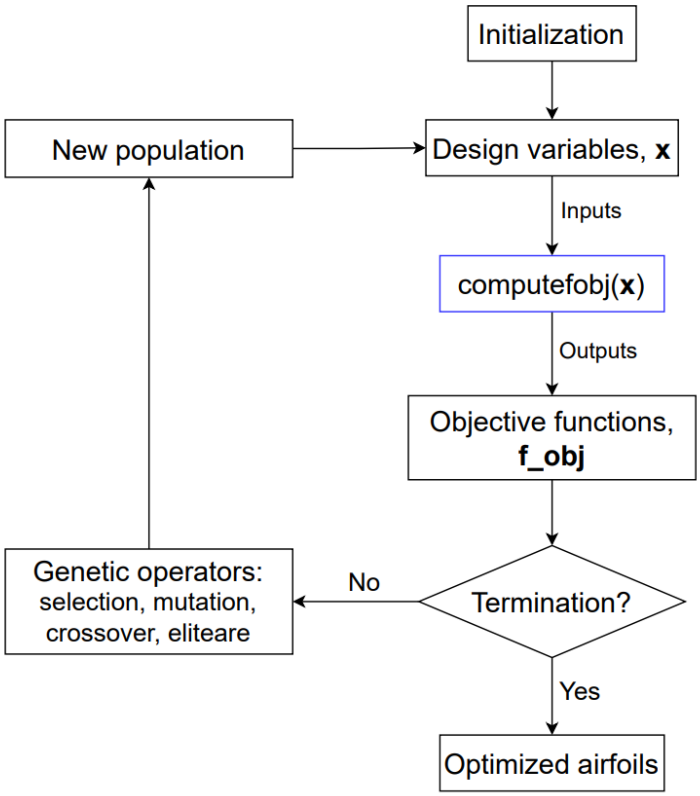

Figure 4.21: Genetic algorithm flowchart.

4.5. Optimization results

This section aims to present the results and observations of the optimization procedure with the three described objective functions and the 12 design variables. Since we have employed 3 objectives, the pareto front is a surface (or a set of points in a 3-dimensional space forming a surface) instead of the

curves shown in 4.2.4. Such set of points distributed in a 3D space is not well suited for visualization in a 2D graph, however, in order to show its results, certain airfoils from the pareto set are highlighted in the current section.

The main advantage of having the pareto front is that we can select which airfoil in the set finds the most appropriate compromise between the three objectives. Since three objectives have been fed into the optimization algorithm, there are three airfoils that maximize one single objective without concerning about the other two. It is interesting to compare these three airfoils geometries (Figure 4.22) and polars (Figure 4.23) to see how their shape and setting vary within the pareto set when prioritizing different objectives.

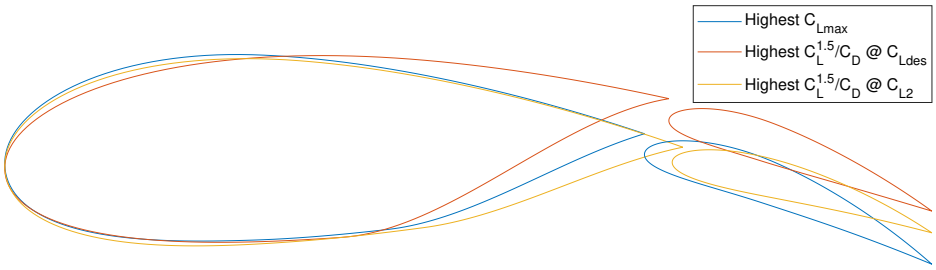

Figure 4.22: Airfoil geometries resulting of prioritizing different objectives.

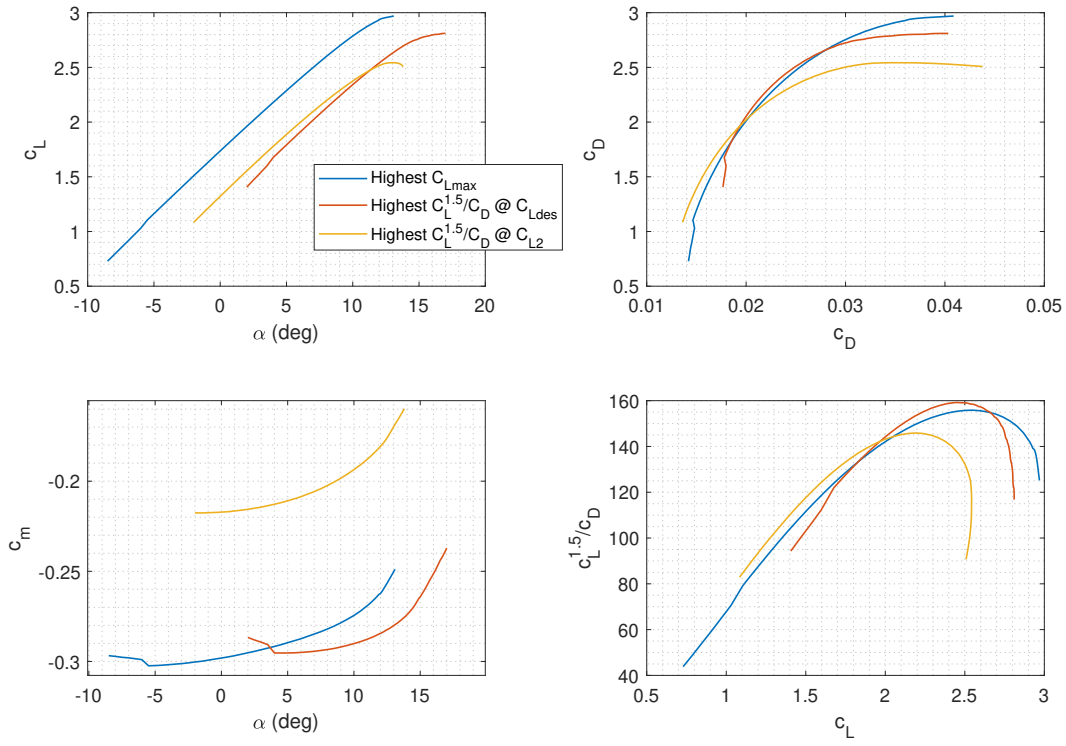

Figure 4.23: Polars of the three airfoils that prioritize different objectives.

Notice that these three airfoils reach the highest value for each objective within the bounds applied to the design variables, such bounds limit the design variables into the feasible design space. The polars in Figure 4.23 show that these airfoils indeed perform best in one of the objectives. In

Iannelli's [37] work, a multi-element airfoil is optimized through a genetic algorithm for commercial aviation purposes. One observation they presented is that the objective of the optimization algorithm is more sensitive to the setting variables rather than the shape variables. Such statement is not totally observed in the current work due to the main element does vary significantly at the trailing edge for the various objectives, although it is true that the flap shape does not vary much. It is then inferred that the unsensitivity of the objective functions with the shape parameters found by [37] might be subject to the type of parametrization scheme. Identifying the variables that have a greater effect on the objective is quite relevant since they can simplify further optimizations by putting more effort in the sensitive variables. [37] suggests to decouple the optimization problem into shape and setting parameters since it simplifies the optimization and such decoupling is justified by the objective functions being more sensitive to the setting variables. However, such approach is not recommended for the current work since coupling effects between the setting parameters and the main element's shape have been found, i.e. they are interdependant.

The C_L-α polar of the airfoil that maximizes the power coefficient at the design C_L (red in Figure 4.23) begins at a C_L of 1.4 approximately, which is relatively high. That is due to the fact that massive flow separation takes place even at slightly positive angles of attack at the pressure surface of the main element, leading to MSES not being able to converge below that angle of attack. Said airfoil is more prone to flow separation than the other two due to its drastic variation of curvature at the pressure surface, see Figure 4.22, making the flow decelerate excessively such that flow reversal takes place. Such phenomena will be further analysed in the section concerning return phase (Section 5.2.3), where low lift capabilities are required.

4.5.1. Selected airfoil

By analysing the obtained pareto front, an airfoil that finds a suitable compromise between the three objectives must be selected. The objective function of C_{Lmax} is given significant priority, therefore the selected airfoil is close to the one that maximizes only the C_{Lmax} However, such airfoil also reaches fairly high values for the other two objectives, the power coefficient. The reason why the C_{Lmax} has a great relevance in the decision is that it increases the operational C_{Ldes} which makes the kite able to produce energy at lower wind speeds, therefore reducing both the cut-in wind speed and the rated wind speed. Reducing the cut-in and rated wind speed is deemed as crucial in order to increase the operational wind range where the kite can operate as well as increase the energy yield for a given site. The geometry of the selected airfoil is shown in Figure 4.24 and its polars in Figure 4.25.

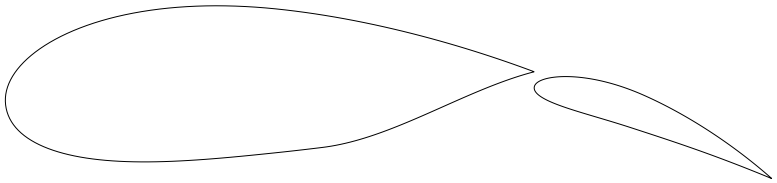

Figure 4.24: Selected airfoil for the production phase.

The polars show that the C_{Lmax} is close to 3, leading to a theoretical airfoil $C_{Ldes} = 2.36$ ($C_{Lmax} = 2.95$), giving an AoA margin between the C_{Ldes} and C_{Lmax} of about $\Delta\alpha$= 7.5º which is deemed as sufficient margin to ensure that the kite does not operate close to the C_{Lmax}. A reference we have to compare such value to other concepts is extracted from [27], where it is stated that Makani's constraint for the AoA margin was of 5º, thus reassuring that our resulting $\Delta\alpha$= 7.5º is satisfactory. Note that the airfoil C_{Ldes} is not the wing C_{Ldes}, due to the finite wing losses, nor the kite C_{Ldes} due to the tail and fuselage lift contribution. The power coefficient is maximum close to the design C_L meaning that the kite will operate efficiently when using the C_{Ldes}, i.e. below the rated wind speed. For high wind speeds, the power or tether loads might have to be capped by reducing the C_L, where the power coefficient will be inevitably lower. The pitching moment coefficient is around C_m=-0.31, which can

be balanced through the horizontal tail of the kite.

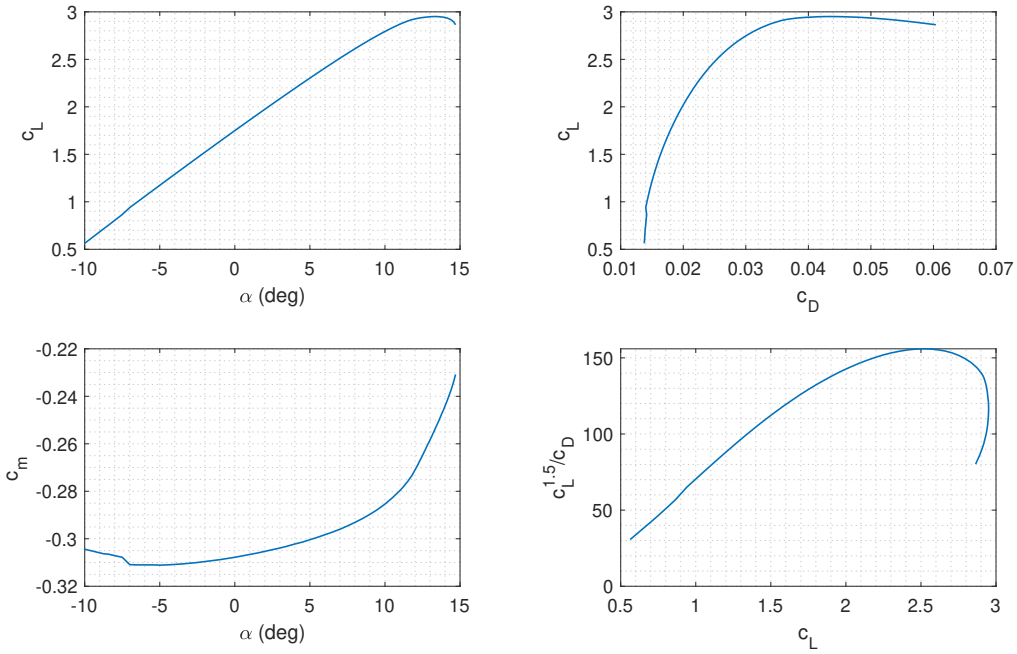

Figure 4.25: Polars of the selected airfoil for production phase.

4.5.2. Spanwise wing bending effect on optimized airfoil

The kite wing will show spanwise bending during operation due to the high loads, as a consequence of such bending the airfoil setting might well vary due to the relative movement of the two elements. The exact relative movement is not known since it would require a high fidelity structural analysis, however, for our work we assume that the wing bending will affect mainly the flap gap, i.e., the flap will move vertically with respect to the main element. Relative movement in the horizontal direction or rotational movement of the flap is also to be expected but it is deemed as less significant for a preliminary analysis. In the optimization process, the flap gap has only been constrained such that a minimal space is left between the main element and the gap, so that they do not end up overlapping the surfaces. However, no constraint has been added due to structural constraints such as wing bending. That was done in order to determine the optimal gap only from an aerodynamic point of view, and with that information the industrial partner can decide how to alter it, according to the expected bending such that the optimal aerodynamic gap will be present even with the wing bent.

A sensitivity analysis of the flap gap is then relevant to know how the performance of the selected airfoil will vary as the flap moves vertically with respect to the main element due to wing bending. The gap has been increased by 1% and 2% and the polars have been computed. For reference, the flap gap in the selected airfoil is 1.4% of the whole airfoil's chord. The airfoils with varying flap gap are shown in Figure 4.26 and their respective polars in 4.27.

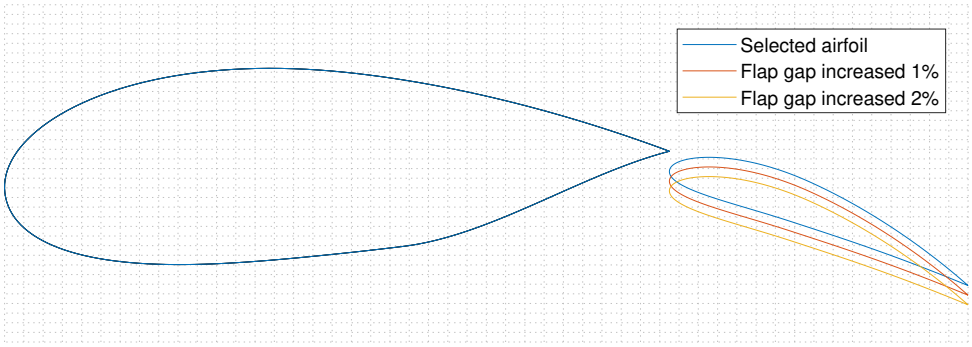

Figure 4.26: Airfoils geometry with flap gap variation.

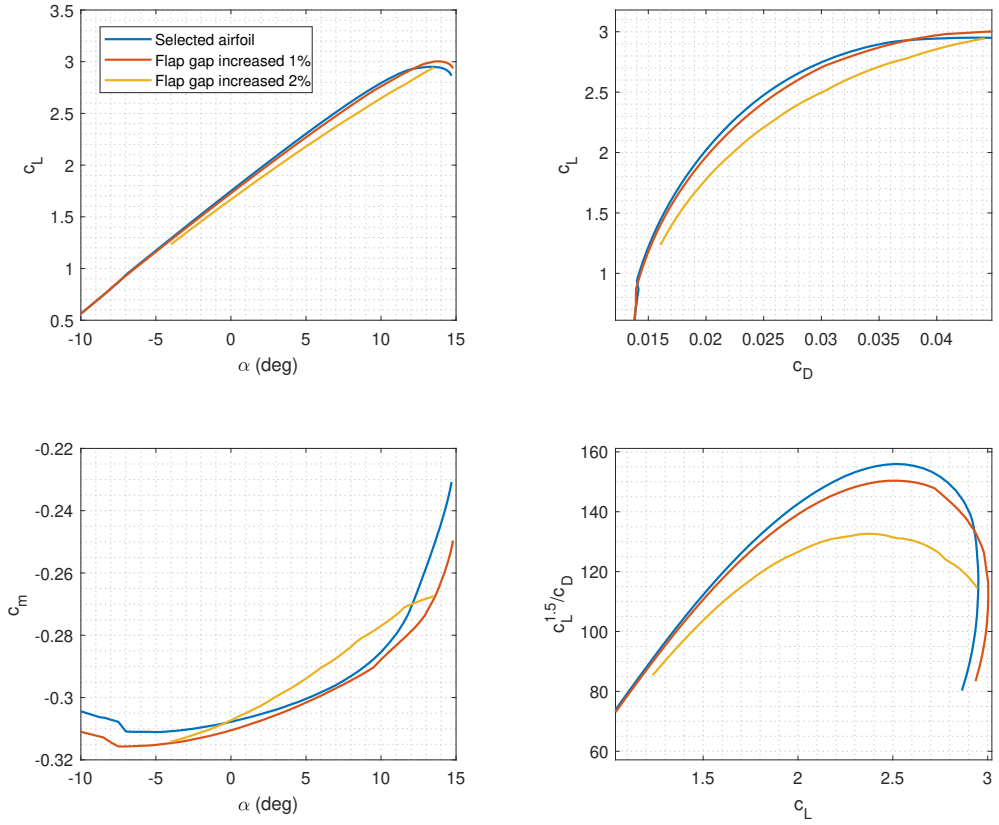

Figure 4.27: Polars for the airfoils with varying flap gap.

The polars show that the maximum C_L is not significantly affected by the flap gap increase. However, the drag coefficient does vary such that the power coefficient is reduced as the gap increases. Such effect is relatively small when the gap is increased 1%, but is quite significant as the gap increases further. Meaning that the overall performance is somewhat similar for a certain flap gap range. Notice that the airfoil with a flap gap increased by 1% still shows a satisfactory aerodynamic performance, where a different compromise among the objective functions is provided, therefore, it might be another airfoil of the pareto front or close to it. That's not the case for the flap gap increased by 2% since the drag rises significantly. The reason why the the larger gap results on a higher drag

coefficient at the same C_L can be further studied by plotting the drag coefficient decomposition, i.e., pressure and viscous drag coefficients separately, where the total drag C_D is the addition of the two mentioned drags (for 2D analysis). In order to see clearly the effect on the gap size increase, the two extreme cases are used: selected airfoil and gap increased by 2%, shown in Figure 4.28.

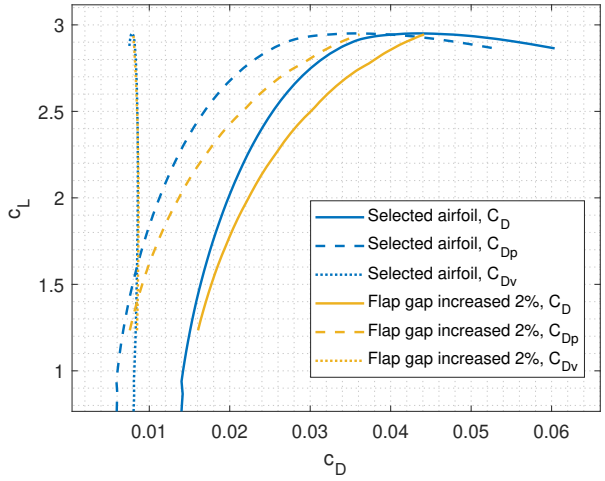

Figure 4.28: Drag coefficient decomposition for the selected airfoil and the airfoil with the gap increased by 2%.

It is shown that the increase of drag is mainly due to an increase of pressure drag, while the viscous drag remains constant as the gap size is increased. Let us then look at the pressure coefficient along the surface for both geometries at the same C_L, Figure 4.29.

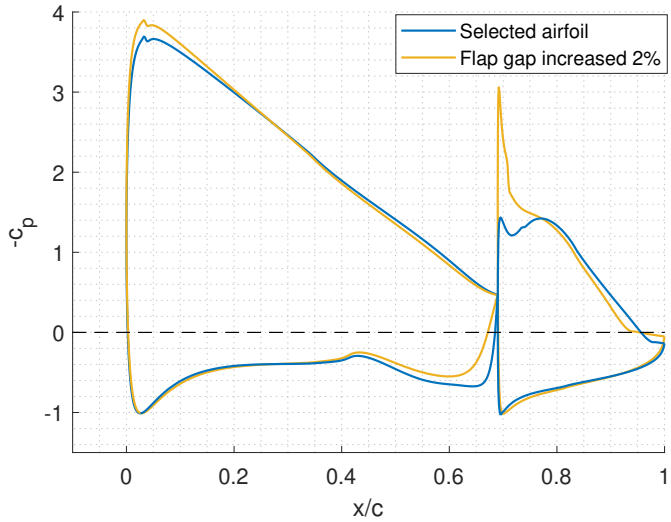

Figure 4.29: Pressure coefficient distribution for the selected airfoil and the airfoil with the gap increased by 2%, at $C_L = 2.3$.

The flap with a bigger gap size shows a drastic suction peak at the flap's leading edge since it is located "more in the freestream" or, in other words, the downwash of the main element to the flap has a smaller effect. Therefore the flap sees a higher effective angle of attack than if it was located closer to the main element. Such suction peak leads to a steeper adverse pressure gradient which results on a slightly earlier flow separation, depicted by the flat plateau at the trailing edge of the flap. Moreover, notice that the rear loading of the main element is lower for the airfoil with a bigger gap, meaning that it has a lower pressure at the TE of lower surface of the main element, where the pressure has a force component opposed to the drag direction. The mentioned effects might well explain why the pressure drag coefficient increases as the flap size increases.

4.6. Return phase

In return phase the kite is reeled in and the winch in the ground station acts as a motor, therefore consuming energy. The consumed energy should be minimized in order to increase the efficiency of the whole cycle. To do so, the tether force while the kite is reeled in should be as low as possible such that the work (force $\times$ displacement) is reduced. The tether force during reel in is mainly a function of the aerodynamic forces (although the kite weight also plays a role). Therefore, the airfoil should be able to reach low loads for the return phase, which is somewhat complex since both the shape and setting has been optimized to reach high C_L's, among other objectives. Such requirement is critical for high wind speed conditions, since the aerodynamic loads will be high, therefore, the lowest lift coefficient will be required.

The industrial partner has computed a minimum C_L of 0.2 for highest operational wind speed condition (cut-out speed), plus a certain margin. An additional safety margin is added to that extreme value to make sure the airfoil covers well the whole operational domain. Therefore, a minimum C_L of -0.1 is required for the airfoil in return configuration.

The C_L-α polar of the airfoil optimized for production phase, given in Figure 4.25 shows that it reaches a minimum $C_L = 0.56$ at an angle of attack of -10º. MSES does not converge below said angle of attack due to massive flow separation on the lower surface of the main element around the TE. Such phenomena can be clearly observed through the streamlines, Figure 4.30 shows the streamlines around the optimized airfoil at α=-10º. Flow separation can also be observed through the pressure coefficient distribution, where flow detachment is depicted by a flat plateau, seen in Figure 4.31.

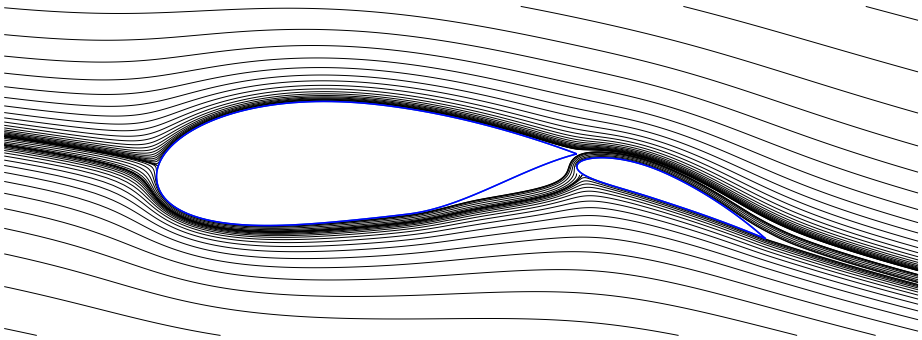

Figure 4.30: Streamlines around the selected airfoil at α=-10º.

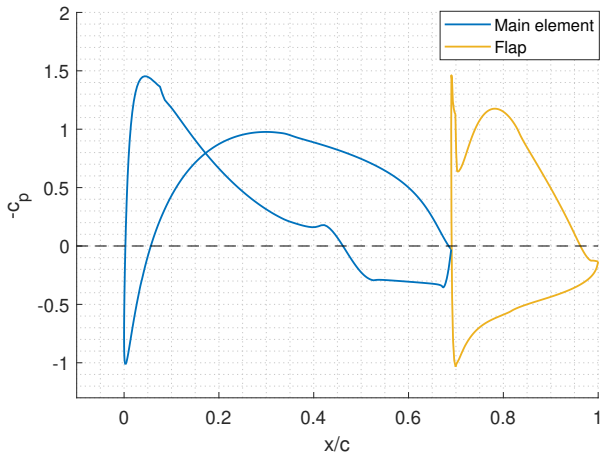

Figure 4.31: Pressure coefficient distribution of the selected airfoil at α=-10º.

Even though MSES does not converge for cases with a big flow detachment region, it is quite useful to predict when this phenomena will take place since it stops converging at that point and the streamlines depict separation clearly (before it stops converging). It is inferred that the C_L-α curve is close to showing non-linear behavior closely below the 'limit' angle of attack, where the 'limit' AoA refers to the smaller AoA for which MSES converges. Therefore, we can employ MSES to estimate approximately until what angle of attack the C_L will be linear and what is the minimum C_L within the linear region. The non-linear region is non desired even though the C_L still decreases, since a non-linear behaviour makes the control of the kite significantly more complex.

It is therefore inferred that the airfoil optimized for production phase is not suitable for return phase as it is since the mentioned lift requirement for return phase is not reached. In order to reach low C_L's the flap can be rotated upwards. However, various flap deflections from a pivot point inside the flap have been tried and flow separation takes place such that a low enough C_L is still not reached. The main reason why flow detachment is taking place is due to the curvature of the lower surface at the TE of the main element which results in the flow decelerating excessively until flow is detached. A possible solution would be to alter said curvature such that the flow is able to stay attached. However, that would be counter productive since that exact shape is the result of the optimization for production mode operation. An alternative solution is to rotate the flap from a pivot point such that the flap ends up at a location that mitigates (or delays to lower AoA) the flow separation phenomena. By locating the pivot point outside the flap, it will not only rotate but also translate. The idea is to move the flap to a position where we can employ the high velocity flow induced by the flap, to accelerate the flow where separation occurs and therefore, mitigate it. In a way, we aim to reenergize the boundary layer at the trailing edge of the main element where it has low kinetic energy and is thus prone to separation. To do that, the pivot points shown in Figures 4.32 and 4.33 are studied. Notice that with the newly introduced pivot points (outside the flap), the rotated flap ends up at a location where there is some overlapping, which is what we are looking for since we want to use the high velocity region induced by the flap.

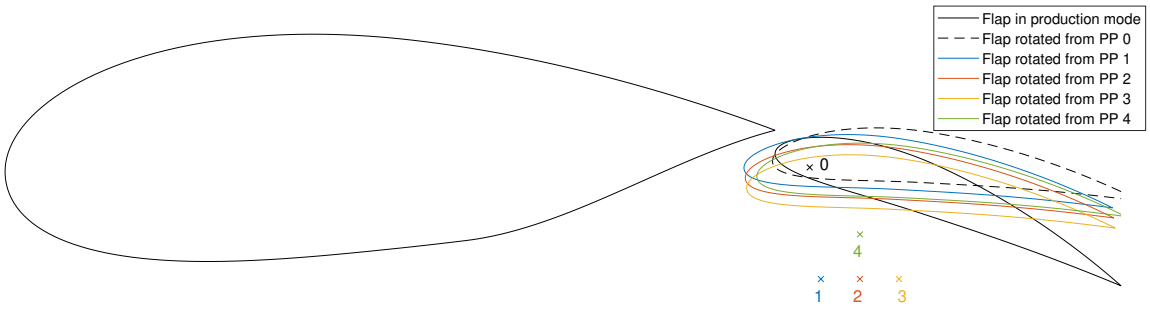

Figure 4.32: Flap rotated upwards for return phase from various pivot points (PP).

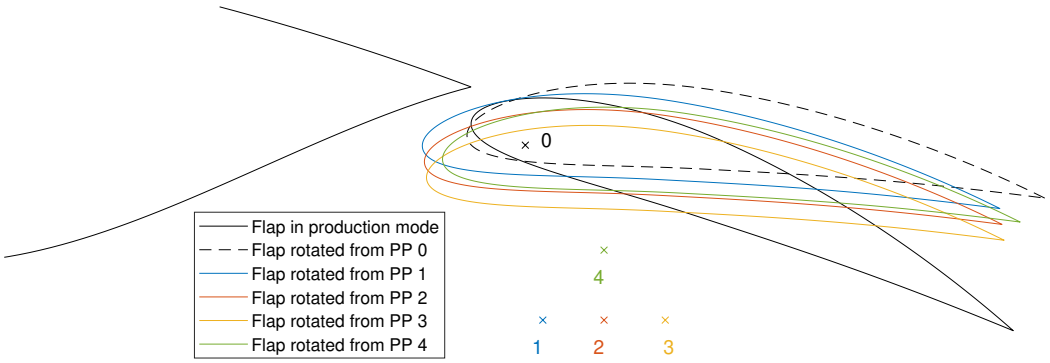

Figure 4.33: Close view of the flap rotated upwards for return phase from various pivot points.

Each C_L-α polar for the 5 airfoils shown in Figure 4.32 are given in Figure 4.34.

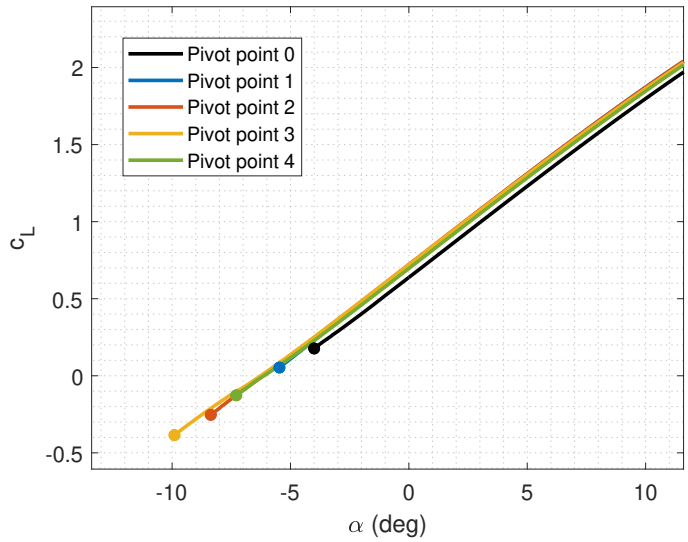

Figure 4.34: C_L-α polar of the airfoil with the flap rotated from various pivot points.

The dot at the end of the curve depicts the last point in the polar that MSES has been able to converge. For angles of attack below that dot, the flow separation region is too big for MSES to converge. Thus, we can assume that the dot is close to the region of the C_L-α curve where it has non-linear behaviour. It is clearly seen that each airfoil has a different minimum C_L showing that the modification of pivot point outside the flap can help delay flow separation and reach lower C_L's. Pivot point number 3 is the one that reaches the lowest C_L among the analysed ones, however, it is also the most complex one to build from a mechanical point of view, since it is further away from the main element. It is convenient to have the pivot point as close to the airfoil as possible both from a mechanical and aerodynamic perspective. The aerodynamic perspective concerns mainly about the drag penalty of having the hinge in the freestream. Taking these considerations into account, the pivot point 4 is selected since it is close to the main element while providing a fairly low linear C_{Lmin}, around -0.1.

The effect of shifting the flap position to mitigate flow separation can be visually shown through the streamlines. Figures 4.35 and 4.36 show the streamlines at the same angle of attack for the two extreme configurations. Those are pivot point 0 (inside the flap), which gives the highest linear C_{Lmin} and pivot point 3, which reaches the lowest linear C_{Lmin}. The angle of attack -4º is employed so that both airfoils can be analysed with MSES, note that the airfoil with pivot point 0 does not converge below said AoA.

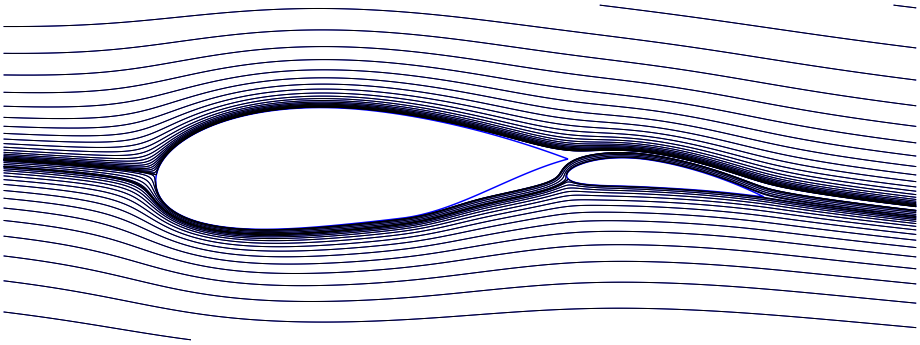

Figure 4.35: Streamlines around the airfoil with the flap rotated from pivot point 0 at α=-4º.

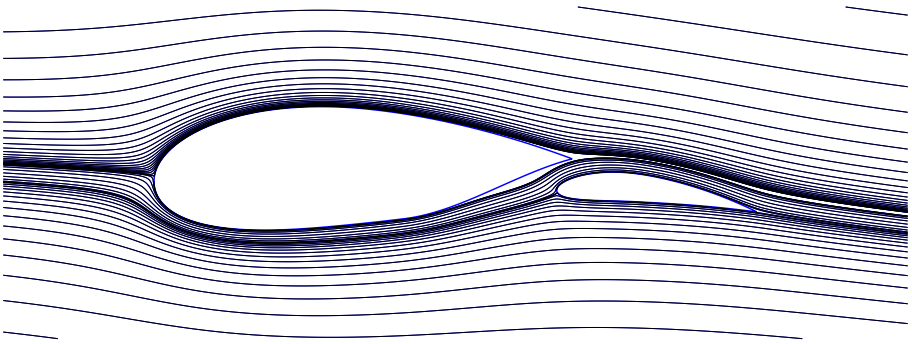

Figure 4.36: Streamlines around the airfoil with the flap rotated from pivot point 3 at α=-4º.

We can clearly observe that moving the flap to a position where there is some overlap between the main element and flap (pivot point 3) results on the flow being more attached to the surface. Thus showing the beneficial effect of having overlap to reach a lower linear C_{Lmin}. This study reaches the conclusion that for the current airfoil optimization, overlap is beneficial for return phase but for production phase an overlap of 0 was reached by the genetic algorithm, such difference variation overlap can be attained through the studied pivot points.

5

Computational Fluid Dynamics verification

Once the airfoil has been designed, its polars are verified with Computational Fluid Dynamics (CFD) simulations. The aim is to compare the polars obtained with MSES to the polars obtained with CFD, a higher fidelity tool, and assess the possible discrepancies. The current chapter provides an overview of the setup for the CFD simulations presenting the workflow of the used programs, the turbulence model and the mesh generation. The given setup is validated with experimental data and lastly, the CFD results are compared to the polars obtained with MSES. In addition, the flow separation phenomena in return phase configuration is also analysed to investigate if CFD and MSES predict similarly such phenomena.

5.1. Setup

5.1.1. Workflow

The workflow for the CFD simulations consisted of three main stages: meshing, solving the flow and data post processing. The meshing of the airfoil geometry has been done through the commercial software Cadence (Pointwise). Cadence is a meshing software that allows high quality meshes as well as scripting through the programming language: Glyph. Scripting the meshing procedure is relevant for the current task since it accelerates vastly meshing similar geometries with small modifications.

Once the mesh is generated, the CFD RANS simulation is performed through the open source software: OpenFOAM. The employed solver is SimpleFoam, a steady-state solver for incompressible, turbulent flow. A turbulence model must be determined to close the RANS equations, which is further presented in the following subsection 5.1.2. These simulations have been carried on in the high performance computer cluster provided by TUDelft, in order to reduce the computational time.

Post processing of the results is done in Paraview, an open source software that gives the flow visualization from the output of the CFD simulation. It was mainly employed to illustrate the flowfield and streamlines around the airfoil. Other post processing data such as convergence plots or pressure distribution along the airfoil have been obtained through self-developed Matlab scripts.

5.1.2. Turbulence model

The employed CFD simulations solve the Reynolds averaged Navier-Stokes equations (RANS). Said equations are derived by time-averaging the flow variables in the Navier-Stokes equations into mean and time-dependent components, this is referred as Reynolds decomposition which splits the problem

in two parts. First, the averaged part is numerically solved, second, the fluctuating part is modelled by a semi-empirical **turbulence model** that closes the RANS equations. Such models are based on the assumption that the effect of turbulence can be seen as an increased viscosity, i.e., *turbulence viscosity*

The result of the CFD simulation is sensitive to the selected turbulence model, therefore it is critical to determine which model to employ. The most widely used models (although not the only ones existing) due to their numerical robustness and accuracy are the following:

- Spalart-Allmaras: one-equation model by [60] which solves the transport equation for the eddy viscosity.
- k-ε: two-equations model by [45], k for turbulent kinetic energy and ε for turbulent dissipation rate. It gives good results for external flows, should be applied to flows without strong pressure gradient or separation.
- k-ω: two-equations model by [70], k for turbulent kinetic energy again and ω the turbulence dissipation rate per unit energy. It gives very good results for boundary layer flows, for flows with pressure gradients and separation. It is, however, quite sensitive to freestream boundary conditions, that is why k-ε performs better for external flow.

None of the existing turbulence models work universally for all types of flows, hence, it is paramount to assess the suitability of said turbulence models for each case. As recommended in [7, 30] and [55], a very suitable option for airfoil analysis (or for a leading edge inflatable kite airfoil in the case of [30]) is the k-ω Shear stress transport (SST) model proposed by [49], which combines the k-ε and the k-ω to get the best of both models. The use of a k-ω formulation in the inner parts of the boundary layer makes it suitable until the wall through the viscous sub-layer. The SST model then switches to a k-ε behaviour in the freestream and therefore avoids the common k-ω issue that the model is too sensitive to the freestream boundary conditions at the inlet. Authors who use the SST model often merit it for its good behaviour in adverse pressure gradients and separating flow.

That being said, the selected turbulence model is the k-ω SST since it seems to give a superior results according to the mentioned literature. However, it will be compared to the k-ε to see how they compare in terms of flow separation. Such comparison is shown in the subsection 5.1.4: Validation of the setup.

5.1.3. Mesh

As previously mentioned, the analysed airfoils have been meshed through Cadence. The mesh topology is based on a hybrid mesh, structured on the airfoil surface and the wake and unstructured otherwise. Figure 5.1 shows the topology of the mesh were the structured and unstructured regions are depicted.

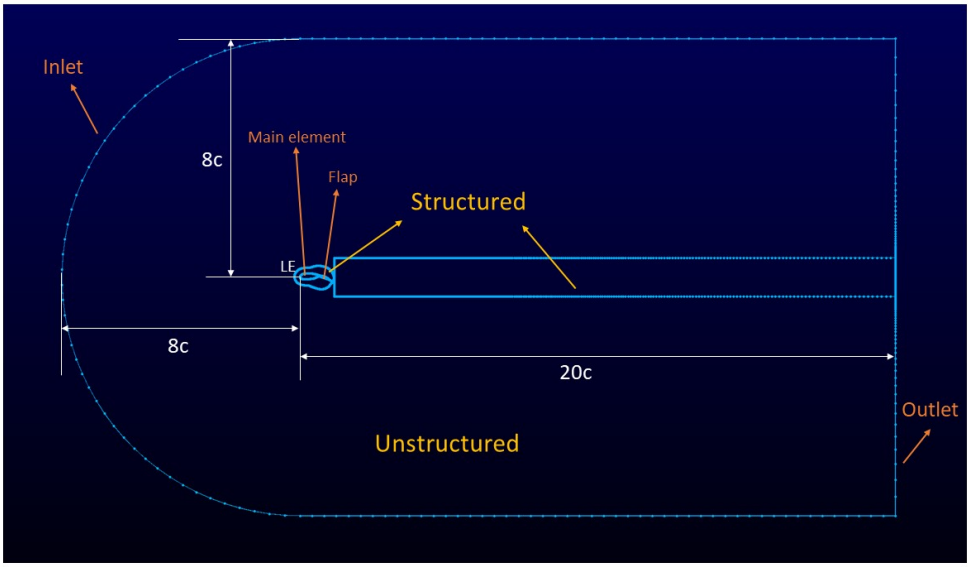

Figure 5.1: Topology of the hybrid mesh.

The outlet is at a distance of 20 chords $(20c)$ from the airfoil's leading edge and the inlet is at $8c$ from the LE, both horizontally and vertically since the inlet arc has the center on the LE. The simulation is a *pseudo-2D* simulation, i.e, the mesh is actually 3D but it is extruded one single cell such that the properties in the out-of-plane direction do not vary, thus simulating a 2D case.

The reason behind employing a hybrid mesh is that the flow solver is benefited from having the cells on the boundary layer orthogonal to the flow, therefore structured is recommended on the surface. On the other hand, in the region far from the airfoil and wake it is feasible to employ a sparser unstructured mesh leading to a reduced total cells number. The wake is meshed with a structured rectangular block since it gives simple direct control on the cells size distribution.

The structured mesh around the airfoil surface is an O-grid type, obtained through a hyperbolic extrusion such that the first cell is orthogonal all around the surface of both elements, see Figure 5.2.

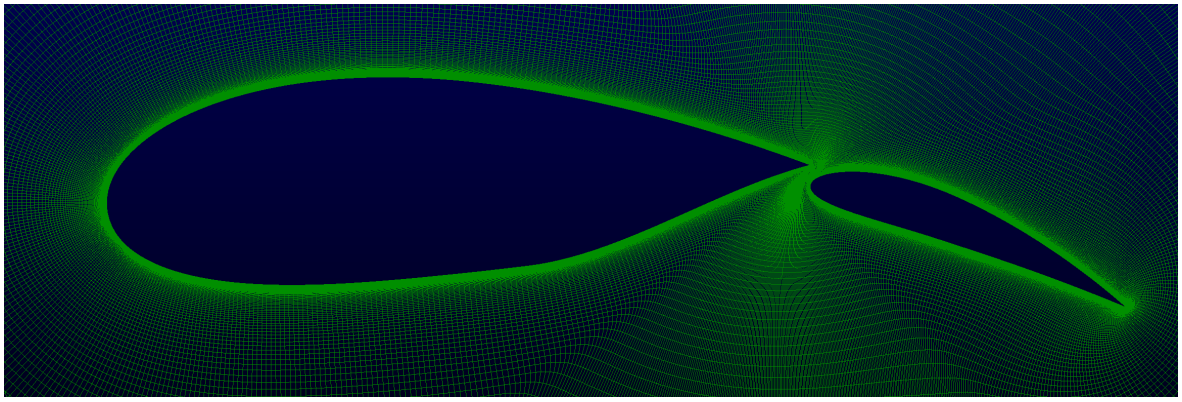

Figure 5.2: Structured hyperbolic mesh close to the airfoil surface.

The most challenging region to mesh is the gap between the two elements, due to its complex geometry. It is also critical to mesh said region properly since gradients of pressure and velocity are expected to occur. Figure 5.3 shows the mesh in the gap region, where the hyperbolic extrusion uses a link between the main element TE and the flap LE, resulting on a good quality mesh.

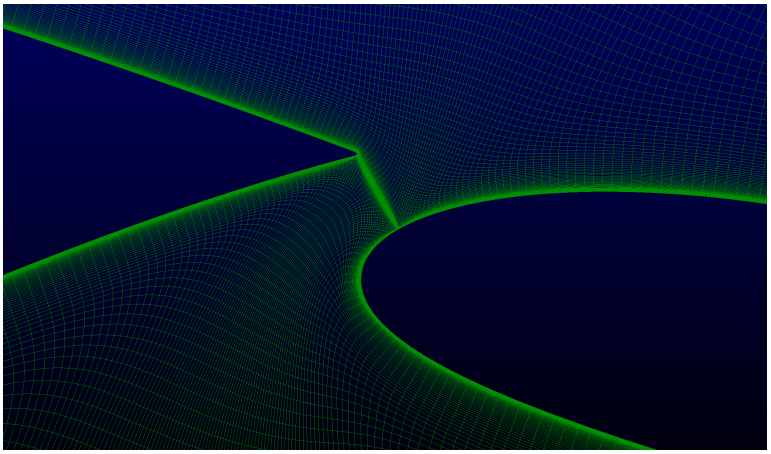

Figure 5.3: Mesh in the gap between the two elements.

Far from the airfoil and the wake, the mesh becomes unstructured and sparser, as shown in Figure 5.4.

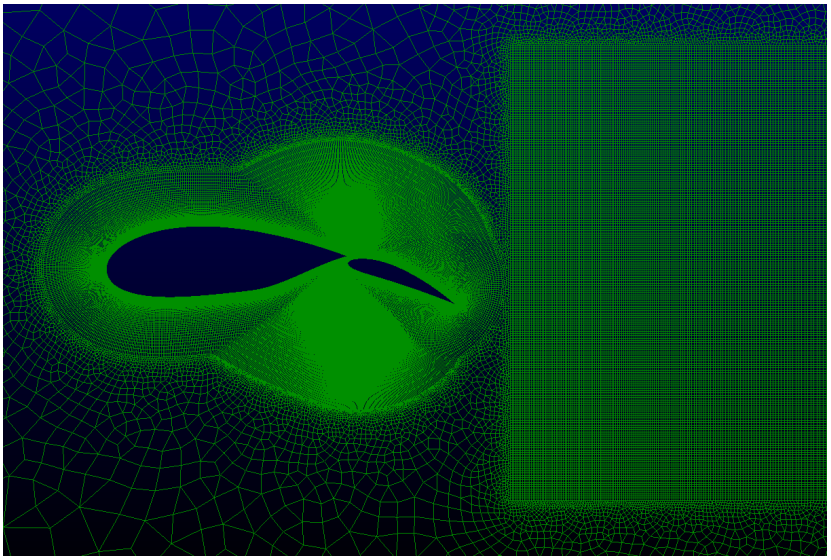

Figure 5.4: Transition from structured to unstructured mesh.

The unstructured mesh has been generated through an algorithm provided in Cadence called T-rex [62], which stands for anisotropic tetrahedral extrusion. The main advantage of this mesh generation method is that it can resolve boundary layers, wakes, and other phenomena in viscous flows although it was not used to that purpose for the current work. It was selected since its predominance for quadrangular cells resulted in a rather smooth transition from structured to unstructured mesh.

One of the main benefits of employing a structured mesh on the airfoil surface is that the height of the first cell is easily controllable, therefore, managing the y^+ becomes straightforward. Moreover, the y^+ along both element's surface is constant. A common recommendation from literature ([2, 51, 48]) is to use a value of y^+ below 1. Such approach results in the boundary layer being resolved, including the viscous sub-layer. If the y^+ is increased to values above 20-30, the wall function is used which models the boundary layer through the log law, [68, 67].

In order to determine the y^+ to use, a sensitivity analysis has been performed. The height of the first cell, i.e., the y^+ has been progressively reduced to see how the aerodynamic coefficients C_L and C_D vary. However, if only the height of the surface cells is decreased, the aspect ratio of those cells increases significantly. To avoid extremely high values of aspect ratio, the length of the cells in the

surface direction is also reduced accordingly with the height. Each combination of width and height of the surface cells is a level of discretization and the higher the level, the finer the mesh. The mesh sensitivity is shown in Figure 5.5 and the features of each level of discretization are given in Table 5.1.

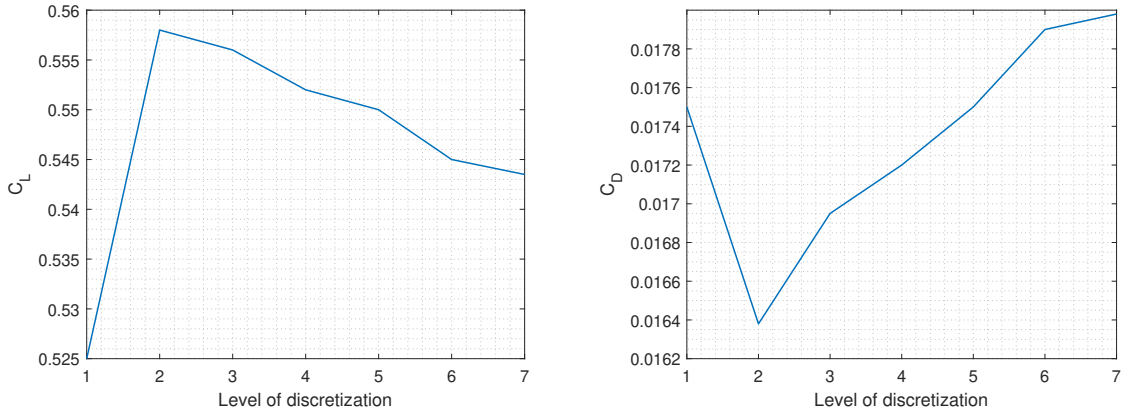

Figure 5.5: Aerodynamic coefficients sensitivity to the mesh level of discretization.

Level of discretization	Height of first cell	y^+	C_L	C_D
1	$2 \cdot 10^{-3}$	230	0.525	0.0175
2	$2 \cdot 10^{-4}$	23	0.558	0.0164
3	$2 \cdot 10^{-5}$	2.29	0.556	0.0169
4	$1 \cdot 10^{-5}$	1.15	0.552	0.0172
5	$5 \cdot 10^{-6}$	0.57	0.550	0.0175
6	$2 \cdot 10^{-6}$	0.23	0.545	0.0179
7	$1 \cdot 10^{-6}$	0.11	0.544	0.0180

Table 5.1: Properties of the employed levels of discretization.

It is shown in Figure 5.5 that the aerodynamic coefficients become rather insensitive to the mesh for values of y^+ below 0.23. Notice that the relative variation of the lift coefficient above the second level of refinement, i.e., below $y^+ = 23$ is less than 3%. On the other hand, the drag coefficient does vary significantly in that same range, with a variation close to 9%. The sparsest level of discretization has been included in order to see how the aerodynamic coefficients vary when 'switching on' the wall function. It is inferred that employing a small y^+ (around $y^+ \approx 0.2$) is preferred since the results become insensitive to the mesh.

One of the main advantages of employing Cadence to mesh our geometry is that it offers certain functionalities that allow the user to easily script the meshing procedure. By scripting the actions done to mesh the airfoil, we can automatically mesh for different geometries with small variations. In the script, variables can be defined such that the relevant mesh parameters can be easily modified.

Once the mesh is generated, its quality is reviewed through the integrated OpenFOAM function: *checkMesh*. This function checks for several mesh properties such as maximum aspect ratio, maximum skewness, mesh non-orthogonality or minimum volume. An ill-defined mesh can be detected by using this function and prevents the solver from diverging or encountering errors.

5.1.4. Validation of the setup

Before verifying the MSES polars with the CFD setup, it is positive to validate the setup with a simple case to benchmark it and check its accuracy with respect to experimental data. The airfoil selected

to perform the validation is a NACA 2424 (see Figure 5.6), its experimental polars are obtained from [1].

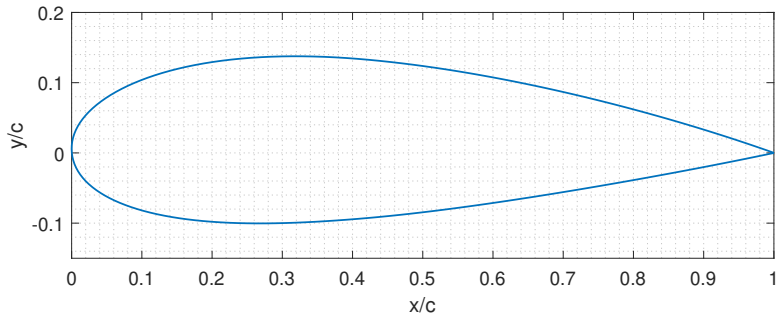

Figure 5.6: NACA 2424.

The mesh used for this case has the same topology as the one presented in the previous subsection (5.1.3: Mesh), with the added ”simplicity” of not having a gap since we are now dealing with a single-element airfoil. The Reynolds number is adjusted to $Re = 2.9 \cdot 10^6$ to use the same as in the experimental simulation and the CFD simulation is performed with a fully turbulent boundary layer so the turbulent experimental C_D polar is used for the validation. The reason to employ a fully turbulent BL is that the airfoil is designed for turbulent conditions as justified in Section 4.2. As mentioned in the subsection 5.1.2: Turbulence model, both the $k-\omega$ SST and $k-\varepsilon$ are used to validate the setup, shown in Figure 5.7.

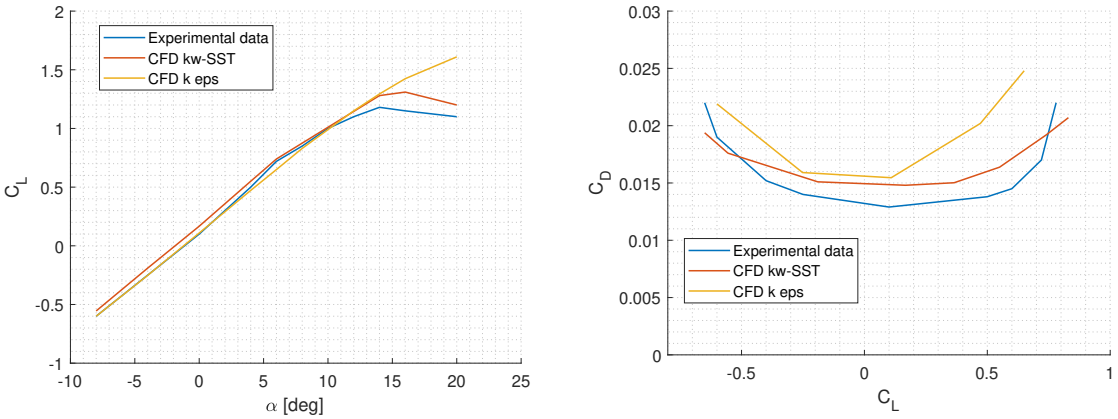

Figure 5.7: Setup validation with experimental data from [1].

The validation shows that the turbulence model $k-\omega$ SST performs significantly better than the $k-\varepsilon$. The setup with $k-\omega$ SST predicts accurately the lift coefficient in the linear region and captures fairly well the stall region, where the maximum lift is slightly overpredicted. In terms of drag, the CFD simulation overestimates it but it lays rather close to the experimental, within a 13% of relative error approximately. The setup with $k-\varepsilon$ as turbulence model is also accurate in terms of lift in the linear region but is not capable of capturing the flow separation in the stall region, as has been anticipated in the subsection 5.1.2. In order to visualize the difference of both turbulence models in the stall region, the flowfield at the same AoA, α =16º, is shown in Figure 5.8, where it is observed that the separation region for the simulation with $k-\varepsilon$ is considerably smaller. Moreover, the drag is significantly overestimated all along the C_D polar. It is therefore confirmed that $k-\omega$ SST is preferred and the setup is deemed to be satisfactory.

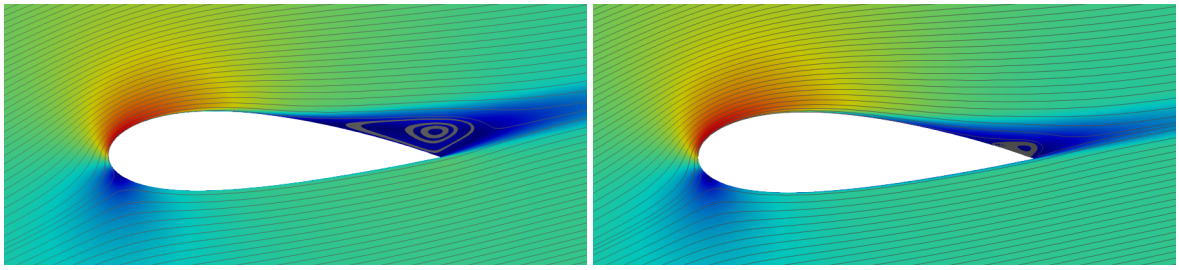

(a) Flowfield for an α =16º with the turbulence model $k-\omega$ SST.

(b) Flowfield for an α =16º with the turbulence model $k-\varepsilon$.

Figure 5.8: Comparison of flowfield at stall region for the CFD simulations with different turbulent models.

5.2. Verification results

5.2.1. Convergence criteria

The criteria to terminate the CFD simulations was the root mean square (RMS) of the residuals from the continuity and momentum equations, a value of 10^{-7} was considered to be small enough to finish the simulation. In case the residuals limit was not reached, a maximum number of iterations was set to 1000. Such cases mainly occurred when the forces showed a certain oscillation, for those cases, user interference was critical to check if the oscillations are within an acceptable range. To do so, the force coefficients as function of the iteration number were plotted through Matlab.

5.2.2. Polars comparison

The current section presents the comparison of the aerodynamic coefficients obtained with MSES and CFD-RANS simulations. Figure 5.9 shows the polars of the optimized airfoil in production configuration, i.e, flap down configuration. It is observed that the lift coefficient are almost on top of each other, although there seems to be a small offset of lift coefficient; CFD gives a slightly lower C_L all along the angles of attack range. MSES captures well the maximum lift coefficient although it takes place at a slightly lower AoA wrt the CFD result. The somewhat underpredicted C_L in the linear region is also found in [29] where it is regarded as a consequence of the flow between elements not being well captured by MSES, in said literature, a good agreement in C_{Lmax} is also obtained.

Regarding the drag coefficient, MSES significantly underpredicts it wrt to CFD, where the discrepancy is more conspicuous for high angles of attack. In order to further investigate in such difference of drag, the drag breakdown is plotted in Figure 5.10. The drag coefficient is split into its two contributions: viscous drag and pressure drag (two contributions in 2D flow), to see which contribution is leading to the difference of drag seen in Figure 5.9b.

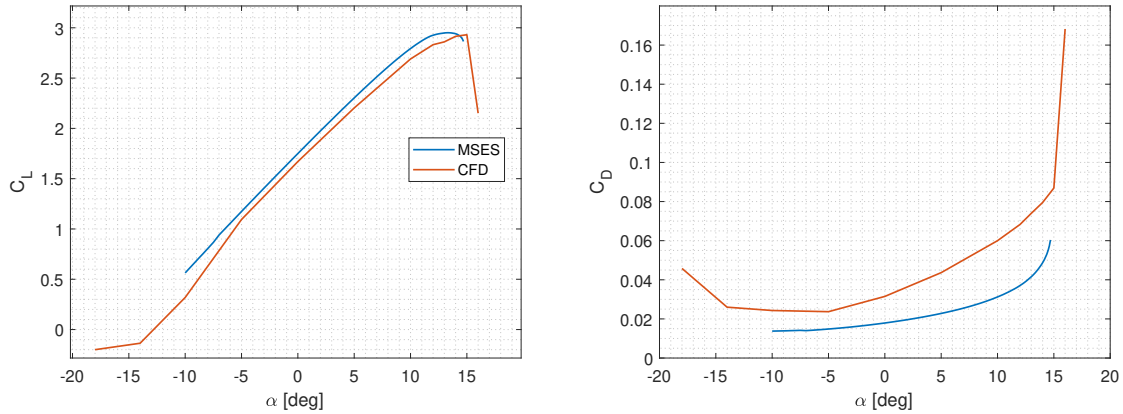

(a) Verification of C_L polar.

(b) Verification of C_D polar.

Figure 5.9: Verification of the polars for the airfoil in production configuration (flap down).

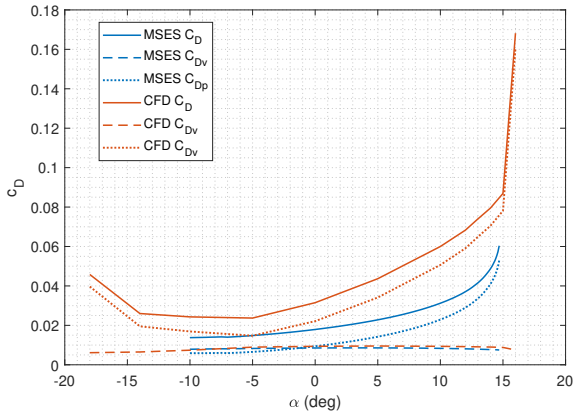

Figure 5.10: Comparison of the drag breakdown.

The drag coefficient breakdown in Figure 5.10 shows that both tools give the same viscous drag, and the pressure drag is the contribution underpredicted by MSES. MSES underpredicting drag was anticipated in the literature study since other authors ([29, 61, 35, 27, 15] and [26]) have found similar results when verifying it against RANS solvers for multi-element airfoils, where [27, 15] and [26] are highlighted since the analysed airfoils had AWE applications. For the case of [26], MSES also shows significant lower C_D where it is justified with the flow separation phenomena, however, in that case 3D CFD simulations are employed so flow separation has a larger effect.

The polars for the optimized airfoil in return configuration, i.e. flap down, are also verified leading to similar conclusions. The maximum lift coefficient is again well captured although it takes place at a slightly smaller angle of attack according to MSES. The drag coefficient also shows a similar behaviour wrt to the polars for the airfoil in production configuration, however, in this case the drag curves seem to show a better agreement.

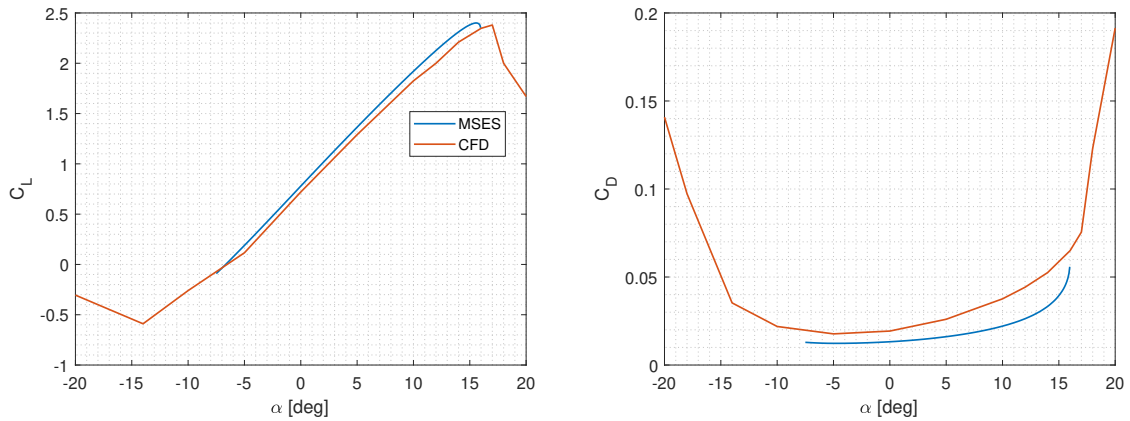

(a) Verification of C_L polar.

(b) Verification of C_D polar.

Figure 5.11: Verification of the polars for the airfoil in return configuration (flap up).

It is also relevant to see the limitation of MSES in the low angle of attacks region, where it stops converging as soon as a big recirculation area takes place on the lower surface TE of the main element. The verification therefore shows that MSES is not capable of reaching the non-linear region in the low AoA side, such information can be used by the user to infer approximately at what AoA does the polar reach non-linear behaviour since non-linearities are expected somewhat close below the 'limit' AoA, as seen in Figures 5.9a and 5.11a.

The flowfield obtained with the CFD simulations for the airfoil in both production and return configuration at several AoA's are shown in the Appendix B.

5.2.3. Flowfield in return phase configuration

When designing the airfoil for return phase configuration, a modification on the pivot point was implemented in order to vary the flap up position such that the flow separation is mitigated on the lower surface of the main element for low AoA's. Such effect was analysed in MSES so the aim in this section is to visualize it through the CFD simulations. Figure 5.12 shows the flowfield for the airfoil in return configuration with the flap in the initial position, i.e., without having mitigated flow separation through the shift in pivot point. The following Figure, 5.13, shows the flowfield for the case were the flap position has been altered. It is clearly shown that the effect previously seen in MSES is supported by the CFD simulations, since the flow separation region is distinctly reduced. The effect of reenergizing the exhausted boundary layer on the lower surface TE of the main element by means of the high velocity induced by the flap's LE is now depicted by the colour giving the flow velocity.

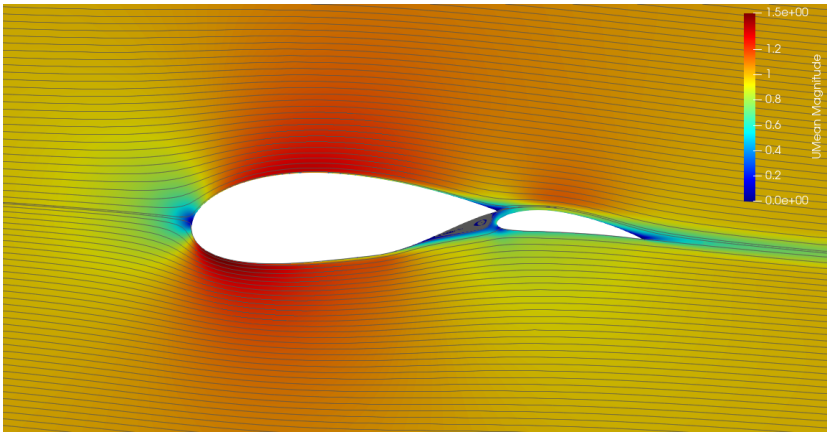

Figure 5.12: Flowfield with streamlines with the initial flap setting for return phase (hinge point inside the flap), where flow separation is shown. The angle of attack is α=-4°.

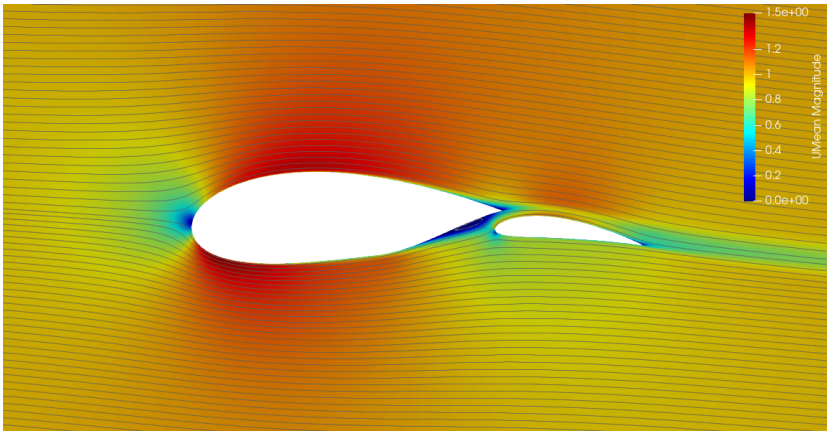

Figure 5.13: Flowfield with streamlines with the designed flap setting for return phase (hinge point outside the flap), where flow separation is mitigated. The angle of attack is α=-4°.

6

Conclusions & Recommendations

This chapter presents first the conclusions on the overall optimization and verification procedure after which recommendations for future research will be suggested.

6.1. Conclusions

In the presented thesis, a two-element airfoil has been designed through optimization for a rigid kite with AWE applications. The kite operates in a pumping cycle mode (ground-gen), therefore has two operational phases where the design requirements are totally distinct: production and return phase. Both phases have been taken into account in the design process by optimizing the airfoil for production phase first, and then evaluating and adapting it to perform efficiently in both phases, such that the airfoil has two flap settings. The aerodynamic performance of the resulting multi-element airfoil has been verified by comparing the C_L and C_D polars with CFD RANS simulations. The conclusions derived from the described process are hereby presented.

The first step to optimize a multi-element airfoil is to define its parametrization, i.e., the design variables that define its geometry. The goal when developing a parametrization scheme is to have a flexible geometry with shape control in the relevant regions of the airfoil without having an excessively high number of design variables. Such compromise has been achieved through a combination of the NACA 4-digits nomenclature for both elements combined with a modification on the TE of the main element, to enhance the flap integration. The relative position between the two elements is parametrized through the typical variables: gap, overlap, flap chord and deflection, thus providing the whole scope of relative positions. Moreover, such parametrization scheme allows a simple constraint of the elements' thickness, which is required due to structural reasons. The developed method for airfoil parametrization has been therefore deemed as suitable for our design problem.

The optimization strategy is based on a multi-objective genetic algorithm implemented in Matlab and coupled to MSES, a 2D aerodynamic solver employed for design and analysis of multi-element airfoils with low computational cost. The genetic algorithm has been found to be suitable for the optimization procedure due to its robustness in finding the global optima in such a highly non-linear design space as well as its capability of finding the pareto front, significant for a multi-objective problem. Coupling effects between the shape-related and setting-related variables have been observed, therefore, optimizing the airfoil by subdividing the problem is not recommended with the employed parametrization. It has also been found that employing a gradient-free method such as a GA is beneficial since the sensitivity information might not be available along the whole design space due to the found MSES convergence issues. Despite such issues, MSES has been selected as the solver for the optimization due to its low computational cost, fairly accurate results and good suitability to being coupled with an optimization algorithm since it can be easily executed from Matlab. Furthermore, a relevant feature of MSES for this application is that a high quality mesh is automatically generated for each particular geometry. Its main found issue is that it does not reach convergence for some

analysis and such cases are quite detrimental for the optimization process. However, the amount of unconverged cases has been reduced by carefully adjusting the mesh parameters. In addition, the unfavourable effect of an unconverged case has been mitigated by employing the human-in-the-loop technique, i.e. the designer has monitored and manually analysed the required cases so that the algorithm can successfully carry on.

The objectives of the optimization have been identified, first for the production phase, which have been implemented in the optimization algorithm and then, for the return phase. In the production phase three objectives have been prioritized with the goal of maximizing the power output. To that end, the operational C_L as well as the power coefficient C_L^3/C_D^2 along the whole operational range are to be maximized. Since the kite operates at a wide range of C_L's, the power coefficient has been considered at two representative C_L's, such that the whole operational scope is represented. In order to implement the optimization algorithm, the design variables have been progressively added into the algorithm, allowing us to observe that the algorithm is able to reach a better airfoil the more it can alter the airfoil geometry. The convergence of the MOGA and its termination criteria has also been shown for a simplified problem. However, due to the computational cost of the genetic algorithm, in some cases the optimization run has been halted before reaching the termination criteria if all individuals (airfoils) start to converge towards a promising individual.

The result of the optimization is the pareto front, from where an airfoil has been selected according to its compromise among the various objective functions. Such airfoil has been shown to have a satisfactory performance for production phase according to its polars from MSES. The challenge then is to adapt such airfoil for return phase as well. Low aerodynamic loads are required for return phase in order to have an efficient power cycle. To that end, the flap has been rotated upwards, however flow separation has been observed for low AoA. In order to mitigate that effect, the flap has been rotated from a specific pivot point such that the flap in flap-up configuration has a certain overlap with the main element. That is desired so that the high velocity flow induced by the flap reenergizes the BL in the detached flow region. Such feature has been proved to delay flow separation to lower AoA's and thus allow lower C_L's. Therefore, it has been inferred that a certain overlap between the main element and flap is beneficial for the return phase, while the optimized airfoil for production phase has an overlap close to zero. This difference in overlap can be achieved by locating the flap rotational point outside the flap, such that the flap is both rotated and translated. The airfoil in production configuration (flap down) has been subject to a preliminary analysis to assess the effect of gap variation. Such study has been done since the wing for which the airfoil is designed will experience significant wing bending in the spanwise direction, and thus the gap will vary along the span during its operation. The analysis has shown that the gap variation does not alter significantly the performance for a specific flap gap range, however, above a certain threshold its aerodynamic performance considerably decays due to an increase of pressure drag.

Once the airfoil has been designed, its aerodynamic performance has been verified through CFD RANS simulations, using the open source software OpenFOAM. The CFD setup has been first validated with the experimental data of a single-element airfoil which has shown fairly good agreement. The selected turbulence model has been $k-\omega$ SST due to its superior performance in dealing both external flows as well as the boundary layer flow, as has been inferred from the literature study. Nonetheless, it has been compared to the $k-\epsilon$ which has clearly shown that $k-\epsilon$ does not capture well the separated flow in the stall region. A hybrid mesh has been constructed through the software Cadence, which allows to be scripted, thus simplifying greatly the process of analyzing different airfoil geometries. The verification results show a fairly good agreement of the lift coefficient both in the linear region and the maximum C_L. On the other hand, the drag coefficient is significantly underpredicted by MSES where the pressure drag has been shown to be the contribution leading to such discrepancy in drag. The flow separation phenomena in the return phase has also been analysed with CFD analysis. The improvement achieved with the MSES analysis by varying the location of the flap rotational point is also seen in the flowfield visualizations obtained with the CFD simulations.

6.2. Recommendations for future work

This thesis has optimized a two-element airfoil, where the reasoning behind employing two elements comes from the goal of increasing the design C_L. To that end, a three-element airfoil would also be worth investigating and optimizing. Such design was discarded for the current work due to time constraints and the significant added complexity. Even though it was discarded, several attempts were done to analyse three-element airfoil (consisting of a slat, main element and flap) with MSES and convergence was not reached in the majority of cases. Therefore, the approach used in the current thesis might not be suitable for three-element airfoils. CFD simulations might be required which would lead to reconsider the whole optimization process, since a GA coupled with a CFD RANS solver might well have a computational time of the order of days. A potential solution could be a surrogate model, as employed by [41].

Other recommendations for future work are related to the CFD verification. The CFD setup employed to verify has been validated in the current thesis with a single element airfoil such that it can be easily benchmarked, without having to consider the effect of a slot. However, it would be valuable to validate it with both single and two-element airfoil to see if the addition of an element varies the agreement with experimental data. On the other hand, the C_D discrepancy between MSES and CFD RANS seems to be very common as seen in literature but it would be worth to further investigate in such disparity. Regarding the mesh, a hybrid mesh has been employed where the transition from structured to unstructured is somewhat smooth with the T-rex algorithm, however, its parameters could be further tuned to reach a more progressive transition.

The airfoil has been designed for specific flow conditions, considering a Reynolds number representative for the whole wing. Nonetheless, the kite for which the airfoil is designed is most likely to have a significant variation of chord along the span, such that the Reynolds number also varies along the span. In order to improve the design of the whole wing, different Reynolds numbers could be considered for the optimization since a different flow condition might well converge to a slightly different optimized airfoil geometry. Similarly, the airfoil has been designed assuming a turbulent BL since the impurities on the LE of the wing will trigger the transition to turbulent flow. However, it would be valuable to optimize assuming a clean LE as well to see how the performance varies, since the wing will remain clean for a certain operational time.

References

[1] Ira H. Abbott and Albert E. Von Doenhof. “Theory of Wing Sections”. In: *Physics Bulletin* 11.10 (1960). ISSN: 0031-9112. DOI: 10.1088/0031-9112/11/10/006.

[2] SMA Aftab et al. “Turbulence model selection for low Reynolds number flows”. In: *PloS one* 11.4 (2016), e0153755.

[3] Uwe Ahrens, Moritz Diehl, and Roland Schmehl. *Airborne wind energy*. Springer Science & Business Media, 2013.

[4] Bechtle et. Al. “wind data: ERA5.” In: ().

[5] J.D. Anderson. *Fundamentals of Aerodynamics*. 6th international ed. New York, United States: McGraw Hill Education, 2017.

[6] Florian Bauer et al. “Drag power kite with very high lift coefficient”. In: *Renewable energy* 118 (2018), pp. 290–305.

[7] Ernesto Benini, Rita Ponza, and Andrea Massaro. “High-lift multi-element airfoil shape and setting optimization using multi-objective evolutionary algorithms”. In: *Journal of Aircraft* 48.2 (2011).

[8] Stefano Bortolotti. “A fully automated optimisation procedure for multi-airfoil configurations based on CFD”. In: *Politecnico di Milano* (2021).

[9] H. X. Chen et al. “GA optimization design of multi-element airfoil”. In: *7th International Conference on Computational Fluid Dynamics, ICCFD 2012* (2012), pp. 1–6.

[10] Haixin Chen et al. “GA optimization design of multi-element airfoil”. In: *Seventh International Conference on Computational Fluid Dynamics (ICCFD7)*. 0.32. 2012, pp. 0–34.

[11] S. Chen, F. Zhang, and M. Khalid. “Aerodynamic optimization for a high-lift airfoil/wing configuration”. In: *Collection of Technical Papers - AIAA Applied Aerodynamics Conference* 1.August (2004), pp. 676–683. ISSN: 10485953. DOI: 10.2514/6.2004-5078.

[12] Antonello Cherubini et al. “Airborne Wind Energy Systems: A review of the technologies”. In: *Renewable and Sustainable Energy Reviews* 51 (2015), pp. 1461–1476. ISSN: 1364-0321. DOI: https://doi.org/10.1016/j.rser.2015.07.053. URL: https://www.sciencedirect.com/science/article/pii/S1364032115007005.

[13] IPCC Climate Change. “Synthesis Report Summary Chapter for Policymakers”. In: *IPCC* 2014 (2014), p. 31.

[14] Roger Coenen. “Single Skin Kite Airfoil Optimization for AWES”. In: (2018). URL: http://resolver.tudelft.nl/uuid:fdcf8423-11f0-4b33-956e-3e761635ac41.

[15] G. De Fezza and S. Barber. “Parameter analysis of a multi-element airfoil for application to airborne wind energy”. In: *Wind Energy Science* 7.4 (2022), pp. 1627–1640. DOI: 10.5194/wes-7-1627-2022. URL: https://wes.copernicus.org/articles/7/1627/2022/.

[16] G De Oliveira. “Wind turbine airfoils with boundary layer suction: a novel design approach”. In: (2011).

[17] Kalyanmoy Deb. “Multi-objective optimisation using evolutionary algorithms: an introduction”. In: *Multi-objective evolutionary optimisation for product design and manufacturing*. Springer, 2011, pp. 3–34.

[18] Kalyanmoy Deb et al. “A fast elitist non-dominated sorting genetic algorithm for multi-objective optimization: NSGA-II”. In: *International conference on parallel problem solving from nature*. Springer. 2000, pp. 849–858.

[19] M Drela. *MSES Multi-element Airfoil Design/Analysis Software–Summary*. 1994.

[20] M. Drela. “XFOIL 6.94 User Guide”. In: (2001).

[21] Mark Drela. “A User ’ s Guide to MSES 3 . 05”. In: July (2007).

[22] Mark Drela. “A User’s Guide to LINDOP V2 . 5”. In: *Optimization* June (1996).

[23] Mark Drela. “Design and optimization method for multi-element airfoils”. In: *AIAA/AHS/ASEE Aerospace Design Conference, 1993* (1993). DOI: 10.2514/6.1993-969.

[24] Mark Drela. “Newton solution of coupled viscous/inviscid multielement airfoil flows”. In: *21st Fluid Dynamics, Plasma Dynamics and Lasers Conference*. 1990, p. 1470.

[25] Mark Drela. “Pros and Cons of Airfoil Optimization Pros_Cons_Airfoil_Optimization.pdf”. In: November 1998 (1998), pp. 1–19. DOI: 10.1142/9789812815774.

[26] Christoph Drexler. *Design by Optimization of a Multi-Element Airfoil for Drag Power Kite*. TECHNISCHE UNIVERSITÄT MÜNCHEN, 2019.

[27] Paula Echeverri et al. *The Energy Kite-Selected Results From the Design, Development and Testing of Makani’s Airborne Wind Turbines-Part 1*. Tech. rep. Technical Report 1, Makani Power, https://storage. googleapis. com/x-prod …, 2020.

[28] *Find pareto front of multiple fitness functions using genetic algorithm - matlab gamultiobj - mathworks españa*. URL: https://es.mathworks.com/help/gads/gamultiobj.html.

[29] Dino Florjancic. “Improved design of a high lift system for general aviation aircraft”. In: (2015).

[30] Mikko Folkersma, Roland Schmehl, and Axelle Viré. “Boundary layer transition modeling on leading edge inflatable kite airfoils”. In: *Wind Energy* 22.7 (2019), pp. 908–921. ISSN: 10991824. DOI: 10.1002/we.2329.

[31] Gustavo E Fujiwara, Daniel Chaparro, and Nhan T Nguyen. “An Integral Boundary Layer Direct Method Applied to 2D Transonic Small-Disturbance Equations”. In: *34th AIAA Applied Aerodynamics Conference*. 2016, p. 3568.

[32] PE Gill. “W. Murray, and MH Wright”. In: *Practical Optimization* (1981), pp. 212–229.

[33] Sobieczky H. *Parametric airfoils and wings*. Notes Numer Fluid MEch, 1999.

[34] Thomas Hansen. “Aerodynamic Optimisation of Airfoils and Winglets for Wind Turbine Application”. In: (2017).

[35] Michael Hölling, Joachim Peinke, and Stefan Ivanell. *Wind energy-Impact of turbulence*. Vol. 2. Springer Science & Business, 2014.

[36] TJR Hughes, G Scovazzi, and LP Franca. *Multiscale and stabilized methods,[in:] E. Stein, R. de Borst, and TJR Hughes,[eds.], Encyclopedia of Computational Mechanics*. 2004.

[37] P Iannelli and D Quagliarella. “Multi-objective/multi-point shape and setting high-lift system optimization by means of genetic algorithm and 2D Navier-Stokes equations”. In: *EUROGEN 2011 Conference proceedings, Capua, Italy*. 2011.

[38] J.N. Jacobs, K.E. Ward, and R.M. Careas. “The Characteristics of 78 Related Airfoil Sections Sections From Tests In The Variable-Density Wind Tunnel”. In: *National Advisory Commitee for Aeronautics* (1935). ISSN: 1098-6596.

[39] Joseph Katz and Allen Plotkin. *Low-Speed Aerodynamics. Cambridge*. 2001.

[40] Sangfao Kim, Joan J. Alonso, and Antony Jameson. “Multi-element high-lift configuration design optimization using viscous continuous adjoint method”. In: *Journal of Aircraft* 41.5 (2004), pp. 1082–1097. ISSN: 15333868. DOI: 10.2514/1.17.

[41] E J Kroon. “Aerodynamics and Wind Energy Airborne Wind Energy Airfoils Design of Pareto-optimal airfoils for rigid wing systems in the field of Airborne Wind Energy”. In: (2018).

[42] Brenda M. Kulfan. “A universal parametric geometry representation method - ”CST””. In: *Collection of Technical Papers - 45th AIAA Aerospace Sciences Meeting* 1 (2007). DOI: 10.2514/6.2007-62.

[43] Brenda M. Kulfan. “Recent extensions and applications of the ”CST” universal parametric geometry representation method”. In: *Collection of Technical Papers - 7th AIAA Aviation Technology, Integration, and Operations Conference* 1.August (2010), pp. 96–127. ISSN: 0001-9240. DOI: 10.1017/s0001924000003614.

[44] Kevin A. Lane and David D. Marshall. “Inverse airfoil design utilizing CST parameterization”. In: *48th AIAA Aerospace Sciences Meeting Including the New Horizons Forum and Aerospace Exposition* January (2010). DOI: 10.2514/6.2010-1228.

[45] Brian Edward Launder and Dudley Brian Spalding. “The numerical computation of turbulent flows”. In: *Numerical prediction of flow, heat transfer, turbulence and combustion*. Elsevier, 1983, pp. 96–116.

[46] Miles L Loyd. “Crosswind kite power (for large-scale wind power production)”. In: *Journal of energy* 4.3 (1980), pp. 106–111.

[47] Xiaoqiang Lu et al. “An improved geometric parameter airfoil parameterization method”. In: *Aerospace Science and Technology* 78 (2018). ISSN: 12709638. DOI: 10.1016/j.ast.2018.04.025. URL: https://doi.org/10.1016/j.ast.2018.04.025.

[48] Florian R Menter, Martin Kuntz, and Robin Langtry. “Ten years of industrial experience with the SST turbulence model”. In: *Turbulence, heat and mass transfer* 4.1 (2003), pp. 625–632.

[49] FLORIANR Menter. “Zonal two equation kw turbulence models for aerodynamic flows”. In: *23rd fluid dynamics, plasmadynamics, and lasers conference*. 1993, p. 2906.

[50] Bruce Valpy Mike Blanch Alexi Makris. “Getting airborne – the need to realise the benefits of airborne wind energy for net zero”. In: Airborne Wind Europe. 2022.

[51] J Morgado et al. “XFOIL vs CFD performance predictions for high lift low Reynolds number airfoils”. In: *Aerospace Science and Technology* 52 (2016), pp. 207–214.

[52] E Omar et al. *Two-dimensional wind-tunnel tests of a NASA supercritical airfoil with various high-lift systems. Volume 2: Test data*. Tech. rep. NASA, 1977.

[53] B Peerlings. “A review of aerodynamic flow models, solution methods and solvers and their applicability to aircraft conceptual design”. In: *Delft University of Technology* (2018), p. 108.

[54] Adam Ragheb and Michael Selig. “Multi-element airfoil configurations for wind turbines”. In: *29th AIAA Applied aerodynamics conference*. 2011, p. 3971.

[55] Arslan Saleem and Man Hoe Kim. “Aerodynamic performance optimization of an airfoil-based airborne wind turbine using genetic algorithm”. In: *Energy* 203 (2020), p. 117841. ISSN: 03605442. DOI: 10.1016/j.energy.2020.117841. URL: https://doi.org/10.1016/j.energy.2020.117841.

[56] Hermann Schlichting and Joseph Kestin. *Boundary layer theory*. Vol. 121. Springer, 1961.

[57] Michael S Selig and Mark D Maughmer. “Multipoint inverse airfoil design method based on conformal mapping”. In: *AIAA journal* 30.5 (1992), pp. 1162–1170.

[58] Adam Slowik and Halina Kwasnicka. “Evolutionary algorithms and their applications to engineering problems”. In: *Neural Computing and Applications* 32.16 (2020), pp. 12363–12379.

[59] A. M. O. Smith. “High-lift aerodynamics”. In: *Journal of Aircraft* 12.6 (1975), pp. 501–530.

[60] Philippe Spalart and Steven Allmaras. “A one-equation turbulence model for aerodynamic flows”. In: *30th aerospace sciences meeting and exhibit*. 1992, p. 439.

[61] GF Syms. “Analysis of general-aviation aircraft wing sections with drooped leading edges”. In: *Journal of aircraft* 43.4 (2006), pp. 1029–1035.

[62] *T-rex hybrid meshing in pointwise*. URL: https://www.pointwise.com/articles/t-rex-hybrid-meshing-in-pointwise.

[63] Paul Thedens, Gael de Oliveira, and Roland Schmehl. “Ram-air kite airfoil and reinforcements optimization for airborne wind energy applications”. In: *Wind Energy* 22.5 (2019). ISSN: 10991824. DOI: 10.1002/we.2313.

[64] Alessandro Vicini and Domenico Quagliarella. “Inverse and direct airfoil design using a multiobjective genetic algorithm”. In: *AIAA Journal* 35.9 (1997), pp. 1499–1505. ISSN: 00011452. DOI: 10.2514/2.274.

[65] K Vimalakanthan et al. “Aerodynamic analysis of Ampyx’s airborne wind energy system”. In: *Journal of Physics: Conference Series*. Vol. 1037. 6. IOP Publishing. 2018, p. 062008.

[66] K. Vimalakanthan et al. “Aerodynamic analysis of Ampyx’s airborne wind energy system”. In: *Journal of Physics: Conference Series* 1037 (June 2018), p. 062008. DOI: 10.1088/1742-6596/1037/6/062008. URL: https://doi.org/10.1088/1742-6596/1037/6/062008.

[67] *Wall function: Boundary layer modelling approach - all about CFD...* June 2022. URL: https://cfdisrael.blog/2021/09/20/wall-function-boundary-layer-modelling-approach/.

[68] *Wall functions*. URL: https://cfd.blogs.upv.es/turbulence/wall-functions/.

[69] *What Is the Genetic Algorithm?* URL: https://es.mathworks.com/help/gads/what-is-the-genetic-algorithm.html.

[70] David C Wilcox. “Reassessment of the scale-determining equation for advanced turbulence models”. In: *AIAA journal* 26.11 (1988), pp. 1299–1310.

[71] Jochen Wild et al. “Advanced high-lift design by numerical methods and wind tunnel verification within the European project EUROLIFT II”. In: *Collection of Technical Papers - AIAA Applied Aerodynamics Conference* 2.June (2007), pp. 1575–1592. ISSN: 10485953. DOI: 10.2514/6.2007-4300.

[72] Xinjie Yu and Mitsuo Gen. *Introduction to evolutionary algorithms*. Springer Science & Business Media, 2010.

[73] Udo Zillmann and Philip Bechtle. “Emergence and economic dimension of airborne wind energy”. In: *Airborne Wind Energy*. Springer, 2018, pp. 1–25.

A

Work plan

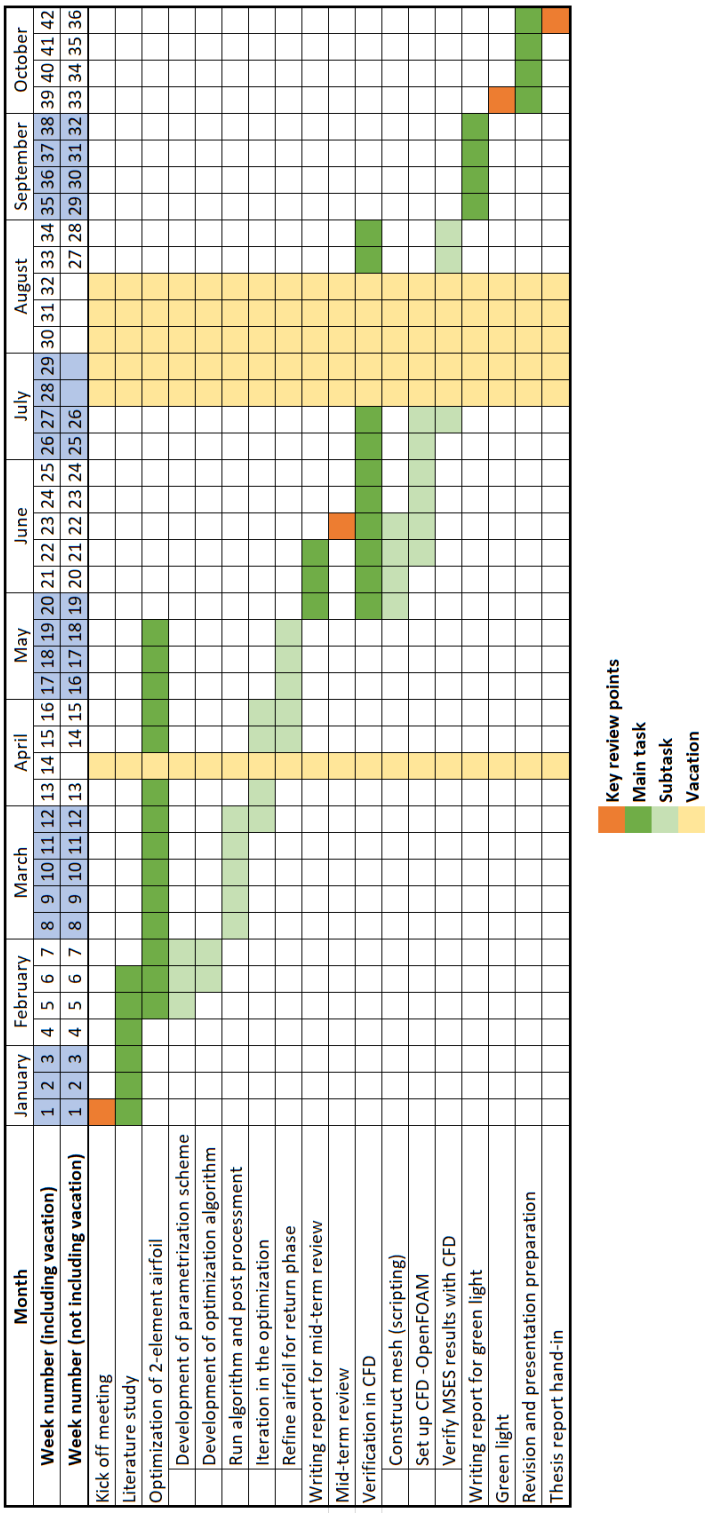

Figure A.1: Gantt diagram of the initial work plan.

B

Flowfield results

B.1. Airfoil in production configuration

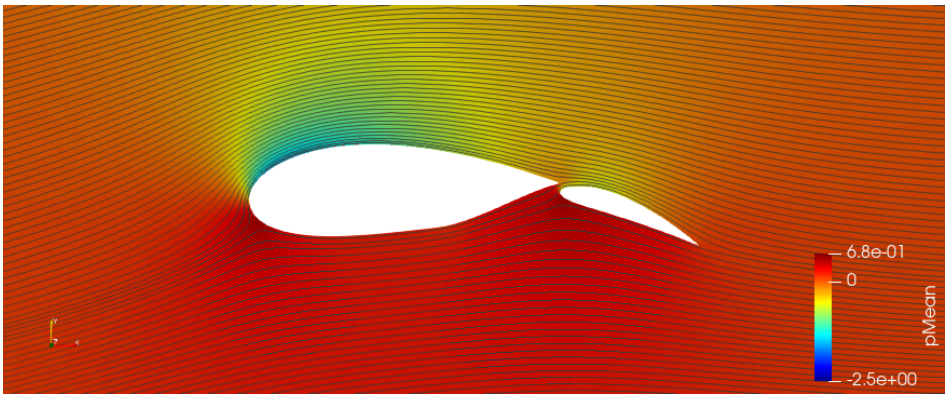

(a) Pressure field with streamlines.

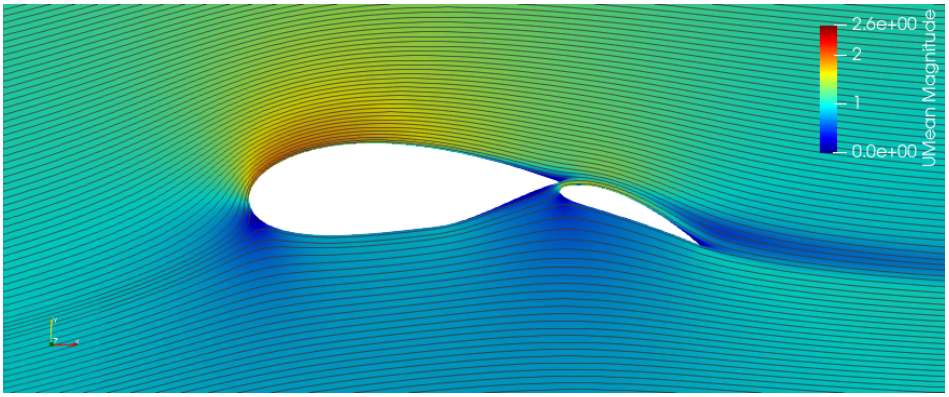

(b) Velocity field with streamlines.

Figure B.1: Flowfield of the optimized multi-element airfoil in production configuration (flap down) at α=5º, i.e. in the linear region, close to the C_{Ldes}.

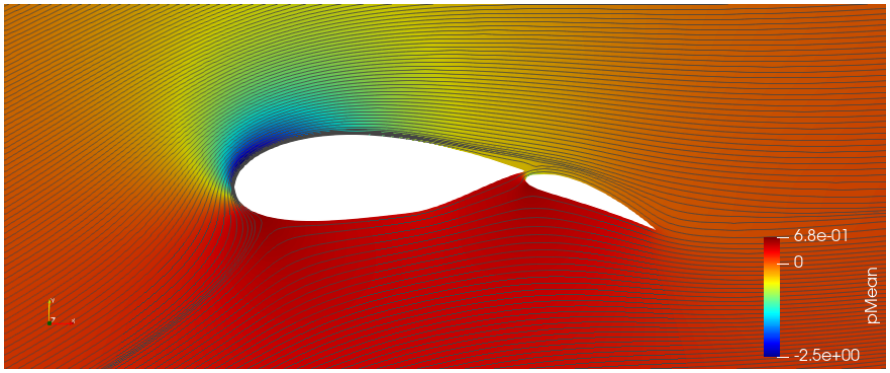

(a) Pressure field with streamlines.

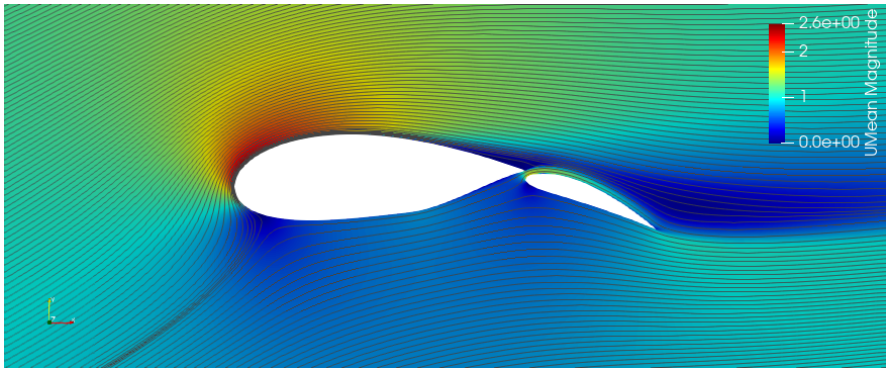

(b) Velocity field with streamlines.

Figure B.2: Flowfield of the optimized multi-element airfoil in production configuration (flap down) at α=15º, i.e. right before stall.

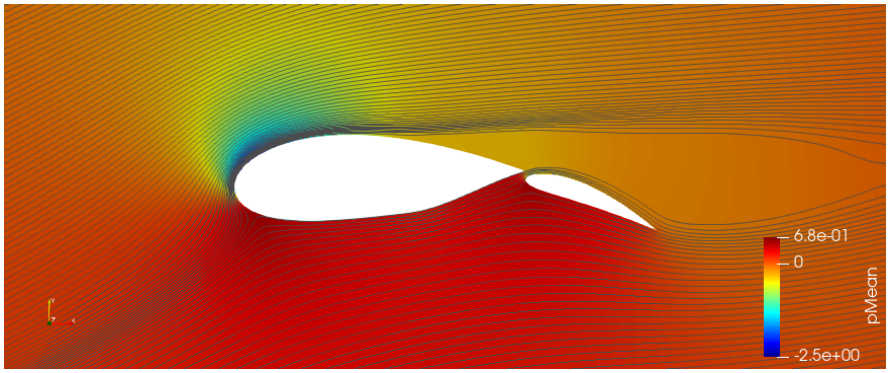

(a) Pressure field with streamlines.

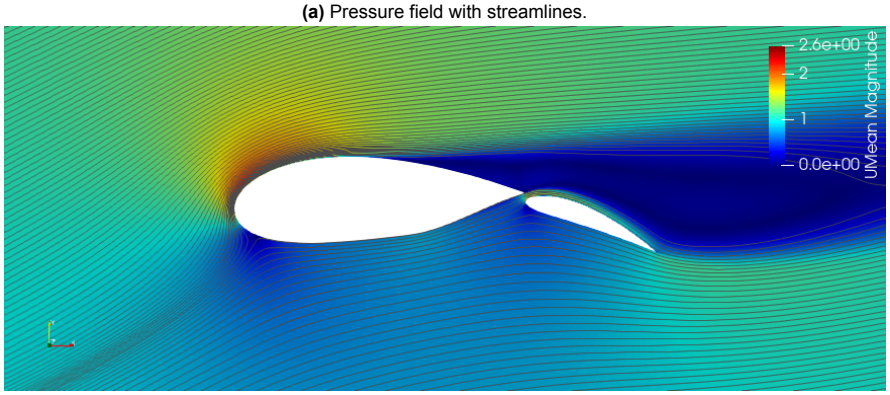

(b) Velocity field with streamlines.

Figure B.3: Flowfield of the optimized multi-element airfoil in production configuration (flap down) at α=16º, i.e. after stalling.

B.2. Airfoil in return configuration

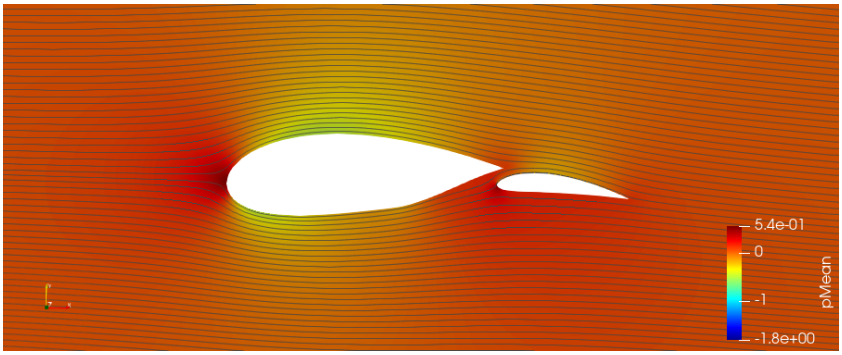

(a) Pressure field with streamlines.

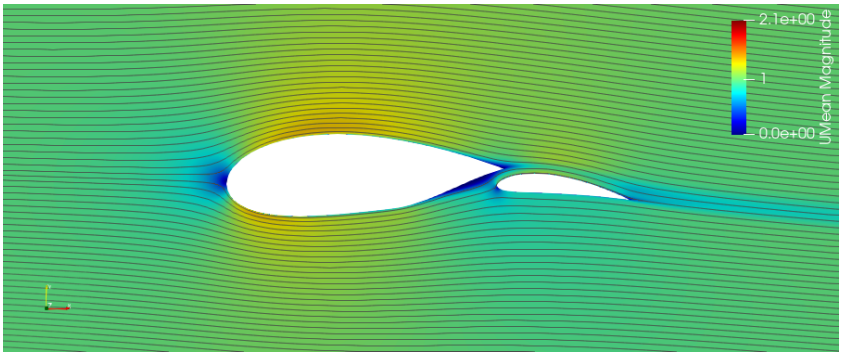

(b) Velocity field with streamlines.

Figure B.4: Flowfield of the optimized multi-element airfoil in return configuration (flap up) at α=-3º, i.e. in the linear region.

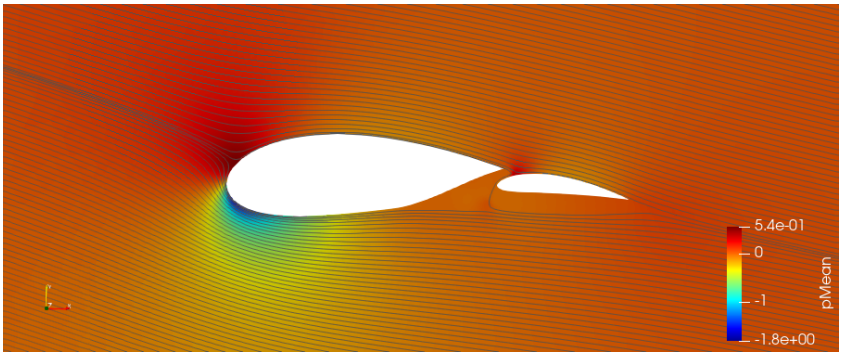

(a) Pressure field with streamlines.

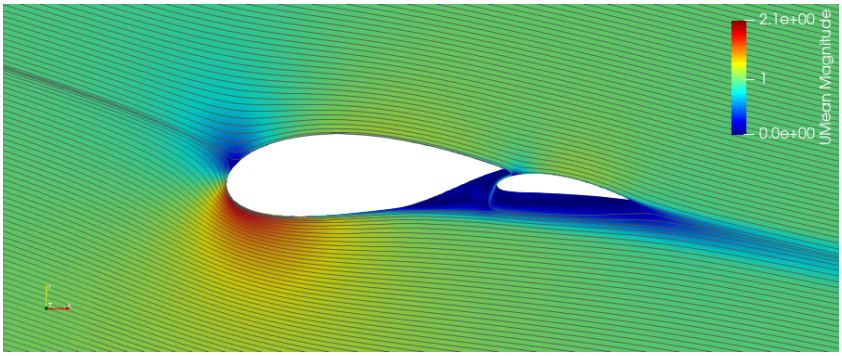

(b) Velocity field with streamlines.

Figure B.5: Flowfield of the optimized multi-element airfoil in return configuration (flap up) at α=-14º, i.e. minimum C_L.